



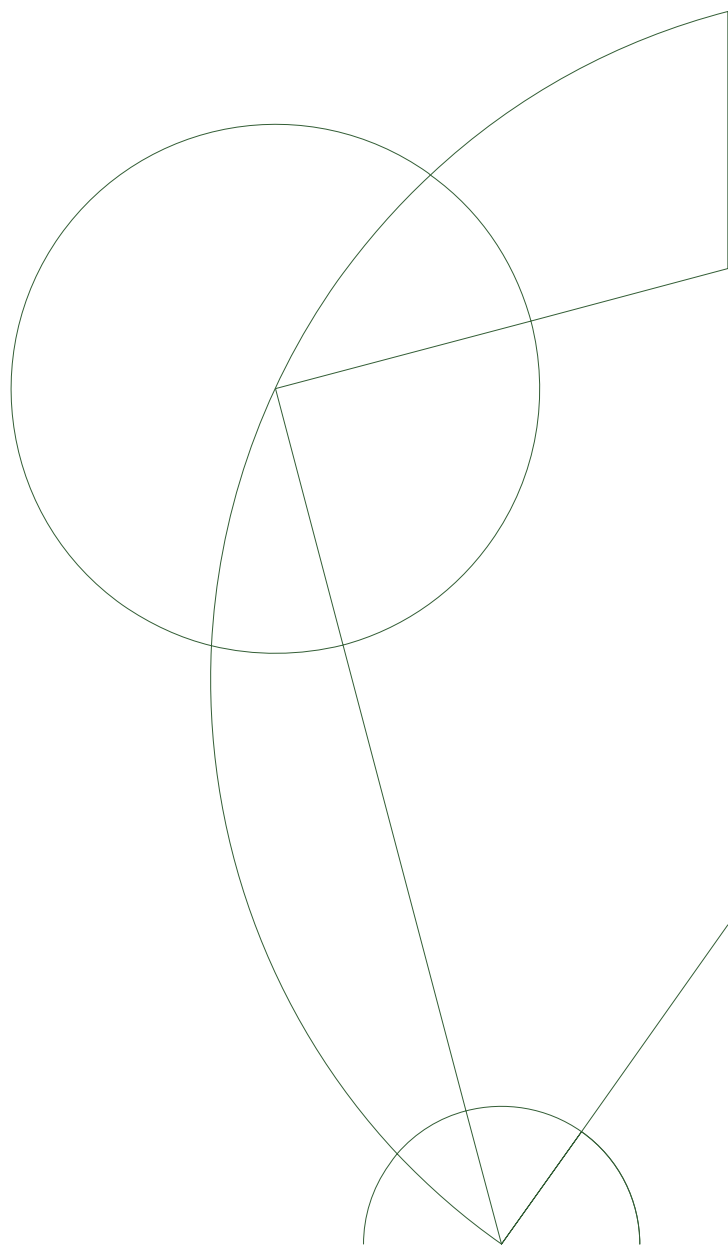
Master's thesis

CMB methods applied to flow data from ALICE

Bastian Poulsen

Supervisor: Jens Jørgen Gaardhøje
Assisting supervisor: Christian Holm Christiansen
University of Copenhagen
Niels Bohr Institute

August 2013



Abstract

This thesis is concerned with the analysis of anisotropic flow. Conventional methods in flow analysis has estimated the flow as an average over many events. In this thesis I will present a method based on the methods used for the study of Cosmic Microwave Background (CMB) which may allow for an event-by-event anisotropic flow determination.

In the thesis the basic theory of heavy ion high energy physics is touched with a special focus on the flow phenomenon and the conventional methods for flow analysis. A brief description of the ALICE detector is given. The theory behind the CMB method is presented as well as the mathematical foundation for this method.

Most of the analysis is performed on simulated event, and in this case the analysis reveals that the method with a high degree of precision is able to recalculate the flow and symmetry plane of up to the eighth order of the flow. The very last part of the thesis is concerned with analysis on real events from the Time Projection Chamber (TPC) in ALICE.

Dansk Resume

Denne afhandling beskæftiger sig med analyse af anisotropisk flow. Konventionelle metoder i *flow* analyse har estimeret *flowet* som et gennemsnit af mange begivenheder. I denne afhandling vil jeg præsentere en metode baseret på de metoder, der anvendes til undersøgelse af kosmisk mikrobølge baggrund (CMB), som kan give mulighed for en begivenhed-til-begivenhed bestemmelse af anisotropisk *flow*

I afhandlingen er den grundlæggende teori for tungions højenergifysik med særligt fokus på flow fænomenet og de konventionelle metoder til flow analyse præsenteret. En kort beskrivelse af ALICE detektoren er givet. Teorien bag CMB metode præsenteres såvel som det matematiske grundlag for denne metode.

Størstedelen af analysen er udført på simulerede begivenheder, og i dette tilfælde viser analysen, at fremgangsmåden med en høj grad af præcision er i stand til at genfinde input *flowet* og symmetriplanen op til den ottende orden. Den allersidste del af afhandlingen beskæftiger sig med en analyse af virkelige begivenhed fra the Time Projection Chamber (TPC) i ALICE.

Acknowledgements

I would like to thank the High Energy Heavy Ion group at the Niels Bohr Institute (NBI), for introducing me to the field of heavy ion physics. In particular I would like to thank my supervisor Professor Jens Jørgen Gaardhøje for giving me the opportunity to do this project for my Master's thesis, and for his kind and patient nature, which has made it a joy working with this project.

A special thanks goes to my assisting supervisor Christian Holm Christiansen for introducing me to the world of computer programming, and his vital and comprehensive help with the rewriting of the GLESP code into ROOT and other programming tasks.

I would also like to thank Ante Bilandzic for providing the data and figures from the TPC events, for very informative and useful comments and correction of the flow chapter and for his intelligible explanations.

A very sincere thanks goes to Hajrah Tabassam, who more than one time took her time to read and correct the entire thesis less than a week before submission. Thanks for a most appreciated very useful and thorough work.

The last thanks goes to my beautiful and lovely wife Elizabeth Morales Poulsen, who at a very difficult period of our life has taken care of my needs, our house and newborn child, and demonstrated compassion and understanding for the importance of the finishing of this thesis.

Contents

1	Relativistic heavy ion collisions	1
1.1	The standard model	1
1.1.1	Quantum Chromodynamics	4
1.1.2	Quark Gluon Plasma	5
1.2	Heavy Ion Collisions	7
1.2.1	Geometry of a collision	7
1.2.2	Physical properties of a collision	9
1.2.3	Evolution of a collision	9
1.2.4	Rapidity	11
1.2.5	Pseudorapidity	11
1.2.6	Transverse energy	11
1.2.7	Multiplicity	12
1.2.8	Impact parameter	12
2	CERN Facility and the ALICE detector	15
2.1	CERN	15
2.1.1	LHC	15
2.1.1.1	The four experiments	17
2.2	The ALICE detector	18
2.2.1	Composition	18
2.2.2	The Time Projection Chamber	20
3	Fourier expansion and Spherical harmonics	23
3.1	The Fourier series	23
3.1.1	Discrete Fourier Transformation	24
3.1.2	Fast Fourier Transform	25
3.2	Spherical harmonics	27
4	Anisotropic Flow	31
4.1	The flow phenomenon	31
4.1.1	Fourier expansion of the collective flow	33
4.1.2	Motivation for studying elliptic and higher order flow	34
4.1.2.1	Importance of the reaction plane	36
4.2	Methods of flow analysis	36
4.2.1	Determination of the event plane	38
4.2.2	The reaction plane method	38
4.2.3	Non-flow	39

4.2.4	The cumulant method	40
4.2.4.1	Reference flow	40
4.2.4.2	Differential flow	42
4.2.4.3	Integrated flow	44
4.2.5	Lee-Yang zeroes method	46
4.2.5.1	Integrated flow	46
4.2.5.2	Differential flow	47
5	Morphology of High multiplicity Events in Heavy Ion Collisions	49
5.1	Motivation	49
5.2	CMB analysis	50
5.2.1	The CMB-method	51
5.2.2	Mollweide projection of heavy ion events	51
5.2.3	Event-by-event Flow analysis	53
5.2.3.1	v_n -modulation with $n = \text{even}$	55
5.2.3.2	v_n -modulation with $n = \text{odd}$	56
5.2.3.3	Analysis on elliptic flow	57
6	Implementation of GLESP into the ROOT framework	59
6.1	From GLESP to ROOT	59
6.1.1	The GLESP package	59
6.1.2	Rewriting of mappat	60
6.1.2.1	Pixelization	61
6.1.3	Evaluation of spherical harmonics coefficients	61
6.1.3.1	The GiRo code	63
6.1.4	End product of GiRo	65
7	The event generator	71
7.1	The JJG-Generator	71
7.1.1	Particle distribution	71
7.1.2	Flow and cuts	72
8	Analysis of simulated events with a single flow harmonic	75
8.1	Settings	75
8.2	Analysis of elliptic flow	75
8.2.1	Determination of the symmetry plane	77
8.3	Higher even order flow estimation	83
8.4	Odd order flow estimation	88
8.4.1	Conlusional remarks	90
9	Analysis of multiflow events	93
9.1	Analysis with equal reaction planes	93
9.2	Analysis with unequal reaction planes	96
9.2.1	Remarks on the flow analysis	98

10 Multiplicity- and mapsize dependence	103
10.1 Analysis with maps narrowing in θ	103
10.2 Multiplicity dependence	106
11 Analysis on real events	111
11.1 TPC analysis	111
11.1.1 Analysis of odd ordered symmetry planes	114
11.2 Accumulated TPC events	115
11.3 Remarks on the TPC analysis	115
12 Conclusion	117
A Cumulants with non-uniform detector acceptance	125
B GiRo coding	127
B.1 Gauss-Legendre quadrature	127
B.2 Drawing of the histogram	128
B.3 Evaluation of $a_{l,m}$ coefficients	128

List of Figures

1.1	Higgs like particle at CMS	3
1.2	Higgs like particle at ATLAS	4
1.3	Color Confinement	5
1.4	The Running coupling constant	6
1.5	QGP phase diagram	6
1.6	Collision coordinate system	8
1.7	Spherical coordinate system	8
1.8	Collision space time diagram	10
1.9	Model of collision and Lorentz contraction	10
1.10	Impact parameter	12
1.11	Multiplicity distribution	13
2.1	CERN Laboratory	16
2.2	Lead injection to LHC	17
2.3	ALICE detector	19
2.4	TPC subdetector	20
2.5	Electron drift	20
3.1	Continuation of a nonperiodic function	25
3.2	Discrete Fourier Transform	26
3.3	Spherical Harmonics for $l = 5$	28
4.1	Elliptic flow	32
4.2	Two particle correlation	32
4.3	$v_2 \cos(2\phi)$	33
4.4	Illustration of how the uneven nucleon distribution inside the nuclei in a collision may be considered as elliptic or triangular flow. The arrow indicate the orientation of the symmetry plane.	34
4.5	Centrality dependence on flow	35
4.6	Higher order flow	36
4.7	Participant plane	37
4.8	Event plane resolution	39
4.9	Differential elliptic flow vs. p_T	45
4.10	Integrated flow v. centrality	45
4.11	Generating function of LYZ	47
5.1	Procedures in CMB-analysis	51

5.2	Map of the CMB fluctuations	52
5.3	Forward backward symmetry of Pb-Pb collision	53
5.4	HIJING event in Mollweide projection	53
5.5	HIJING event in Mollweide projection with $m = 0$ modes removed	54
5.6	Powerspectrum of HIJING event	55
5.7	Results from CMB	57
6.1	Event file	60
6.2	Legendre polynomials	62
6.3	Pixel position in GLESP	62
6.4	Weights	63
6.5	Maps	64
6.6	Fourier coefficients from GiRo	66
6.7	$a_{l,m}$ coefficients from GiRo	67
6.8	Powerspectrum from GiRo	68
6.9	Relative deviations in $\text{Re}[a_{l,m}]$	68
6.10	Relative deviations in $\text{Im}[a_{l,m}]$	69
6.11	Relative deviations in powerspectrum	69
6.12	Relative deviations in powerspectrum	70
7.1	Particle distribution from JJG-Gen	72
7.2	Particle distribution from JJG-Gen	72
7.3	ϕ -distribution with flow from JJG-Gen	74
8.1	Elliptic flow estimation	76
8.2	Maps with different binning	78
8.3	Low Resolution flow estimation	79
8.4	Statistic on binning	80
8.5	Elliptic flow estimation with increasing v_2	80
8.6	Symmetry plane determination of v_2	81
8.7	Statistics on symmetry plane	81
8.8	Symmetry plane determination of $v_2 = 0.1$	82
8.9	Statistic on v_4 flow	83
8.10	v_4 vs. Estimated v_4	84
8.11	v_6 estimation and statistic	85
8.12	v_8 estimation and statistic	86
8.13	Symmetry plane dertermination of ψ_4 and ψ_6	86
8.14	Symmetry plane dertermination of ψ_8	87
8.15	v_3 estimation	88
8.16	$\text{Re}[Y_4^3(\theta, \phi)]$	89
8.17	v_3 estimation by average over northern and southern hemisphere	89
8.18	Statistic on v_3	90
8.19	Statistic on v_7	91
8.20	Statistic on v_5	91
9.1	Statistics on v_n in multiflow events	94
9.2	Statistics on ψ_n in multiflow events	95

LIST OF FIGURES

9.3	Statistics on v_n in multiframe events	96
9.4	v_2 in events with all flow harmonics present	97
9.5	v_7 in events with all flow harmonics present	98
9.6	Symmetry plane lying at the border of the definition range	99
9.7	Symmetry plane determination of ψ_5	99
9.8	Flow estimation for $n = 1, \dots, 6$ with background	100
9.9	Flow estimation for $n = 1, \dots, 6$ with background	101
10.1	Varying mapsize	104
10.2	v_3 and v_4 : Reduced mapsize	105
10.3	Statistics on multiplicity: Flow estimation	107
10.4	Statistics on multiplicity: Symmetry plane determination	108
10.5	Statistics on multiplicity: Flow estimation	109
10.6	Statistics on multiplicity: Symmetry plane determination	110
11.1	TPC event: v_2 distribution	112
11.2	TPC events: ψ_2 distribution	113
11.3	TPC event: v_3 distribution	113
11.4	TPC events: v_1 and v_4	114
11.5	TPC events: Odd ordered symmetry planes	115
11.6	TPC events: Accumulated map	116

List of Tables

1.1	The quark group	2
1.2	The leptonic group	2
1.3	The bosonic group	2
10.1	Table of the slopes for various θ ranges	105

Chapter 1

Relativistic heavy ion collisions

1.1 The standard model

The Standard Model is the key product from the studies of particle physics. It gives an explanation of which particles today are believed to be fundamental, and how their interactions. The idea of fundamental particles dates back as early as the 6th century BC, where the ancient Greeks speculated in the composition of our universe. However it was first in the 19th century that the idea picked up speed when Dalton concluded that all known matter is built from atoms. Rutherford discovered in 1909 with his famous experiment that the atom is not fundamental and in 1919 he found evidence for the proton. Since then a continuous development of the field made it clear that not even the protons (and neutrons) were fundamental, and eventually a formulation of the Standard Model was made.

The Standard Model in its present form, consists of a surprisingly few number of particles, which are divided into groups and subgroups. There are two main groups: the fermions and the bosons. The fermions are all matter particles and can be divided into two groups: the quarks and the leptons. The quarks are represented in table (1.1). Spin is an intrinsic form of angular momentum. All fermions are spin- $\frac{1}{2}$ particles whereas all bosons possess an integer spin number. In fact a boson is defined as a class of particles that possess an integer spin, whereas the fermion is defined as being any class of particles with a half integer spin.

Quarks are combined to make hadrons. A baryon is a combination of three quarks, and a meson is combination of two quarks. The mesons have integer spin, and hence they are bosons, whereas the baryons have half-integer spin and hence they are fermions.

The other group of fundamental fermions are the leptons represented in table (1.2)

The bosons are represented in table (1.3). The bosons are the mediators or force carriers, making it possible for the fermions to interact with each other. The photon is the mediator of the electromagnetic interaction, and couples to any particle with an electric charge. Photons couple to any of the fermions, except the neutrinos, it is massless and travels at the speed of light.

The Z and W^\pm bosons are mediators of the weak interaction. The weak interaction leads to radioactive decay of the fundamental particles and couple to any of the fermions including the neutrinos.

The gluon is the mediator of the strong interaction. It carries a color charge, and

Name	Symbol	Charge	Spin	Mass
Up	u	$+\frac{2}{3}$	$\frac{1}{2}$	$2.4 \text{ MeV}/c^2$
Down	d	$-\frac{1}{3}$	$\frac{1}{2}$	$4.8 \text{ MeV}/c^2$
Charm	c	$+\frac{2}{3}$	$\frac{1}{2}$	$1.27 \text{ GeV}/c^2$
Strange	s	$-\frac{1}{3}$	$\frac{1}{2}$	$104 \text{ MeV}/c^2$
Top	t	$+\frac{2}{3}$	$\frac{1}{2}$	$171.2 \text{ GeV}/c^2$
Bottom	b	$-\frac{1}{3}$	$\frac{1}{2}$	$4.2 \text{ GeV}/c^2$

Table 1.1: The six quarks of the Standard Model

Name	Symbol	Charge	Spin	Mass
Electron	e^-	-1	$\frac{1}{2}$	$0.511 \text{ MeV}/c^2$
Electron neutrino	ν_e	0	$\frac{1}{2}$	$< 2.2 \text{ eV}/c^2$
Muon	μ	-1	$\frac{1}{2}$	$106 \text{ MeV}/c^2$
Muon neutrino	ν_μ	0	$\frac{1}{2}$	$< 0.17 \text{ MeV}/c^2$
Tau	τ	-1	0	$1.78 \text{ GeV}/c^2$
Tau neutrino	ν_τ	0	$\frac{1}{2}$	$< 15.5 \text{ MeV}/c^2$

Table 1.2: The six leptons of the Standard Model

Name	Symbol	Charge	Spin	Mass
Photon	γ	0	1	0
Gluon	g	0	1	0
Z Boson	Z^0	0	1	$91.2 \text{ GeV}/c^2$
W Boson	W^\pm	± 1	1	$80.4 \text{ eV}/c^2$
Higgs Boson	H	0	1	Unknown

Table 1.3: The bosons, also known as the mediators of the standard model. The Standard Model Higgs Boson has not been proven yet to exist, but is a prediction of the Standard Model in order for the other particles to acquire mass. However recent results has found a Higgs like particle with spin 0, and a mass of $126.0 \text{ GeV}/c^2$. Further analysis is needed in order to determine whether this is the Standard Model Higgs Boson.

couples to the quarks. Although it does not appear from the table, all quarks carries a color charge, and the particles couple together into a color neutral state, so that all hadrons are color neutral. This report is especially concerned with the strong interaction, and a more thorough description will be given in the following section.

One of the weaknesses of the Standard Model, has for a long time that if only the experimentally observed and confirmed particles exists, they will all be massless¹. It is a well known fact that our universe is not massless. Several solutions have been proposed

¹Actually it is not a weakness of the standard model, since the standard model also includes the Higgs Boson, furthermore at the moment of writing the Higgs boson has been found and confirmed as a Higgs boson.

to get around this issue. In 1964 six scientists in three different articles [1]-[3], proposed the existence of a boson, that possessed such properties that the time-like particles would acquire mass. One of the writers was Peter Higgs [1] who gave name to the particle. The particle has, at the moment of writing, not been proven to exist, and one of the main goals for the Large Hadron Collider is to prove its existence. However recent discoveries from both the ATLAS and CMS [4] detectors at CERN have shown the existence of an unknown particle. CMS has observed an excess of events at $126\text{GeV}/c^2$, with a statistical significance at 5.0 standard deviations. The chance that this is random background is about less than one to three millions. The results from ATLAS are even better, where a Higgs like particle with a mass at $126.5\text{ GeV}/c^2$ was found. The local statistical significance was at 5.9 standard deviations as shown in figure fig. (1.2). The probability that this is just random background fluctuations, is one to 588 millions. However the global significance is only 5.1 standard deviations. At the time of writing the particle has been confirmed as the long searched for Higgs boson [51] further data is needed to investigate whether this is the Standard Model Higgs Boson.

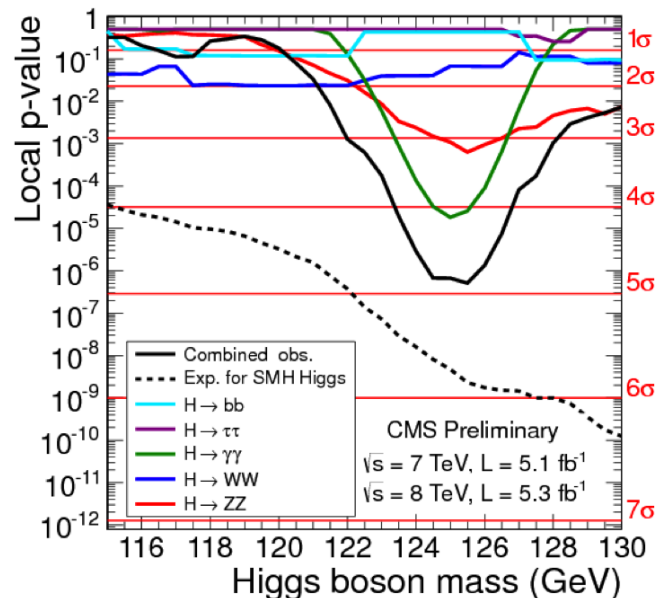


Figure 1.1: Results from the CMS detector, different channels stemming from a Higgs particle. The combination of these channels yields a statistical significance of 5.0 standard deviations

The particles listed in table (1.1)-(1.3) have antiparticles. The properties of an antiparticle are generally the same as for the ordinary particle except that charges is of opposite sign. This is however only in general. As shown in table (1.1)-(1.3), not all of the particles carry charges. Consequently the photon as well as the Z boson and Higgs, are their own antiparticles. The gluon carry color charge, however there are eight types of gluons. These are referred to as a gluon octet. The antiparticle of any of the gluons is contained in this octet, and therefore the gluon octet is its own antiparticle. The neutrinos do not carry any charge. It is not certain whether the neutrino is its own antiparticle. Experimental differences in spin has been found between the neutrino and the supposed antineutrino, but it is not certain that this difference can be ascribed to the fact that they

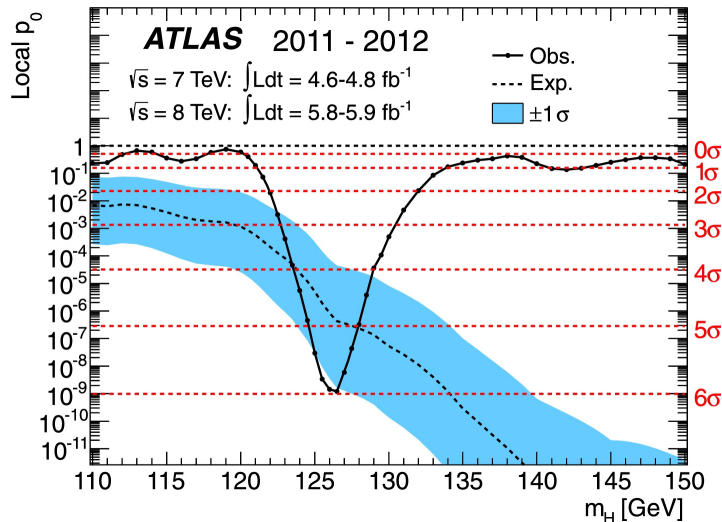


Figure 1.2: Results from the ATLAS detector. The combination of three channels that originates from a Higgs particle yields a local statistical significance at 5.9 standard deviations. However the global significance would only be 5.1.

are each others antiparticle [5].

1.1.1 Quantum Chromodynamics

Quantum Chromodynamics (QCD) is the theory of the strong interaction. As mentioned above this interaction is mediated by gluons. The name comes from the fact that it is the strongest of the four fundamental interactions. It is 100 times stronger than the electromagnetic interaction and 10^{14} times stronger than the weak interaction [8]. In the standard model the quarks are the only fundamental particles which are affected by the strong interaction. Just like in the electromagnetic case the quarks carry charges of the strong interaction. But where in the electromagnetic case there is only one positive and one negative charge, in QCD there are three different “positive” charges and three “negative” charges. The charges are labelled with the names of colors (this has nothing to do with physical colors), red (r), green (g) and blue (b) for the “positive” charges, where the “negative” charges are labelled as anticolors of the “positive”. They are called antired (\bar{r}), antigreen (\bar{g}) and antiblue (\bar{b}). In QCD the mediators the gluons do them self carry charges with important consequences: The first is that the gluons can couple to each other, and the second is that the gluons are able to change the charge of the particle it interacts with. However charge will always be conserved. This means that if a particle carries red charge and changes its color to blue in the interaction with a gluon, then the gluon must have carried an antired and a blue charge.

Although quarks and gluons fit perfectly into the Standard Model they have actually never been observed. So QCD will have to answer for this difference between theory and phenomenology. The answer lies in the color confinement.

The way quarks behave when they are coupled with the strong interaction, can be compared to the behaviour of a rubber band. When quarks are separated the tension increases with distance. In other words the greater the distance is between two particles,

the more energy is required to separate them even further. At some point in the process of separating the particles, enough potential energy has been built up for a new pair of quarks to be created to which the original pair of quarks will couple, and hence it is not possible to observe free quarks. This is illustrated in figure (1.3). The separation of quarks at high energies leads to a narrow banded spray of hadrons which is known as jets.

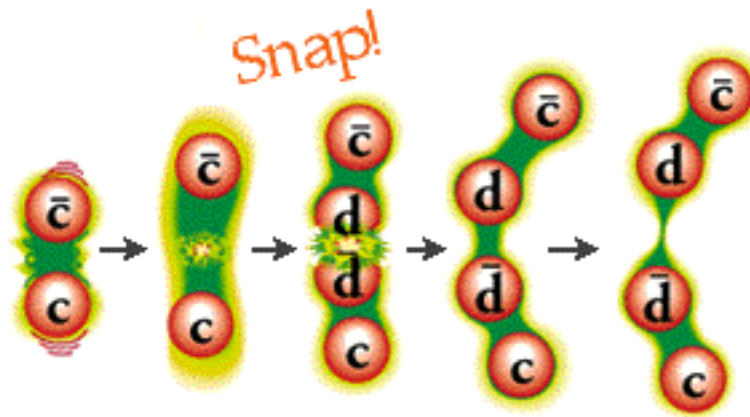


Figure 1.3: The figure displays how a charm and anticharm quark are separated. When the distance between the quarks increases energy and tension builds up. The bond between the original quark pair breaks when the potential energy reaches a level where a new pair of quarks can be created.

The property that the coupling constant decreases with distance is known as asymptotic freedom and was proven in 1973 [7]. Figure (1.4) is a summary of measurements of the strong coupling constant α_s (which is not a constant). It shows how α_s decreases with increasing energy, and hence increases with distance.

This makes it interesting to go to the other limit the limit with very short distances between the quarks. In this case the coupling between the quarks will basically not exist and it is possible to consider the quarks as freely moving particles. The very same thing would happen if the temperature is increased sufficiently. So the goal is to create a very dense and/or hot matter and then study the behaviour of the particles. This matter is called the quark gluon plasma (QGP) figure (1.5) shows the regime of the QGP.

1.1.2 Quark Gluon Plasma

QGP is expected to exist in two places in the universe, one is inside the neutron stars (or even denser cosmic objects like black holes) where densities are very high. And the other is in the laboratory where it is possible to create high energy densities by smashing two high energetic nuclei into each other. In the simplest case the transition from ordinary nuclear matter to QGP can be compared to a thermodynamical phase transition. Particles will go from a bounded state to a state where they can interact more freely. Just like water which changes from liquid to gas at a specific temperature. The requirement that the phase transition happens at a specific temperature is that the matter is in thermodynamical equilibrium. In the same way if the nuclear matter is in thermodynamical equilibrium the phase transition will happen at a specific temperature, the critical temperature. Calculations indicate that the critical temperature is $T_c \approx$

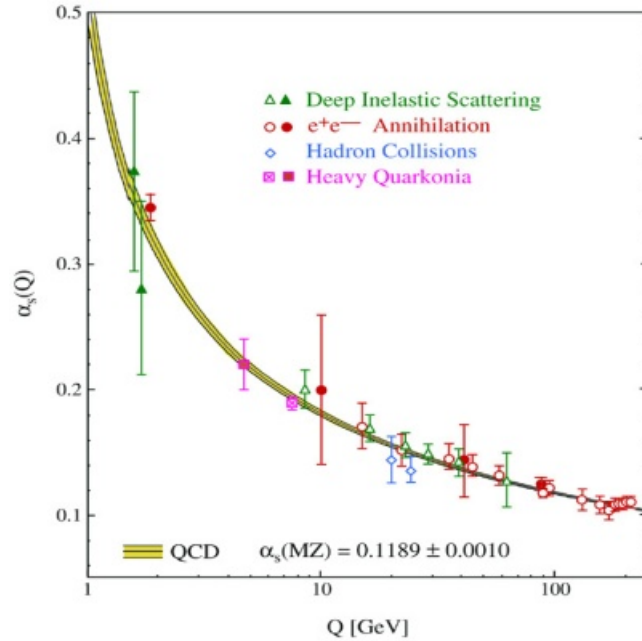


Figure 1.4: The coupling constant of the strong interaction. This is a summary of data from several measurements. It is clear from the figure that the coupling constant is not at all a constant, and that it decreases with increasing energy [8].

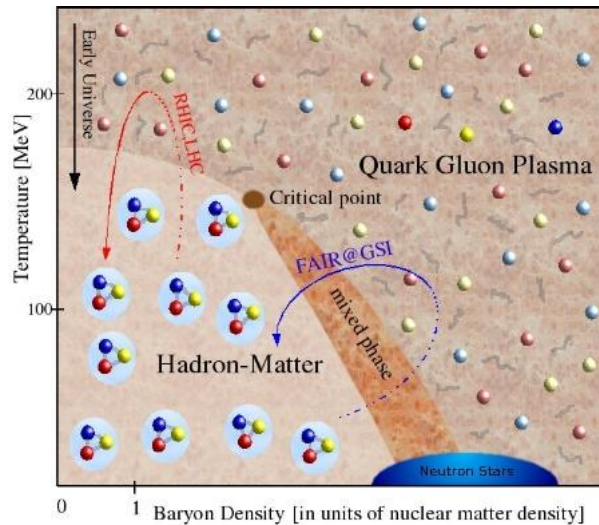


Figure 1.5: The diagram shows the regime where QGP is possible. The red curved arrow indicates where in the diagram to place the relativistic heavy ion experiments from RHIC and LHC

175MeV [10]. However it is uncertain whether and when thermodynamical equilibrium is to be expected and hence the temperature can vary. In a certain temperature interval near the critical temperature hadron gas is expected to be found inside the QGP. This effect is known as bubbles.

There is another effect, that is the flow. When nuclei are smashed into each other,

a rapidly expanding fireball is created. This expansion will follow a certain pattern depending on whether the particles can be regarded as unbounded. This will be elaborated much further in chapter 4, for now it suffice to say that evidence of flow was first detected in the Relativistic Heavy Ion Collider (RHIC) at Brookhaven university, in 2001 with an energy at $\sqrt{s_{NN}} = 130$ MeV [11].

1.2 Heavy Ion Collisions

It turns out that one of the best ways to study QGP is by colliding heavy ions into each other at relativistic speeds. The heavy ion physics can be divided into three regions of energy.

- i The intermediate energy region
- ii The relativistic energy region
- iii The ultra-relativistic energy region

Where the first two regions covers the energy upto 10GeV [9]. Experiments in this region have basicly been used for extracting information about the Equation Of State (EOS) of the heavy ion reaction. A lot of theoretical work about the QGP which is now possible to be tested has been done based on collisions in these regions.

The Ultra-relativistic region covering physics with energies above 10GeV, is the one that concerns this report. In this region it is possible to examine properties of the QGP. The QGP is being examined at the Relativistic Heavy Ion Collider (RHIC) at Brookhaven National Laboratory (BNL) with energies up to 250GeV per nucleon, and the Large Hadron Collider (LHC) at CERN with energies up to 7 TeV per nucleon. This report is mainly concerned with projects connected to the ALICE (A Large Ion Collider Experiment) collision detector at LHC and a further description of this detector will be given in chapter (2). The current section will cover some of the basic properties and standard expressions of a collision.

1.2.1 Geometry of a collision

There are several ways of defining a coordinate system for a collision. The coordinate system can be defined with respect to a fixed laboratory frame or by certain aspects of the collision which will determine the orientation of the coordinate system. The coordinate systems mentioned below, all have the Center of Mass (CM) as origin in common. In the laboratory frame the coordinate system can be defined by using Cartesian coordinates. The z -axis is parallel to the beam direction. The x and y axes spans the plane orthogonal to the beam direction, and is designated the transverse plane with the x -axis parallel to the local horizontal pointing towards the center of the accelerator, and the y -axis is perpendicular both to the x - and the z -axis [27].

If the nuclei do not collide head on, such that there individual center of masses are displaced by on amount b with respect to each other, the x -axis will be placed parallel to the displacement vector \vec{b} , and the plane spanned by the beam axis and the vector \vec{b} is designated as the reaction plane. The coordinate system can be tilted in order to make

the x and y axes span the reaction plane as shown in figure (1.6). In the following a frame which is oriented with respect to the reaction plane, will be referred to as the collision frame.

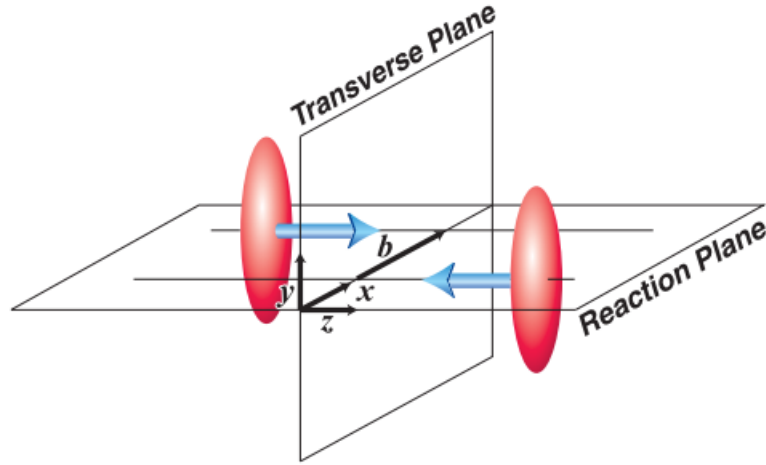


Figure 1.6: The coordinate system of a collision, with the x -axis parallel to the displacement vector \vec{b} , making the x and y axes span the reaction plane.

Spherical coordinates are often used instead of Cartesian coordinates. The variables are the radius r , the polar angle θ and the azimuthal angle ϕ . The azimuthal angle covers the transverse plane, and the polar angle covers the xz -plane [27]. The variable θ which is either in degree or radians is often replaced by the pseudorapidity η given by equation (1.3) in section 1.2.5. In the laboratory frame $\phi = 0$, is placed at the horizontal line pointing towards the center of the accelerator. The spherical coordinates are illustrated in figure (1.7).

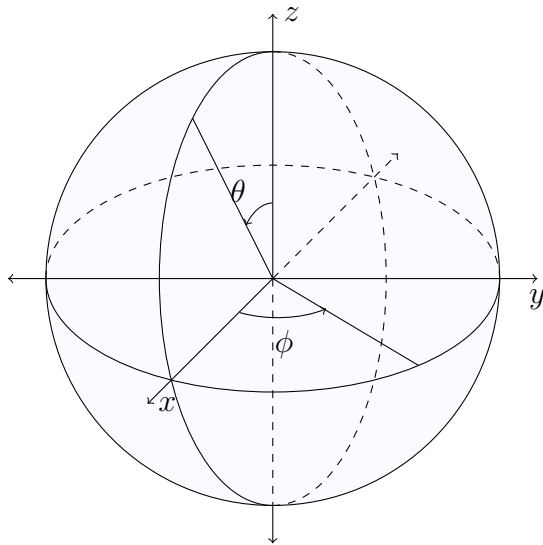


Figure 1.7: The coordinate system of a collision using spherical coordinates. The z -axis is the beam axis.

1.2.2 Physical properties of a collision

In relativistic heavy ion collisions, an atom is stripped off all its electrons to isolate the nucleus. In the RHIC, gold nuclei are preferred whereas in LHC lead are the nuclei most commonly used. The nucleus is not electrically neutral and hence it is possible to accelerate it by creating a magnetic field. The nucleus reaches relativistic velocities, and hence relativistic effects must be taken into consideration.

This means that particles are subjected to Lorentz contraction, for example for a lead nucleus with radius 5.92 fm travelling at speed $0.9999996c$ (7TeV) the radius of the nucleus in the beam direction would only be $5.14 \cdot 10^{-6} \text{ fm}$ or $8.67 \cdot 10^{-5}\%$ of the radius of the nucleus transverse to the beam direction. So in the CM frame the colliding nuclei can be considered as two very flat discs approaching each other. The consequence of the collisions of the nuclei is that a huge amount of energy will be stored in a very small volume.

For a collision that is not head on, parts of the nuclei will continue essentially without being affected by the collision. These are called spectators. The remaining parts which interact, are called the participants.

1.2.3 Evolution of a collision

A hydrodynamical model is used for description of a collision. The model requires a local thermal equilibrium, which means that in a small region it is always possible to define a temperature. A lot of experimental data has successfully been explained by the hydrodynamical model. Although results from LHC and RHIC suggest a local thermal equilibrium [13], it is however still uncertain whether an equilibrium of QGP before phase transition to hadronic gas (HG) is ever reached. The process of reaching equilibrium is called thermalization.

In the initial stage of a collision, participants penetrate into a state, designated “a fireball”, of very high temperature and with partons³ interacting freely. This state is in no sense in equilibrium. Thermalization is reached through collisions of the constituents of the fireball. The fireball is surrounded by vacuum, and it will start expanding itself into the vacuum due to thermal pressure. In a small energy interval around the phase transition from QGP to hadronic gas HG, hadrons will start to form, which means that entropy is decreasing. Since the second law of thermodynamics do not allow for an overall decrease of entropy it means that the system will have to expand very rapidly, but with a constant temperature.

After the phase transition a freeze out stage is reached. This stage is divided into two substages. The chemical freeze out which is reached when the production of hadrons has stagnated because the expansion happens so fast that hadron producing inelastic collisions do no longer contribute to the hadron production. Local thermodynamic equilibrium can be maintained due to elastic collisions. As the system continues to expand and cool down, a stage is reached where the average distances between the hadrons is so large that effects from the strong interaction disappears. Collisions between the hadrons will happen so rarely that local thermodynamic equilibrium can no longer be maintained and the laws

²This value is reached by taking $r = r_0 \sqrt[3]{A}$ where $r_0 \approx 10^{-15} \text{ fm}$ is the radius of a single nucleon, and $A = 207$ is the number of nucleons in lead

³gluons and quarks

of hydrodynamic break down. This is called the kinetic freeze out. A space time diagram of the situation is seen in figure (1.8), and in figure (1.9) a four step model of a collision is shown.

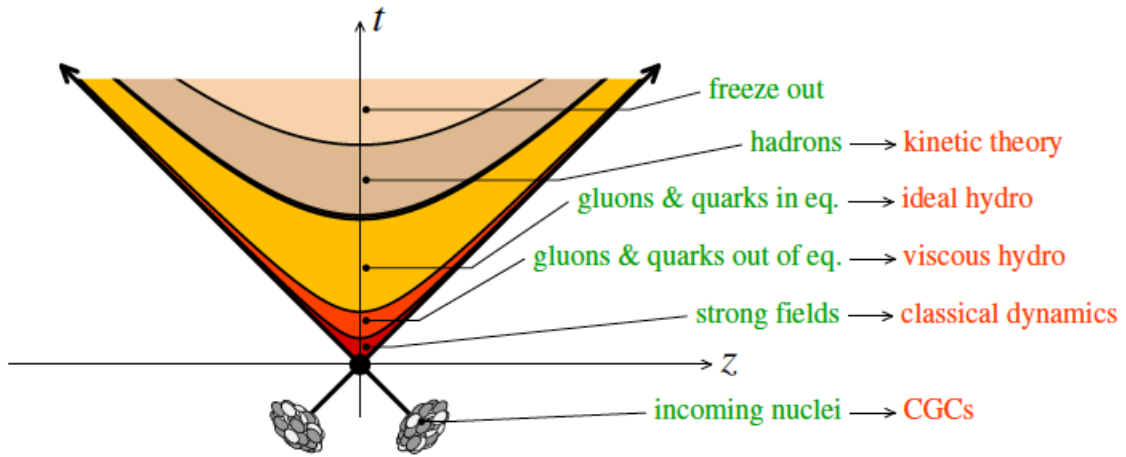


Figure 1.8: The evolution of a fireball from initial collision to kinetic freeze out plotted in a space time diagram. At the bottom of the diagram the two incoming nuclei is drawn along the diagonal and hence indicating the relativistic speed.

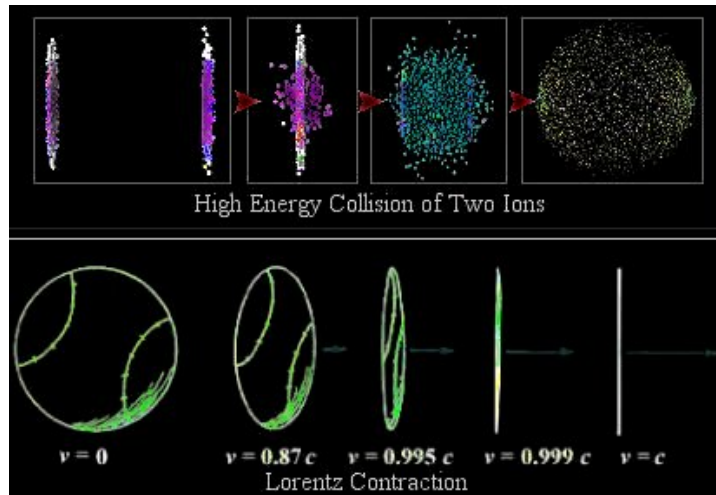


Figure 1.9: A model of a relativistic heavy ion collision. At the top the initial step is the nuclei approaching each other. Second step is right after the collision with formation of QGP and the process of thermalization. Third step is the expansion of the fireball and hadronization. And the fourth step is the kinetic freeze out. In the bottom is shown the Lorentz contraction of a nuclei with increasing speed.

1.2.4 Rapidity

It has proven useful to infer a parameter for velocity. It is defined as

$$y = \frac{1}{2} \ln \frac{E + p_z}{E - p_z} \quad (1.1)$$

Where p_z is the z component of the momentum, and thus the momentum in the beam direction. It can be rewritten in the form

$$\begin{aligned} y &= \frac{1}{2} \ln \frac{1 + \frac{p_z}{E}}{1 - \frac{p_z}{E}} = \tanh^{-1} \frac{p_z}{E} \\ &= \tanh^{-1}(\beta_L) \end{aligned} \quad (1.2)$$

[30] where $\beta_L = \frac{p_z}{E}$ is the longitudinal velocity. The reason for using rapidity instead of velocity is that the rapidity is additive under a longitudinal boost. For example a particle moving with rapidity y in a frame with rapidity dy will have rapidity $y + dy$ to an observer outside the frame.

1.2.5 Pseudorapidity

Another important variable is the pseudorapidity. If the angle θ of an emitted particle with respect to the beam direction is known, one can calculate the pseudorapidity by making the approximation that mass contribution to the energy at high momentum is negligible. Starting from the rapidity

$$\begin{aligned} y &= \frac{1}{2} \ln \frac{E + p_z}{E - p_z} \\ &= \frac{\sqrt{m^2 + \vec{p}^2} + \vec{p} \cos \theta}{\sqrt{m^2 + \vec{p}^2} - \vec{p} \cos \theta} \\ &\approx \frac{\vec{p} + \vec{p} \cos \theta}{\vec{p} - \vec{p} \cos \theta} \\ &= -\ln \tan \frac{\theta}{2} \equiv \eta \end{aligned} \quad (1.3)$$

[30] where η is defined to be the pseudorapidity it is convenient to work with because the only information needed is the angle. Another reason for working with the pseudorapidity is that it has very high resolution around the beam axis whereas it decreases for larger angles of θ . E.g. the angles from $\frac{\pi}{4}$ to $\frac{\pi}{2}$ has pseudorapidity from 0.88 to 0, whereas the angles from 0.0001 to $\frac{\pi}{4}$ has pseudorapidity from 10 to 0.88. In a collision most of the particles produced from the fireball will be detected at small angles and hence it is useful to have a higher resolution at these angles.

1.2.6 Transverse energy

The transverse momentum (\vec{p}_T) is the component of the momentum in the transverse plane. It is an important factor in particle collisions, because a significant and unknown portion of the incoming energy escapes the detector along the beampipe. Consequently

the momentum is not conserved in the beam direction. However it is possible to determine the momentum in the transverse plane. Since momentum conservation is expected the net transverse momentum must equal zero unless some particles have not been detected. The missing transverse momentum is given by

$$\vec{p}_T = - \sum_i \vec{p}_T(i) \quad (1.4)$$

where the sum runs over each final state particle [26]. The missing transverse energy ($/E_T$) can be derived from the magnitude of the missing transverse momentum. It is worth mentioning that the scale in transverse direction is larger than the scale in the beam direction due to the Lorentz contraction of the system [31].

1.2.7 Multiplicity

Another variable is the multiplicity, which is simply the number of produced particles. Most of the times multiplicity refers to the number of produced charged particles. It is convenient to give the multiplicity as a function of the pseudorapidity, and hence the given multiplicity is given for a certain region in η . The multiplicity will be expressed as

$$\frac{dN}{d\eta} \quad \text{or} \quad \frac{dN_{ch}}{d\eta} \quad (1.5)$$

where the first expression is for all produced particles, and the second expression is for the produced charged particles only.

1.2.8 Impact parameter

As previously noted a collision may not always be head on. The center of mass of the individual nuclei may be displaced an amount b as illustrated in figure (1.10). This displacement

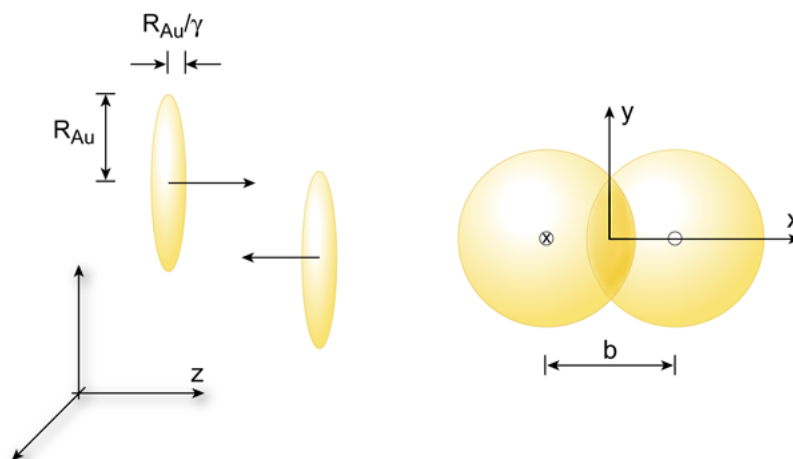


Figure 1.10: The collision geometry, where the impact parameter b is shown.

b is called the impact parameter. The impact parameter can not be detected directly, so in order to determine the impact parameter one will have to determine some aspects

of how the system would be affected by different impact parameters. Collisions with different impact parameter may be qualitatively as well as quantitatively different. One of the obvious differences is the multiplicity and the energy in the transversal direction ($E_T = \sum_i E_i \sin \theta_i$).

Instead of using the impact parameter, centrality can be used instead. The centrality is basically the same as the impact parameter, although centrality is a fractional dimensionless number, where as the impact parameter is a distance. Centrality is a number between 0% and 100%, where 0% is the most central event, and 100% is the most peripheral event. It is possible to relate the collision centrality to the number of observed particles and neutron spectators.

Models are developed to estimate the initial geometric configuration (including the impact parameter and number of spectators and participants) of the collision from the centrality. The models can generally be divided into two classes: The optical Glauber model, and the Monte Carlo Glauber model. The Monte Carlo Glauber model assumes all particles in the nucleus to be fixed at a stochastically determined position inside the nucleus, and then the nuclei are collided assuming that each nucleon follow a straight line along the beam axis. This imply that prior to the collision the number of spectators and participants is known if the impact parameter is known. The position of the nucleons is usually determined by assuming an even distribution in each shell of the nucleus, so that the distribution is only a function of the nucleus radius.

Figure (1.11) shows a distribution of 65000 events, where the centrality is calculated. The vertical lines separate the centrality classes such that the grey area farthest to the right represent the 5% most central events.

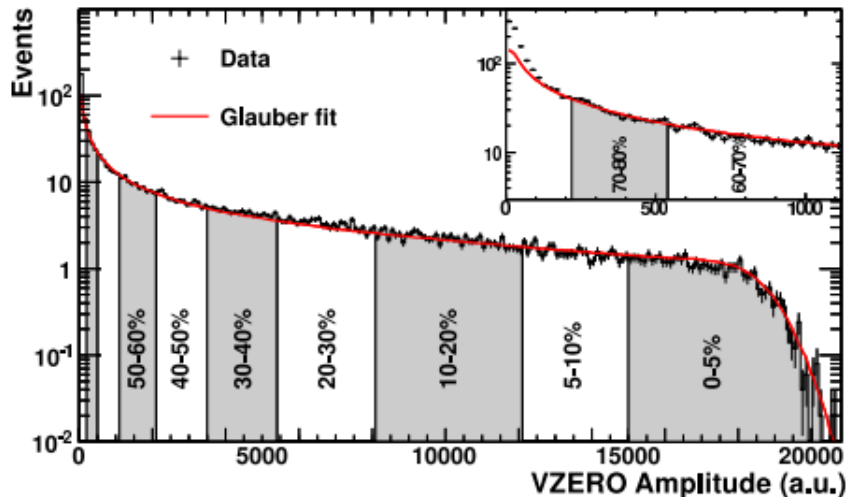


Figure 1.11: Collision centrality based on 65000 events. The 80% most central events are shown. The red line is a Monte Carlo Glauber prediction of the particle production. And the black line is the actual data.

Chapter 2

CERN Facility and the ALICE detector

This chapter is devoted to a description of the LHC particle accelerator at CERN and the ALICE detector. The main data analysis in this thesis is performed on simulated events, however some analysis is also performed on real data extracted from a subdetector system in ALICE labelled as the Time Projection Chamber. Furthermore the analysis currently performed on simulated events, targets a more extensive analysis on real data from ALICE. A brief introduction to the LHC and CERN will be given, followed by a more thorough description of the ALICE experiment. In the last part of the chapter a description of the Time projection Chamber will be given.

2.1 CERN

The CERN (from french: Conseil Européen pour la Recherche Nucléaire, translated as European Council for Nuclear Research) laboratory was founded in 1954 in order to probe the fundamental structures of the universe, as one of Europe's first joint ventures and now has more than 20 member states. It is located at the franco-swiss border and is a complex of accelerators and detectors (see figure (2.1)), where the LHC currently is the accelerator reaching the highest energies.

2.1.1 LHC

Although there are other accelerators at CERN, LHC is the largest and is in fact the largest and most powerful accelerator in the world. It consists of a 27 km. long ring built of superconducting magnets with a number of accelerating structures to boost the energy of the particles along the way. When the detector is fully upgraded it is expected to accelerate protons up to 14 TeV per nucleon pair ($\sqrt{s_{NN}}=8$ TeV is currently the highest CM energy reached [49]) or lead ions up to 5.76 TeV per nucleon pair (The lower energy is due to the uncharged neutronic dead weight). The particles inside the accelerator travels along opposite directions in separate beam-pipes before they are made to collide in the detectors. They are guided along the tunnel with a strong magnetic field supplied by superconducting electromagnets kept at temperature of 1.9K. In order to avoid collisions with gas molecules a vacuum pressure at 10^{-13} atm. is kept in the beam-pipes.

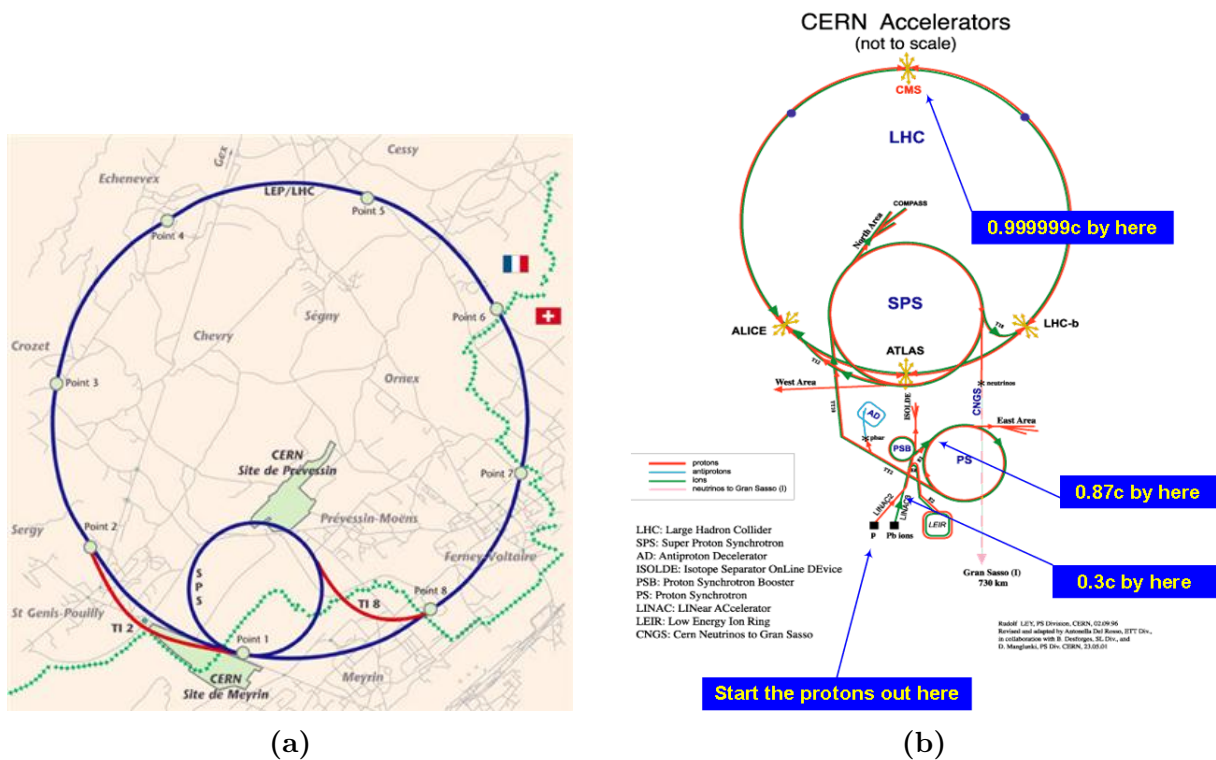


Figure 2.1: The CERN Laboratory: Panel 2.1a represents a scaled map of the CERN facility at the franco-swiss border. Panel 2.1b represents a schematic overview of the CERN facility, where the red and green lines indicate the travel paths of the proton and ion beams respectively, before injected into the LHC.

LHC is mainly focused on proton-proton collisions, however shorter periods (typically one month a year) are devoted to heavy ion collisions. The ions used for the collisions are Pb-ions. The initial injected particles are Pb-Atoms, which will have to be stripped off all its electrons in order to get the Pb^{82+} ion used in the collisions. This is a four step procedure, where the first step is to strip the Pb-Atoms of 27 electrons to get Pb^{27+} by use of an Electron Cyclotron Resonance source. A current of the Pb^{27+} ions are injected to the linear accelerator LINAC 3, where the energy is boosted to 4.2 MeV per nucleon. Before injected to the Low Energy Ion Ring (LEIR) the ions are stripped off an additional 27 electrons. In LEIR the energy is further boosted to 72.2 MeV per nucleon. From LEIR the ions are injected to the Proton Synchrotron (PS) where the energy is further boosted to 5.9 GeV per nucleon. Before entering the Super Proton Synchrotron the Pb^{54+} ions are stripped off their last 28 electrons. In the SPS the lead ions are accelerated to 177 GeV per nucleon. Eventually each LHC ring will be injected with 592 bunches each containing 7×10^7 lead ions. The filling takes approximately 10 minutes. The whole process is schematized in figure (2.2) and in figure (2.1b) where the path is represented by the green line. Protons take a slightly different path as they are first injected through the linear accelerator LINAC 2 instead of LINAC 3. After LINAC 2 they are boosted in the Proton Synchrotron Booster (PSB). The rest of the path is the same as for ions, although protons are boosted to a higher energies and obviously protons do not have to be stripped off the electrons.

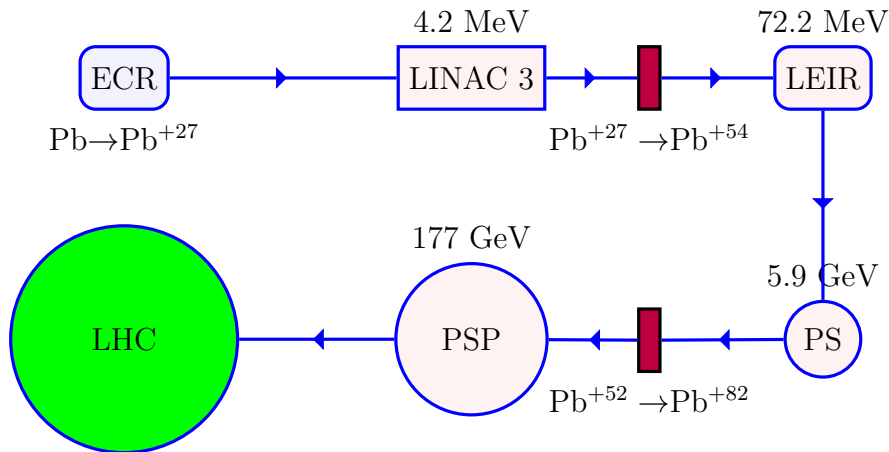


Figure 2.2: The path of lead atoms before injected to the LHC accelerator.

2.1.1.1 The four experiments

10 experiments are associated with the LHC, whereof seven of these use detectors. The four major experiments are the ALICE, ATLAS, CMS and LHCb where ATLAS (A Toroidal LHC ApparatuS) and CMS (Compact Muon Solenoid) are general purpose detectors (where the general purpose is to shed light on inconsistencies in the standard model) designed to cover the largest range of physics possible. ATLAS and CMS are designed independently of each with advantages and disadvantages. This is of vital importance since this allows for cross-confirmation of any new discovery between the two experiments. The research areas of ATLAS and CMS ranges between the search for the

now discovered Higgs boson, the breaking of supersymmetry, dark matter and a more precise determination of the mass of the top quark among others.

The ALICE (A Large Ion Collider Experiment) experiment has a more specific purpose namely to create and investigate the QGP.

The LHCb (Large Hadron Collider beauty) experiment is designed to study interactions between b-hadrons, where b-hadrons are hadrons containing a bottom quark. The purpose of b-physics is to explain the asymmetry between matter and antimatter by measuring the charge-parity (CP) violation of b-hadrons.

2.2 The ALICE detector

Although both ATLAS and CMS also analyse the phenomena, ALICE is the detector specifically designed for the study of QCD and in particular the behaviour of QGP. The physics programme of ALICE includes lighter ion collisions and at lower energies in order to vary energy density and interaction volume, as well as the high energy Pb-Pb collisions with the highest multiplicities anticipated at LHC for which it is designed. ALICE is located at point 2 (see figure (2.1a)) on the french site of the border. The beam line running through ALICE is 44 m. underground. The detector is built by a collaboration including more than 1000 physicists and engineers from 105 institutes and 30 countries. The overall dimensions of ALICE is $16 \times 16 \times 26$ m. and a total weight of 10000 t. The major task in the design of the ALICE detector, is to deal with the high particle multiplicity which were predicted to be in the range of two to five times larger than the highest multiplicities measured at RHIC. In order to measure the higher rate of particles per event, the beam interaction rate is significantly reduced as compared to proton collisions, this allows for slower detectors with higher precision.

2.2.1 Composition

A particle detector generally consist of several layers of subdetector system which can be divided into three groups.

Tracking detectors: Reveal the path of a particle by letting the particles pass through and interact with a suitable substance

Calorimeters: Stop, absorb and measure a particle's energy

Particle-identification detectors: Pin down a particle's identity

The subdetector systems in ALICE can be divided into a central barrel part and a forward muon spectrometer. The central part covers angles between $\cos \theta = (\pm \frac{\sqrt{2}}{2})$ or in terms of pseudorapidity $|\eta| = 0.9$ and is embedded in a large solenoid which is visualized in figure (2.3) as the red part surrounding the central detector. Unless otherwise noted all subdetector systems cover the full azimuthal range between 0 and 2π .

The three innermost detectors are tracking detectors. From the inside out these are the Inner Tracking System (ITS) surrounding the beam pipe. The ITS consists of six cylindrical layers of high resolution silicon detectors: Two Silicon Pixel Detectors (SPD) for the innermost layers, two Silicon Drift Detectors (SDD) for the following two layers

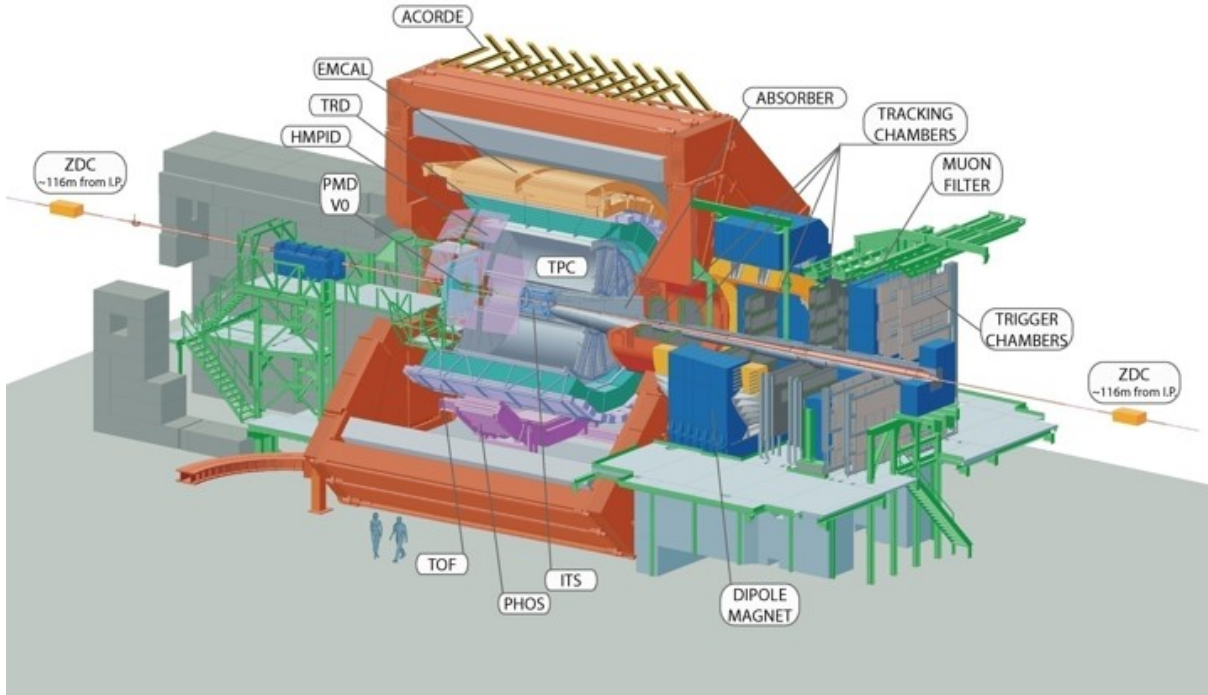


Figure 2.3: Overview of the ALICE detector

and two Silicon micro Strip Detectors (SSD) for the two outermost layers. The ITS practically contributes to all physics topics addressed by the ALICE experiment. That includes to improve the momentum and angle resolution for particles reconstructed by the Time Projection Chamber (TPC), and to reconstruct particles traversing dead regions of the TPC.

The TPC is the next subdetector system surrounding the ITS. It is the main tracking detector of the central barrel and is optimized to provide charged-particle momentum measurements with good two-track separation, particle identification and vertex determination. The next detector subsystem is the Transition Radiation Detector. Its main purpose is to provide identification of electrons with momenta higher than $1 \text{ GeV}/c$.

The Time Of Flight (TOF) is designed to provide particle identification in the intermediate momentum range. Together with ITS and TPC, TOF provides event-by-event identification of large samples of pions kaons and protons.

The following subdetector systems do not carry the full azimuthal range. They are The High Momentum-Particle Identification Detector (HMPID), the PHOTon Spectrometer (PHOS) and ElectroMagnetic CALorimeter (EMCAL), where both EMCAL and PHOS are electromagnetic calorimeters. Only one more subdetector system will be mentioned (although ALICE consists of more). The Zero Degree Calorimeter (ZDC) consists actually of two identical detectors each placed 116 m. away on either side of the interaction point. Its purpose is to measure the impact parameter of the collisions.

2.2.2 The Time Projection Chamber

The TPC is main tracking detector in ALICE. It is designed to handle an extreme charge particle multiplicity density of $\frac{dN_{ch}}{d\eta} = 8000$, leading to about 20000 primary and secondary tracks. No TPC has ever been able to handle this abundance of tracks before. It is built to cover a p_T range of $0.1 < p_T < 100 \text{ GeV}/c$. The TPC consists of a field cage with voltage gradient of about 400 V/cm and a high voltage of 100 kV electrode in the axial center (see figure (2.4)). Inside the 90 m^3 field cage is a gas consisting of 90% Ne and 10% CO_2 . When charged particles are traversing through the gas, the gas is ionised and the liberated electrons start drifting towards the end plates of the detector where they are registered by one of the 557568 readout pads. Depending on the momentum and charge of the particles, the trace will be more or less bent due to the magnetic field provided by the solenoid surrounding the detector. The bending of the particle trace and drifting of electrons is illustrated in figure (2.5). The maximum drift distance is 2.5 m . with a

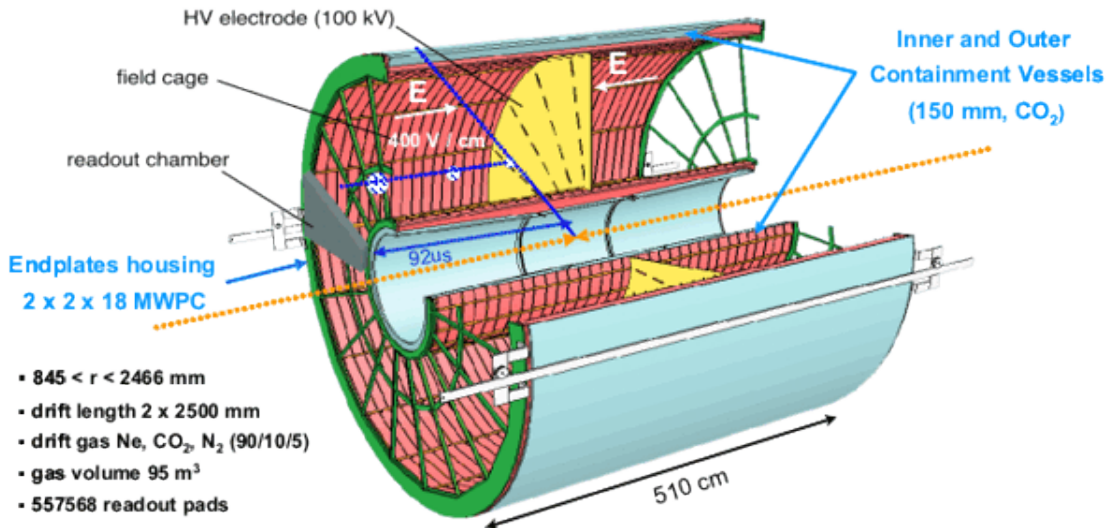


Figure 2.4: Sketch of the TPC subdetector system

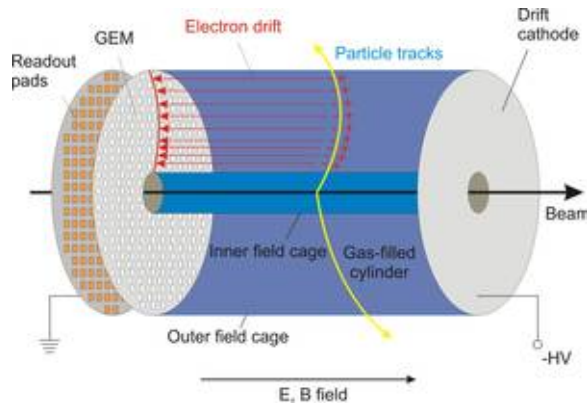


Figure 2.5: Drifting of electrons as they are ionised by the charged particle traversing the TPC. Note the bending of the trace due to the magnetic field.

maximum drift time of $92\mu\text{s}$. making the TPC the slowest detector in ALICE.

Chapter 3

Fourier expansion and Spherical harmonics

This chapter is devoted to the introduction of some of the mathematics used in this thesis. As it will be shown in chapter (4) certain aspects of the particle distribution can be approximated in terms of a Fourier series which is a one-variable continuous function given by a superposition of even and odd periodic functions. The advantage of using this form is that it is possible to investigate the degree of both local and global symmetries and antisymmetries of a given function or signal.

In this thesis the derivation of the Fourier series is achieved by computational power. This chapter will introduce the Fast Fourier Transform (FFT) which is a way of implementing some algorithms that allows for a faster calculation than the classical way of calculating the Fourier Series.

Since the Fourier series do only take one variable it can only describe the particle distribution in the plane. To describe a collision on a sphere the associated Legendre polynomial can be used in order to obtain spherical harmonics which is better suited for a description of the morphology of an entire collision. This chapter will give a description of the Fourier series, the Fourier transform and the discrete Fourier transform. A brief introduction to the FFT will be given, and finally the spherical harmonics will be reviewed.

3.1 The Fourier series

A function $f(x)$ may be expanded into a Fourier series if it satisfies the following conditions

- i) $f(x)$ must be periodic.
- ii) $f(x)$ must be single valued.
- iii) $f(x)$ must have only a finite number of maxima and minima within one period.
- iv) $\int_{x_0}^{x_0+L} |f(x)|dx < \infty$, where L is a constant satisfying that

$$f(x) = f(x + L) \tag{3.1}$$

[23]. Equation (3.1) is the definition of a periodic function. If $f(x)$ satisfy these conditions it can be expressed as

$$\begin{aligned} f(x) &= \frac{a_0}{2} + \sum_{n=1}^{\infty} [a_n \cos(\omega_n x) + b_n \sin(\omega_n x)] \\ &= \sum_{n=-\infty}^{\infty} c_n e^{i\omega_n x} \end{aligned} \quad (3.2)$$

where

$$\begin{aligned} a_n &= \frac{2}{L} \int_{x_0}^{x_0+L} f(x) \cos(\omega_n x) dx \\ b_n &= \frac{2}{L} \int_{x_0}^{x_0+L} f(x) \sin(\omega_n x) dx \end{aligned} \quad (3.3)$$

and

$$c_n = \frac{1}{L} \int_{x_0}^{x_0+L} f(x) e^{-i\omega_n x} dx \quad (3.4)$$

and

$$\omega_n = \frac{2n\pi}{L} \quad (3.5)$$

This is the conventional way of writing the Fourier series expansion of a function $f(x)$, where the right-hand side of equation (3.2) is the Fourier series, and equation (3.3) describes the Fourier coefficients.

The first of the conditions mentioned above, can be circumvented if the function under consideration is only over a finite interval. This is done by imagining a continuation of the function in such a way that it becomes periodic. However there are several ways of making this continuation resulting in different periods which will have to be taken into consideration when using equation (3.2), this is illustrated in figure (3.1).

3.1.1 Discrete Fourier Transformation

If $f(x)$ is nonperiodic and defined for all $x \in]-\infty; \infty[$ The Fourier series can not be achieved. Instead a Fourier transformation can be calculated. In this case $L \rightarrow \infty$ and accordingly $\Delta\omega \equiv \omega_n - \omega_{n-1} = \frac{2\pi}{L} \rightarrow 0$. Considering equation (3.4) this implies that the Fourier coefficients becomes continuous functions of ω , which eventually implies that the Fourier transform $\tilde{f}(\omega)$ is given by

$$\tilde{f}(\omega) = \int_{-\infty}^{\infty} f(x) e^{-i\omega x} dx \quad (3.6)$$

[23]. It appears from equation (3.6) that $\tilde{f}(\omega)$ is an expression for the strength of the complex sinusoids at a given frequency ω .

Sometimes $f(x)$ is not a continuous function, but a finite set of samples, at equally spaced values of x . This is more like the situation in particle physics, where the segmentation of the detector, only allows for a discrete description of the particle distribution.

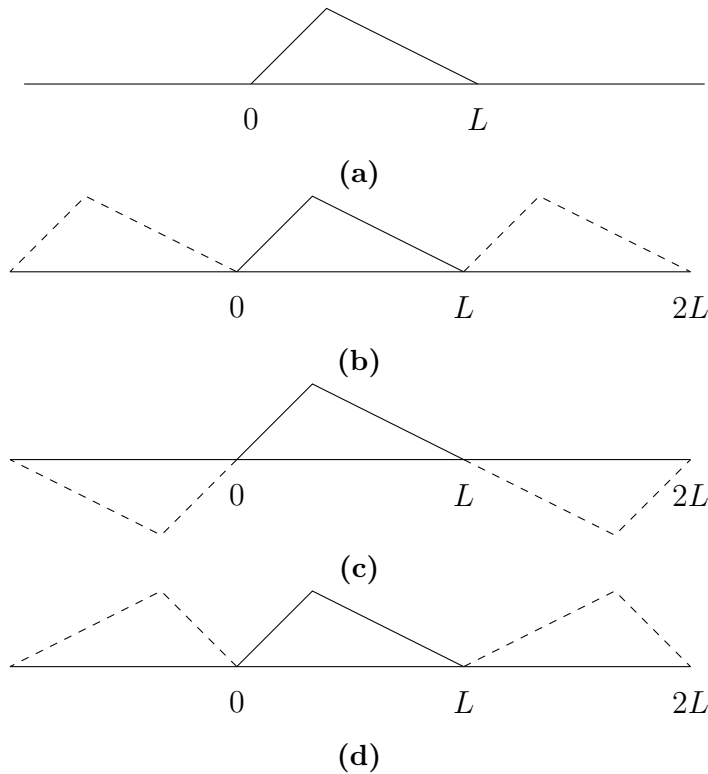


Figure 3.1: Different ways of extending a nonperiodic but finite ranged function.

This is a special case of equation (3.6). Under these conditions the Fourier transformation becomes

$$\tilde{f}(k) = \sum_{n=0}^{N-1} f_n \exp\left(\frac{-i2\pi kn}{N}\right) \quad (3.7)$$

Where N is the number of samples and f_n is the n 'th sample value or equivalently $f_n = f(x_n)$ where x_n is the x -value at the position of the n 'th sample. Each $\tilde{f}(k)$ represents the magnitude of the sine and cosine components with a given frequency. In principle any value of k is valid, but no more than N outputs can be used to determine the degree of symmetries and antisymmetries in a dataset. This is because each data sample is treated as a rectangular column. If there are more than N outputs, the Fourier transformation is fitted to the contours of the sample columns which contain no information.

The discrete Fourier transformation is a dataset of finite range which do not have to be periodic, hence the dataset is imaginatively extended to an infinite periodic set, the same way as was shown in figure (3.1b). The principles of the discrete Fourier transformation are shown in figure (3.2). It is seen that the columns represent a discrete set of values $f(x)$.

3.1.2 Fast Fourier Transform

The calculation of equation (3.6) requires N^2 multiplications. A Fast Fourier Transform (FFT) is an algorithm that reduces this number of operations by dividing the original

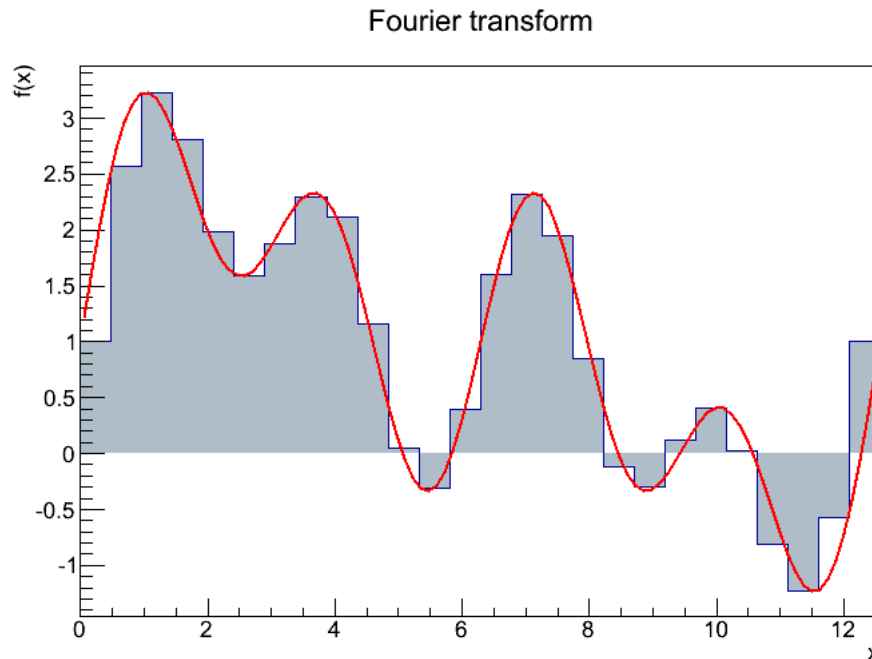


Figure 3.2: The principles of the discrete Fourier transform. The columns represent a data set with a finite number of samples. The curve is the approximated periodic function.

problem into smaller subproblems in such a way that

$$\sum \text{cost}(\text{subproblems}) + \text{cost}(\text{mapping}) < \text{cost}(\text{original problem}) \quad (3.8)$$

[24] meaning that the cost of the calculations of the subproblems plus the cost of gathering the solutions of the subproblems into one solution of the original problem, must not exceed the cost of the direct calculations needed to solve the original problem. In fact the use of FFT has allowed for a reduction of multiplications from N^2 to $N \log_2 N$ multiplications.

The FFT algorithm is not a specific algorithm. It is any algorithm that produces exactly the same result as the result of direct calculations of the discrete Fourier transform but with fewer calculations. Neither is there a specific algorithm which is the fastest. For a given dataset of N samples, the fastest way of making the Fourier transform depends on several things e.g. the size of N in the dataset and the platform on which the FFT is evaluated. One example of how the platform is relevant is the Winograd Fourier Transform which is designed to reduce to the number of floating point multiplications in the FFT. This is an advantage when using computational power. However the cost is a lot of extra additions and data transfers as compared to other FFT algorithms [25].

A mathematical derivation of the FFT will not be given in this thesis. It is not required to understand the underlying math of the FFT in order to understand the results, since the results of the FFT is exactly the same as the result of the direct calculations of the discrete Fourier transform.

3.2 Spherical harmonics

The spherical analogue of the Fourier Series is the Spherical Harmonics (SH) making it possible to analyse frequencies of the symmetries and the antisymmetries on a sphere. SH are used in a variety of fields, e.g. computation of the atomic electron configurations, and the solution of the Schrödinger equation in spherical coordinates. Of more relevance for this thesis, which will be apparent in chapter 5, is the use of SH in the analysis of cosmic microwave background.

The spherical harmonics are defined by

$$Y_l^m(\theta, \phi) = (-1)^m \sqrt{\frac{2l+1}{4\pi} \frac{(l-m)!}{(l+m)!}} P_l^m(\cos \theta) e^{im\phi} \quad (3.9)$$

where l and m are discrete numbers, with $-l \leq m \leq l$, and $P_l^m(\cos \theta)$ is the associated Legendre polynomial. For $m \geq 0$ $P_l^m(\cos \theta)$ is given by

$$P_l^m(x) = \frac{1}{2^l l!} (1-x^2)^{m/2} \frac{d^{l+m}}{dx^{l+m}} (x^2-1)^l \quad (3.10)$$

if $m < 0$ it can be calculated from equation (3.10) by the relation

$$P_l^{-m}(x) = (-1)^m \frac{(l-m)!}{(l+m)!} P_l^m(x) \quad (3.11)$$

[23]. A couple of things should be noted about equation (3.9). m determines the ϕ dependence, and consequently if $m = 0$ there is no dependence in ϕ . The dependence on θ is determined both by m and l . Thus only the case where $l = m = 0$ would have θ -dependence on $Y_l^m(\theta, \phi)$. It is mathematically allowed for l to be zero, in this case $Y_0^0(\theta, \phi) = \sqrt{\frac{1}{4\pi}}$ would be constant resembling a perfect sphere.

From equation (3.11) it is seen that

$$Y_l^{-m}(\theta, \phi) = (-1)^m [Y_l^m(\theta, \phi)]^* \quad (3.12)$$

where the asterisk denotes complex conjugation. Consequently it is common only to evaluate the SH for $m \geq 0$.

The SH are often visualized on a sphere, since the SH are derived to represent functions on the sphere. The disadvantage of this representation is that only half of the function can be seen on a 2-dimensional paper. Figure (3.3) shows the real part of the spherical harmonics for $l = 5$ and for $\{m \in \mathbb{N} | 0 \leq m \leq l\}$ drawn in a cartesian coordinate system where the sphere has been folded out on a plane. This allows for the functions to be fully visualized. The pattern remains the same when the imaginary part is included.

The SH form a complete set in the sense that any function of θ and ϕ can be expanded as a sum SH's. Thus a function $f(\theta, \phi)$ can be written as

$$f(\theta, \phi) = \int_{-1}^1 \int_0^{2\pi} = \sum_{l=0}^{\infty} \sum_{m=-l}^l a_{lm} Y_l^m(\theta, \phi) \quad (3.13)$$

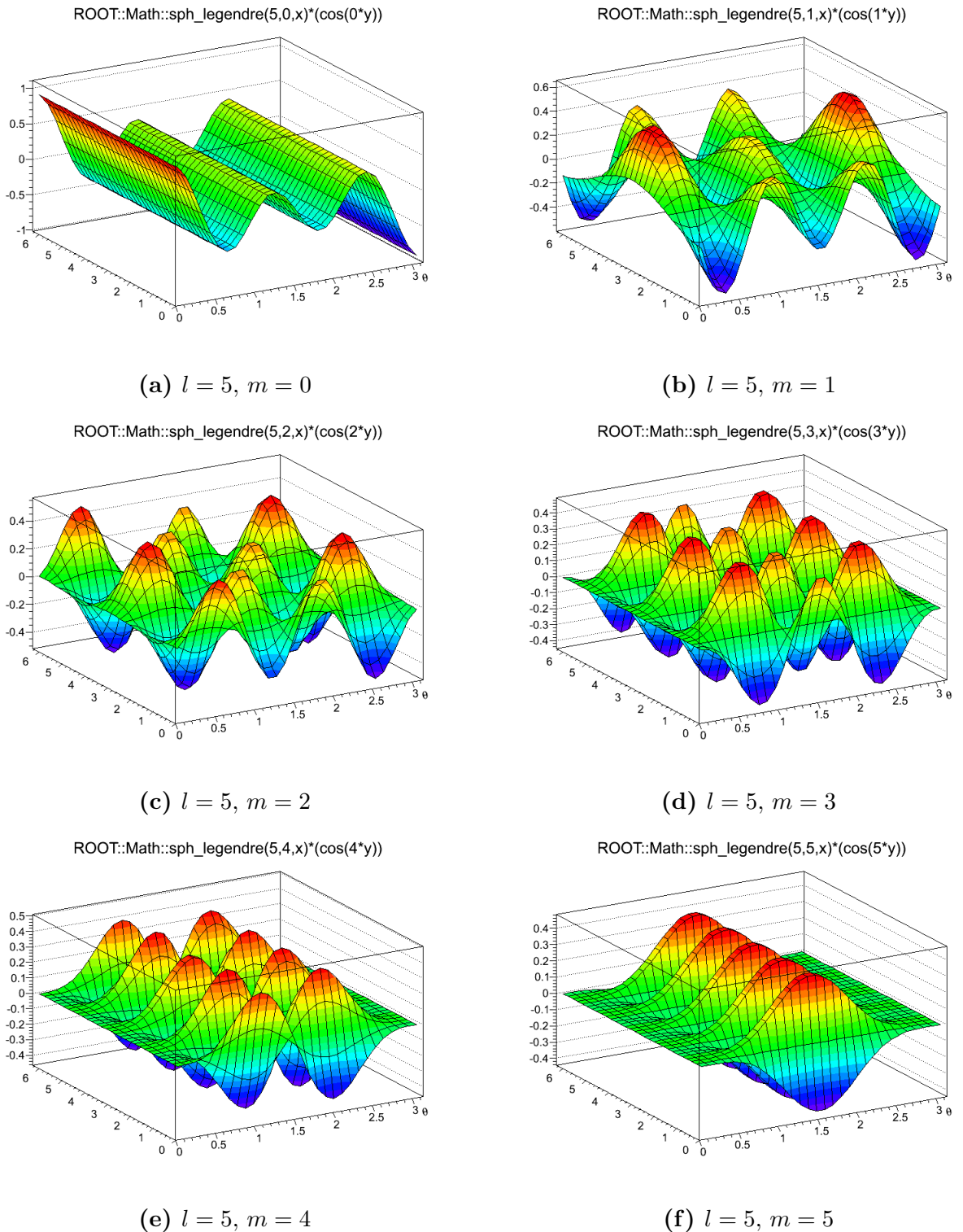


Figure 3.3: The spherical harmonics for $l = 5$ and all values of m . There is no dependence on ϕ for the $m = 0$ part. There is an increase of the multipoles in the ϕ -direction as m increases. The multipoles in the θ -direction decreases as a consequence of the higher order derivatives which eventually leave the θ -dependent part as a constant multiplied by $(1 - x^2)^{m/2}$ with $x = \cos \theta$.

where a_{lm} is a weight coefficient given by

$$a_{lm} = \int_{-1}^1 \int_0^{2\pi} [Y_l^m(\theta, \phi)]^* f(\theta, \phi) d\phi d \cos(\theta) \quad (3.14)$$

Thus the a_{lm} is of utmost importance when analysing a function, since it tells the degree of symmetry and antisymmetry at a given frequency. In equation (3.13) l is allowed to go to infinity. Just like in the discrete Fourier transform this does only make sense if the function $f(\theta, \phi)$ is a continuous function. If $f(\theta, \phi)$ is a finite discrete dataset l should not exceed the number of samples in $f(\theta, \phi)$.

Chapter 4

Anisotropic Flow

As discussed in chapter (1), a central collision at a given CM energy yields the highest particle production, and hence one a central collision is can be suspected as being of higher interest than a noncentral collision. Indeed for several years the central collisions has been the preferred [19]. However the noncentral collisions exhibit hydrodynamical properties which can not be observed in central collisions. These properties arises due to the geometry of the collision where the volume containing interacting matter is anisotropic in the azimuthal plane. The anisotropy can not be allowed in central collisions, since a (perfect) central collision is symmetric in all directions. In this chapter a definition and description of the collective anisotropic flow will be given. Since the results in this report are only concerned with the anisotropic flow which arises from non central collisions, very little attention will be devoted to the isotropic radial flow..

A physical description of the flow phenomenon and the motivation for studying this phenomenon, will primarily be described through flow of second order known as elliptic flow, although some higher order flows will also be reviewed briefly. The last part of this chapter will focus on the methods applied to determine the reaction plane and the amplitude of the flow.

4.1 The flow phenomenon

The phenomenon that a large number of particles moves either in a common direction or with a common velocity is referred to as collective flow [18]. This collective motion is present in a heavy ion collision due to the fact that a very dense zone of compressed nuclear matter is formed and hence a pressure from the inside creates an expanding fireball, as discussed in chapter (1). Flow signals the presence of multiple interactions between the particles produced in the collision. Interactions amongst the particles is exactly what is needed for thermalization so that the strength of the flow becomes a measurement of the degree of thermalization [20].

In the case of a very central collision the pressure gradient in both the azimuthal and polar angle will be approximately zero, and the flow will be isotropic in all directions. In a noncentral collision, the fireball will be almond shaped as shown in figure (4.1), and the flow will be anisotropic in the azimuthal direction. This anisotropy is experimentally observed as shown in figure (4.2), showing the correlation between any two particles. The

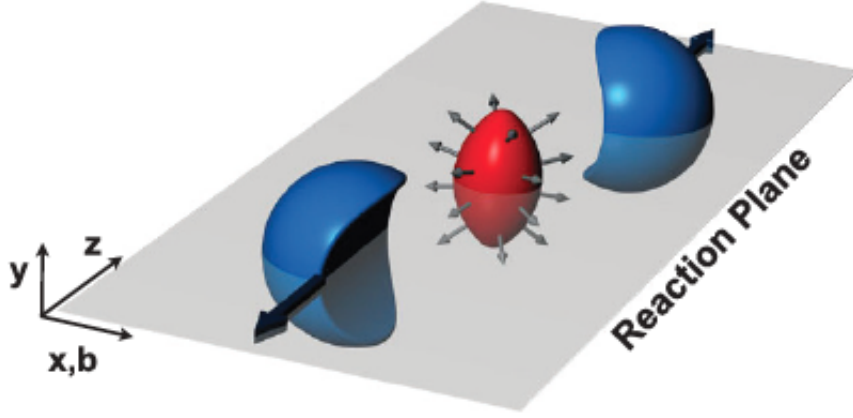


Figure 4.1: Noncentral collision giving rise to the elliptic flow due to an anisotropic pressure gradient in the azimuthal plane.

correlation is derived as

$$\mathcal{R} \equiv \frac{\langle N_a N_b \rangle - \langle N_a \rangle \langle N_b \rangle}{\langle N_a \rangle \langle N_b \rangle} \quad (4.1)$$

Where N_a and N_b denotes the number of particles of type a and b inside a given segment defined by its position and size in pseudorapidity and azimuthal angle [21]. The brackets denote the average over several events. The $\Delta\phi = \phi_a - \phi_b$ and $\Delta\eta = \eta_a - \eta_b$ along the y -axis is the separation between each segment corresponding to N_a and N_b . As it appears

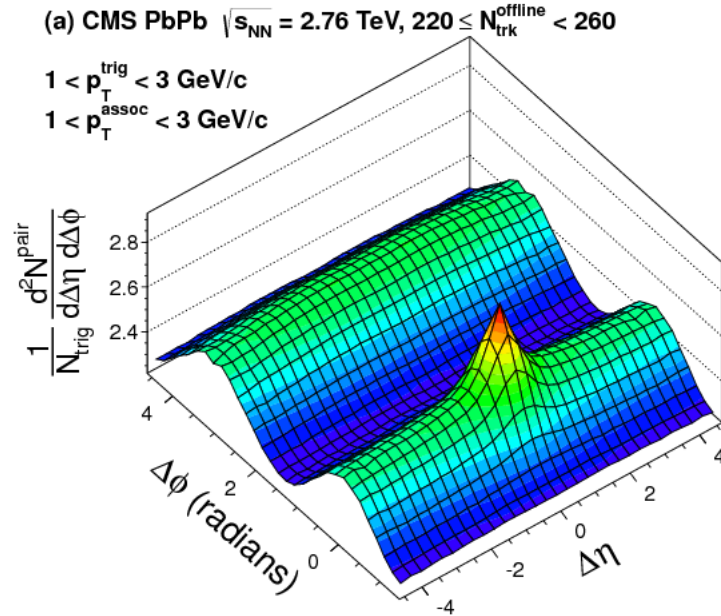


Figure 4.2: $\Delta\phi$ and $\Delta\eta$ distribution of a two particle correlation derived from equation (4.1). The nearside peak is due to jet correlations, the two ridges signify an elliptic flow

from the figure, there is a ridge around $\Delta\phi \approx 0$ and at $\Delta\phi \approx \pi$. The ridge around

$\Delta\phi \approx 0$ signifies that particles that propagates in very different directions with respect to the beam axis preserves a common direction of motion in the transverse plane, whereas the ridge around $\Delta\phi \approx \pi$ signifies that this motion is symmetric in the transverse plane. This is a result of the anisotropy shown in figure (4.1). The pressure inside the fireball is the same in all directions. But since the pressure is spread over a larger distance along the major axis as compared to the minor axis, the result is an effectively higher pressure gradient along the minor axis. The result is an excess of particles along the minor axis. This kind of flow is known as *Elliptic flow*, and is described mathematically as

$$\frac{dN}{d\phi} \propto 1 + 2v_2 \cos 2\phi \quad (4.2)$$

[21], where v_2 is a measurement of the magnitude of the elliptic flow. Although the equation do only contain a dependency on ϕ , the elliptic flow may still be dependent on η [50].

4.1.1 Fourier expansion of the collective flow

The anisotropic flow only gives rise to an anisotropy in the azimuthal plane, consequently flow is only described by the variable ϕ as a function of particles in the azimuthal plane. Let $f(\phi)$ be the function that describes the particle distribution in the azimuthal plane. The particle distribution is defined in the finite interval between 0 and 2π so that $f(\phi)$ can be Fourier expanded by equation (3.2) to give

$$f(\phi) = \frac{a_0}{2} + \sum_{n=1}^{\infty} a_n \cos(n\phi) \quad (4.3)$$

[28], where a_n is given by equation (3.3). Equation (4.3) do only apply for the case where the colliding nuclei are identical. The sine term is eliminated because the probabilities of particle emission in the ϕ and $-\phi$ direction are equal.

Equation (4.3) has two important features, the first is: that if $n = 2$ it is quite similar to equation (4.2). When $n = 2$, then $f(\phi)$ will have two periods as illustrated in figure (4.3), which is similar to the case of elliptic flow. The second order term of equation

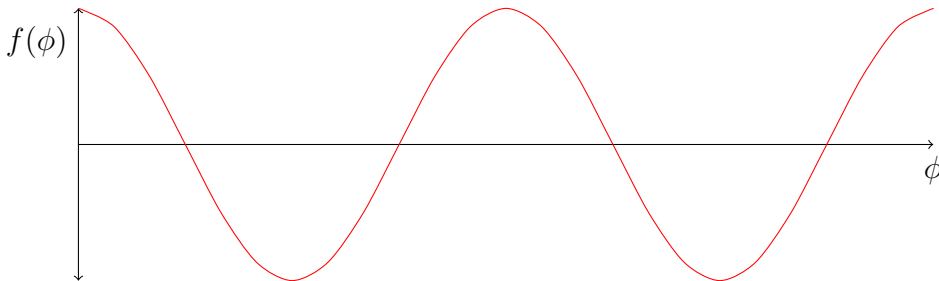


Figure 4.3: $v_2 \cos(2\phi)$

(4.2) is not exactly the same as (4.3) because (4.2) is written in the conventional form of describing the flow whereas equation (4.3) is the conventional form of the Fourier expansion. In flow analysis the most general form of writing the particle distribution in

the azimuthal plane is given by

$$f(\phi) = 1 + 2 \sum_{n=1}^{\infty} v_n \cos[n(\phi - \psi_n)] \quad (4.4)$$

[20]. Equation (4.4) equals equation (4.3) when v_n is chosen properly. The ψ_n term present in equation (4.4) is the angular orientation of the reaction plane.

The second feature of equation (4.3) is that there is an infinite amount of terms in the Fourier expansion. However the reason for the anisotropy is the almond shaped fireball as described above, and it seems natural that the term $n = 2$ would be the only term present in the expansion. The other terms arises due to the fact that the nucleons inside the nucleus are not evenly distributed. Consequently the overlapping region of the nuclei is not strictly ellipsoidal which will lead to other terms of fluctuations in the particle distribution. Figure (4.4) shows how the uneven nucleon distribution inside two colliding nuclei leads to an overlap region that may be approximated with an elliptical or triangular shape, and one may continue with higher orders. When considering the event as shown in figure (4.4) as opposed to the clear cut situation in figure (4.1), the reaction plane is referred to as symmetry plane. It is not necessary that the angle of the symmetry plane is the same for various orders. Furthermore due to the periodicity of the flow orders, it only makes sense to describe the symmetry plane in the range $0 \leq \psi_n \leq 2\pi/n$. Until now the highest measured flow order has been $n = 8$ and is significant up to order the $n = 6$ [32].

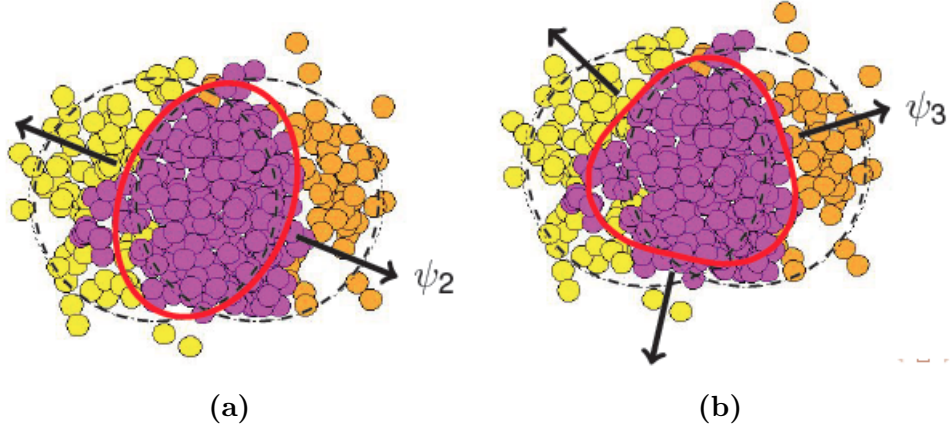


Figure 4.4: Illustration of how the uneven nucleon distribution inside the nuclei in a collision may be considered as elliptic or triangular flow. The arrow indicate the orientation of the symmetry plane.

4.1.2 Motivation for studying elliptic and higher order flow

It was briefly mentioned in chapter 1 that after thermalization the system might be described through a perfect fluid hydrodynamical model. The observation of higher order flow harmonics [33] makes the assertion that the QGP can be considered as a perfect fluid very likely since it does not absorb the fluctuations from the higher harmonics. The hydrodynamical model is better suited for central than peripheral collisions. The

hydrodynamical description is dependent on an equation of state, and the initial conditions of the collision. The initial conditions include the time t_0 at which the system thermalizes, the baryon density and the viscosity of the produced fluid.

In most collisions the elliptic flow is the largest coefficient. Therefore it is advantageous to study this part of the flow. The reason is that elliptic flow is strongly dependent on the geometry of the collision and less dependent on other parameters of the hydrodynamic model. This makes it possible to compare results from elliptic flow to the hydrodynamic model and gain information about the unknown parameters. In particular elliptic flow can be used as an indicator for the degree of thermalization [34] by studying the viscosity of the system. A higher viscosity would quickly reduce the magnitude of the flow. Figure (4.5) shows how the eccentricity of various flow orders varies with centrality, where the eccentricity ϵ is a term describing the deviations from a spherical shape. The eccentricity is given by

$$\epsilon_1 e^{i\psi_1} \equiv \frac{\int r^3 e^{i(\phi-\psi_1)} e(r, \phi) r dr d\phi}{\int r^3 e(r, \phi) r dr d\phi} \quad \text{and} \quad \epsilon_n e^{in\psi_n} \equiv -\frac{\int r^n e^{in(\phi-\psi_n)} e(r, \phi) r dr d\phi}{\int r^n e(r, \phi) r dr d\phi}, \quad n > 1 \quad (4.5)$$

where $e(r, \phi)$ is the initial energy density distribution in the azimuthal plane. Here the

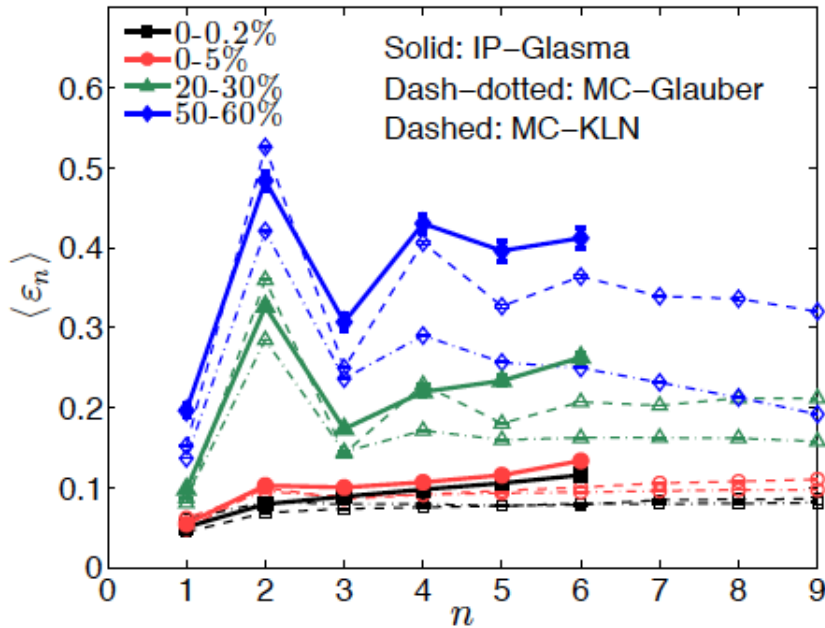


Figure 4.5: The flow dependence on eccentricity. Eccentricity as defined in equation (4.5) is calculated under different initial conditions represented by different signatures of the curve. Eccentricity depends on both the centrality and the initial conditions [35].

actual viscosity is not calculated, but an average over time of the evolution of the fireball is calculated. The fact that the viscosity is not constant is a consequence of the viscosity being affected by the temperature of the system. As the fireball expands the system is cooled and viscosity is increased.

The hadronic state occurring after the QGP may significantly distort the determination of the viscosity as the actual measurement of the flow only takes place after the

phase transition. However an increased CM energy increases the lifetime of the QGP and hence reduces the uncertainty on the measurement. By observing the energy dependence of elliptic flow, the contributions from the hadronic and the QGP phases can be varied and the temperature dependence of viscosity can be investigated.

In principle the flow order n could range infinitely but the shear viscosity dampens the differences in expansion velocities and thus dampens the flow coefficients. But higher flow order coefficients are attenuated more than low flow orders. Thus higher order flow calculations may also be an important tool in determining the viscosity of the QGP. Figure (4.6) shows the flow coefficients variation with centrality. The elliptic flow vary rapidly with centrality whereas v_3 and v_4 has a rather weak centrality dependence.

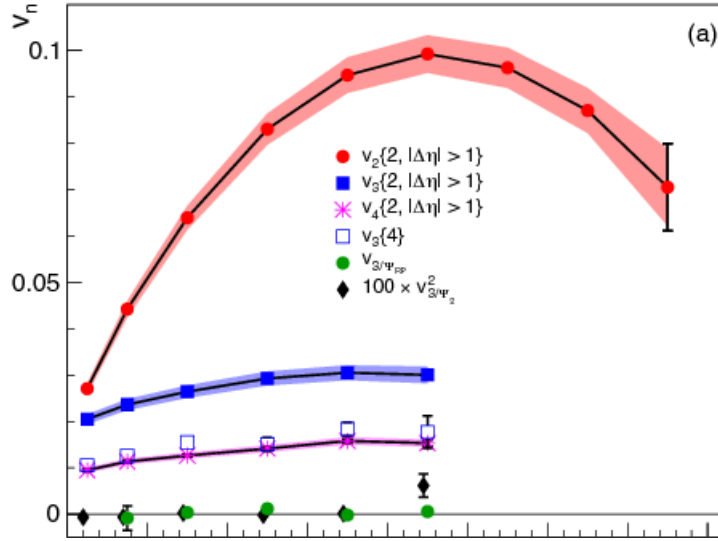


Figure 4.6: Centrality dependence on higher order flow calculated with a two particle correlation (red dots, filled blue squares and pink stars) for the v_2 to v_4 flow, and a four particle correlation (empty blue squares) for the v_3 flow. The x axis run between 0 and 80%

4.1.2.1 Importance of the reaction plane

For the flow coefficients v_2 and v_3 there is to a good approximation a proportionality to the eccentricity ϵ_2 and ϵ_3 . But when encountering higher orders the hydrodynamic model predicts that as the fireball evolve there will be a mixing between the various flow order harmonics thus making v_4 dependent on v_2 and v_5 dependent on v_3 . This results in a change in the reaction plane of flow which is not the same as the reaction plane for eccentricity. In other words ψ_n does not have the same value in equation (4.5) as in equation (4.4). A study of the correlation between the reaction planes may help to determine both the initial conditions of the collision and the shear viscosity [36].

4.2 Methods of flow analysis

There are several ways of calculating the flow coefficients. The original way has been *the event plane method*, where the reaction plane is needed in order to calculate the flow coefficients. But more recent methods known as the cumulant methods considers

the position of the individual nucleons inside the nuclei. The reaction plane method considers the position of particles with respect to the reaction plane which is determined by considering the position of the two colliding nuclei, whereas the cumulant method considers the flow with respect to a participant plane which is determined from the shape of the system of the individual colliding particles form as illustrated in figure (4.7). A

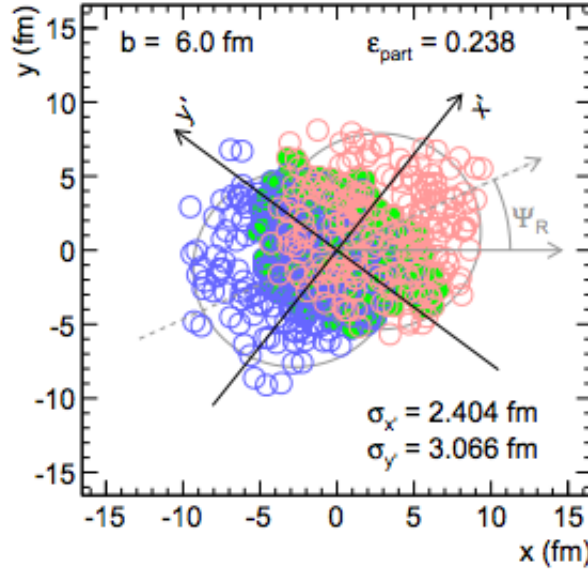


Figure 4.7: Participant plane derived from the position of the individual nucleons. The image shows that the participant plane is slightly rotated with respect to the reaction plane. Generally the participant plane fluctuates around the reaction plane.

description of the three most frequently used methods will be given below. The fact that the flow is not estimated from one method but several can lead to confusion since they do not yield the same result and thus are not directly comparable. The confusion is even further increased with the fact that there are different kinds of flow:

Differential flow: Generally there is a dependence of the flow coefficients on the transverse momentum and rapidity. In this case flow is only calculated with specific class of selected particles satisfying a set of predefined conditions. E.g. one flow coefficient could be calculated only for particles with $1.9 < p_T < 2.1$, and other similar p_T windows would be used in order to obtain flow coefficients for the entire range of p_T .

Integrated flow: Integrated flow is obtained through explicit integration of differential flow with respect to p_T or y . Integrated flow is often visualized with a dependence on centrality.

Reference flow: The reference flow is used in the calculation of cumulants (subsection 4.2.4), where it functions as a reference for the differential flow. It is needed due to limited statistics in each narrow p_T window where differential flow is calculated which prevents calculation of differential flow only by taking particles from that narrow window.

4.2.1 Determination of the event plane

In order to determine the flow coefficients in the reaction plane method, the orientation of the reaction plane is needed. However due to a limited particle production the true reaction plane cannot be found experimentally. Hence in the following there will be a distinction between the “reaction plane” (ψ_n^{RP}) and the “event plane” (ψ_n^{EP}), where the reaction plane denotes the true reaction plane and the event plane means the experimentally estimated reaction plane. If it is clear from the context whether it is the reaction plane or the event plane which is under consideration, the superscript will be omitted.

The reaction plane can be calculated from the event flow vector $\vec{Q}_n = (Q_{x,n}, Q_{y,n})$ defined by

$$\begin{aligned} Q_{x,n} &= |\vec{Q}_n| \cos(n\psi_n^{EP}) \equiv \sum_i^M \omega_i \cos(n\phi_i) \\ Q_{y,n} &= |\vec{Q}_n| \sin(n\psi_n^{EP}) \equiv \sum_i^M \omega_i \sin(n\phi_i) \end{aligned} \quad (4.6)$$

which leads to

$$\psi_n^{EP} = \frac{1}{n} \arctan \left(\frac{\sum_i \omega_i \sin(n\phi_i)}{\sum_i \omega_i \cos(n\phi_i)} \right) \quad (4.7)$$

[37], where the sum runs over all detected particles M , and ω_i are weights. In the following the slight simplification is made that $|\vec{Q}_n| = Q$. In a symmetric collision reflection symmetry demands the same particle distribution in the forward hemisphere as in the backward hemisphere when shifting the azimuthal angle of all particles with π . Consequently the weights of all odd harmonics will have a reversal in sign for all particles in the backward hemisphere. The magnitude of ω_i can vary depending on which effect of the flow is under consideration and which effects (e.g. detector acceptance) needs to be eliminated.

4.2.2 The reaction plane method

Using the event plane as an estimation of the differential flow harmonics can be obtained. The definition of the differential flow harmonics involves the reaction plane

$$v_n \equiv \langle \cos[n(\phi - \psi_n^{RP})] \rangle \quad (4.8)$$

[38], where the brackets denotes the average over particles and events. Since the reaction plane ψ_n^{RP} is not known, the event plane will have to be used instead leading to an observed flow coefficient v_n^{Obs} which can be corrected in order to give an estimation of the true flow coefficient. v_n^{Obs} is given by

$$v_n^{Obs} = \langle \cos[n(\phi - \psi_n^{EP})] \rangle \quad (4.9)$$

and the estimation for the true flow coefficient will be given by

$$v_n^{true} = \frac{1}{R} v_n^{Obs} \quad (4.10)$$

[38], where R is the event plane resolution. If the procedure is applied in a narrow window the differential flow is obtained. The event plane resolution is derived from various sub-events, where a sub-event means a subgroup of particles in an event e.g. all particles in a certain rapidity range. For each of the sub-events an event plane is determined and the event plane resolution is given by

$$R = \langle \cos[n(\psi_{n,a}^{EP} - \psi_n^{RP})] \rangle = \sqrt{\frac{\langle \cos[n(\psi_{n,a}^{EP} - \psi_{n,b}^{EP})] \rangle \langle \cos[n(\psi_{n,a}^{EP} - \psi_{n,c}^{EP})] \rangle}{\langle \cos[n(\psi_{n,b}^{EP} - \psi_{n,c}^{EP})] \rangle}} \quad (4.11)$$

[37], where the subscripts a, b, c are included because the event planes are calculated for various sub-events. The brackets denote average over events. Thus in order to calculate the event plane resolution three sub-events is required. This can be reduced to two if further information is known about the sub-events e.g. the sub-events are of equal multiplicity. Figure (4.8) shows the event plane resolution as a function of centrality for the second order flow harmonic.

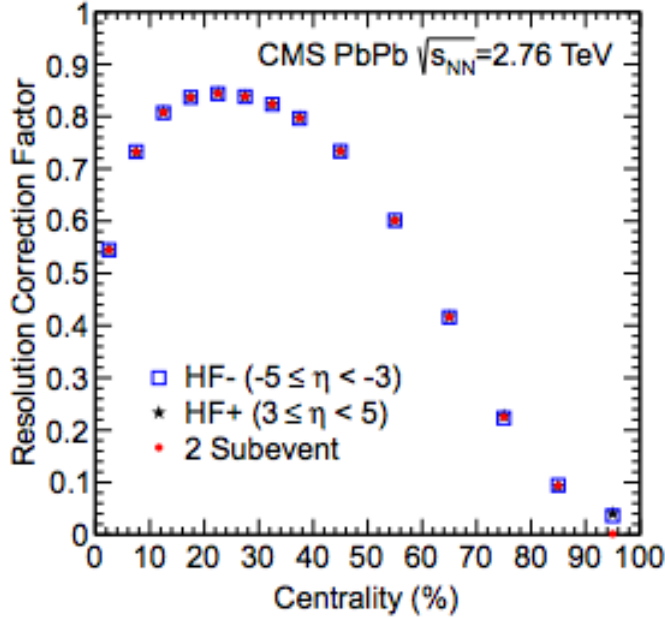


Figure 4.8: The event plane resolution for the second flow harmonic as a function of centrality [39].

When using the event plane method, it is important to remove autocorrelations. This is done by assuming that the contribution from momentum conservation is small. When a particle has been used in the calculation of an event plane the autocorrelation effect in its distribution with respect to this plane is removed by recalculating the event plane without the particle.

4.2.3 Non-flow

One of the weaknesses about the event plane method is that there may be several possible sources of azimuthal correlation which are unrelated to the reaction plane and the initial

geometry of the system. These correlations are known as non-flow effects. The origin of the non-flow effects includes resonance decays, dijets, coulomb effect or momentum conservation along with others. Very often the contribution from non-flow effects scales as $1/M$ where M is the multiplicity of particles used to determine the event plane. However this can not be taken as a general rule, for instance the contributions due to momentum conservation increases with the fraction of particles detected when using the event plane method.

Generally non-flow effects are too large to be negligible and must be suppressed. Although there are tools developed for the suppression of non-flow effects in the event plane method [42], it cannot be done in a systematic manner. This has motivated developments of other methods where contribution from non-flow effects is vanishing. Generally non-flow effects only involve correlations between more than three particles, so the idea is to study flow by studying genuine multi-particle correlations. This can be done in two ways. Either by the cumulant method or by the Lee-Yang zeroes method, both of which considers correlations between the produced particles.

4.2.4 The cumulant method

The cumulant method takes its offspring in the idea that if there exist a correlation between the produced particles and the orientation of the reaction plane, then there must exist a correlation amongst the produced particles themselves. Using this method the anisotropic flow develops relative to the participant plane as shown in figure (4.7) instead of the reaction plane. The method has two steps: the first is to calculate the reference flow and then the reference flow is used in the second step, which is to determine the differential flow harmonics defined in equation (4.8). A weighted average of the p_T dependent differential flow can be calculated to obtain the integrated flow.

4.2.4.1 Reference flow

In order to determine the differential flow, the reference flow must be determined. The reference flow is determined using correlations between all detected particles. From these correlations the n 'th order cumulant which is closely related to the reference flow, can be determined. Although in principle any number of particles could be used in the cumulant determination, it is customary only to use two or four particle cumulants in the study of elliptic flow. Higher order cumulants could be used, but with little advantage since they do not suppress systematic uncertainties better than four-particle cumulants. However second order cumulants are affected by non-flow effects. As the non-flow effects on fourth order cumulants are vanishing, a comparison between second- and fourth order cumulants may be advantageous.

The single event averaged two particle azimuthal correlation is defined as

$$\langle 2 \rangle \equiv \langle e^{in(\phi_1 - \phi_2)} \rangle = \frac{(M-2)!}{2!} \sum_{i,j=1}^M e^{in(\phi_i - \phi_j)} \quad (4.12)$$

and similarly the four particle correlation is defined as

$$\langle 4 \rangle \equiv \langle e^{in(\phi_1+\phi_2-\phi_3-\phi_4)} \rangle = \frac{(M-4)!}{4!} \sum'_{i,j,k,l=1}^M e^{in(\phi_i+\phi_j-\phi_k-\phi_l)} \quad (4.13)$$

where M is the number of particles. The prime in the sum means that indices in the sum must be taken different. These functions can easily be generalized to six- and eight particle correlations. Equation (4.12) can be averaged over all events to obtain

$$\langle\langle 2 \rangle\rangle \equiv \langle\langle e^{in(\phi_1-\phi_2)} \rangle\rangle \equiv \frac{\sum_i^N (W_{\langle 2 \rangle})_i \langle 2 \rangle_i}{\sum_i^N (W_{\langle 2 \rangle})_i} \quad (4.14)$$

and

$$\langle\langle 4 \rangle\rangle \equiv \langle\langle e^{in(\phi_1+\phi_2-\phi_3-\phi_4)} \rangle\rangle \equiv \frac{\sum_i^N (W_{\langle 4 \rangle})_i \langle 4 \rangle_i}{\sum_i^N (W_{\langle 4 \rangle})_i} \quad (4.15)$$

where the $W_{\langle m \rangle}$ are event weights inferred to minimize the effect of multiplicity variation and N is the number of events. The procedure is the same for higher order correlations. If the multiplicity is not the same in all events the event weights may advantageously be chosen as

$$W_{\langle m \rangle} = \frac{M!}{(M-m)!} \quad (4.16)$$

in order to minimize the statistical spread. If the detector has uniform acceptance, equation (4.14) describes the second order cumulant $c_n\{2\}$ such that

$$c_n\{2\} = \langle\langle 2 \rangle\rangle \quad (4.17)$$

and the fourth order cumulant can be written as

$$c_n\{4\} = \langle\langle 4 \rangle\rangle - 2\langle\langle 2 \rangle\rangle^2 \quad (4.18)$$

Equation (4.17) and (4.18) eventually leads to the determination of the reference flow given by

$$v_n\{2\} = \sqrt{c_n\{2\}} \quad (4.19)$$

and

$$v_n\{4\} = \sqrt[4]{-c_n\{4\}} \quad (4.20)$$

The last two equations are the conventional way of determining the reference flow as described in [41], however the calculations do need a lot of computational power especially for the higher order cumulants due to the summations. Furthermore the method do not take into account that the acceptance of the detector may not be uniform.

The generalized form of the second order cumulant which do also contain corrections for non-uniform acceptance in the detector is given by

$$c_n\{2\} = \langle\langle 2 \rangle\rangle - \langle\langle \cos(n\phi) \rangle\rangle^2 - \langle\langle \sin(n\phi) \rangle\rangle^2 \quad (4.21)$$

The generalized fourth order cumulants is given in appendix A.

In order to reduce the calculations of (4.19) and (4.20) it has been suggested to express the correlations in terms of the flow vector defined in equation (4.6). For the sake of simplicity it can be written in complex numbers as

$$Q_n \equiv \sum_{i=1}^M \omega_i e^{in\phi_i} \quad (4.22)$$

A reasonable choice of weight would $\omega = p_T$. In the following calculations Q_n will be treated with ω_i being unity.

The square of the vector can be rewritten as

$$|Q_n|^2 = Q_n Q_n^* = \sum_{i,j=1}^M e^{in(\phi_i - \phi_j)} = M + \sum'_{i,j=1}^M e^{in(\phi_i - \phi_j)} \quad (4.23)$$

from which $\langle 2 \rangle$ can be expressed as

$$\langle 2 \rangle = \frac{|Q_n|^2 - M}{M(M-1)} \quad (4.24)$$

The single event averaged four particle correlation is given in terms of

$$|Q_n|^4 = Q_n Q_n Q_n^* Q_n^* = \sum_{i,j,k,l=1}^M e^{in(\phi_i + \phi_j - \phi_k - \phi_l)} \quad (4.25)$$

It is a little more cumbersome because it includes four distinct cases for the indices i, j, k, l . One where all indices are different from each other, one where two are equal, one where three are equal and one where they are all equal. This finally leads to an expression for $\langle 4 \rangle$ given by

$$\langle 4 \rangle = \frac{|Q_n|^4 + |Q_{2n}|^2 - 2 \cdot \text{Re} [|Q_{n2} Q_n^* Q_n^*]}{M(M-1)(M-2)(M-3)} - 2 \frac{2(M-2) \cdot |Q_n|^2 - M(M-3)}{M(M-1)(M-2)(M-3)} \quad (4.26)$$

Equation (4.24) and (4.26) may be inserted into (4.14) and (4.15) in order to obtain the reference flow. This is a less computationally demanding method. But equation (4.26) also shows the interference between different order harmonics, and thus is a crucial tool in disentangling these interferences.

4.2.4.2 Differential flow

The reference flow can be used to determine the differential flow. This means that the determination of differential flow is a two step operation, firstly the reference flow is determined and secondly the differential flow will be estimated with respect to the reference flow. Particles used in the calculations for the reference flow are labelled Reference Flow Particles (RFP) and particle used in the calculations of the differential flow taken from some phase window are labelled as Particles Of Interest (POI). Particles labelled as RFP and POI may not always be distinct. The azimuthal angel of RFP is denoted by ϕ , where

as the azimuthal angle of POI is denoted by Φ . With this notation the *reduced single event average* two- and four-particle correlations can be defined as

$$\langle\langle 2' \rangle\rangle \equiv \langle e^{in(\Phi_1 - \phi_2)} \rangle \equiv \frac{1}{m_p M - m_q} \sum_{i=1}^{m_p} \sum_{j=1}^{M'} e^{in(\Phi_i - \phi_j)} \quad (4.27)$$

$$\langle\langle 4' \rangle\rangle \equiv \langle e^{in(\Phi_1 + \phi_2 - \phi_3 - \phi_4)} \rangle \quad (4.28)$$

$$\equiv \frac{1}{(m_p M - 3m_q)(M-1)(M-2)} \sum_{i=1}^{m_p} \sum_{j,k,l=1}^{M'} e^{in(\Phi_i + \phi_j - \phi_k - \phi_l)} \quad (4.29)$$

where m_q is the number of particle labelled both as RFP and POI and m_p is the number of particle labelled as POI. The prime in the sum have a slightly different meaning as compared to equation (4.12) and (4.13), the sum is over distinct particles meaning that even a particle labelled both as RFP and POI can not appear twice in one term of the sums. The *event averaged reduced* two and four particle correlations can be defined as

$$\langle\langle 2' \rangle\rangle \equiv \frac{\sum_{i=1}^N (w_{\langle 2' \rangle})_i \langle 2' \rangle_i}{\sum_{i=1}^N (w_{\langle 2' \rangle})_i} \quad (4.30)$$

$$\langle\langle 4' \rangle\rangle \equiv \frac{\sum_{i=1}^N (w_{\langle 4' \rangle})_i \langle 4' \rangle_i}{\sum_{i=1}^N (w_{\langle 4' \rangle})_i} \quad (4.31)$$

Where the weights w_i , inferred for the case of multiplicity fluctuations, may be advantageously chosen as

$$w_{\langle 2' \rangle} = m_p M - m_q \quad (4.32)$$

$$w_{\langle 4' \rangle} = (m_p M - 3m_q)(M-1)(M-2) \quad (4.33)$$

which takes into account the number of different particle combinations used to evaluate all correlations used to evaluate all correlations.

Like with the reference flow, the number of mathematical operations can be reduced by the use of the Q vector defined in equation (4.22) (with the weights omitted), but two additional vectors have to be introduced to take into account the distinction between particles labelled only as POI, and particles labelled both as POI and RFP. Thus the vector p_n is defined as

$$p_n \equiv \sum_{i=1}^{m_p} e^{in\Phi_i} \quad (4.34)$$

and the vector q_n is defined as

$$q_n \equiv \sum_{i=1}^{m_q} e^{in\Phi_i} \quad (4.35)$$

in analogue to the reference flow $\langle 2' \rangle$ is given by

$$\langle 2' \rangle = \frac{p_n Q_n^* - m_q}{m_p M - m_q} \quad (4.36)$$

which may be inserted into equation (4.30) to obtain $\langle\langle 2' \rangle\rangle$. And the reduced four-particle correlations may be written as

$$\begin{aligned} \langle 4' \rangle = & \frac{p_n Q_n Q_n^* Q_n^* - q_{2n} Q_n^* Q_n^* - p_n Q_n Q_{2n}^* - 2M p_n Q_n^* - 2m_q |Q_n|^2}{(m_p M - 3m_q)(M-1)(m-2)} \\ & + \frac{7q_n Q_n^* - Q_n q_n^* + q_{2n} Q_{2n}^* + 2p_n Q_n^* + 2m_q M - 6m_q}{(m_p M - 3m_q)(M-1)(m-2)} \end{aligned} \quad (4.37)$$

With uniform detector acceptance the differential flow cumulants are given as

$$d_n \{2\} = \langle\langle 2' \rangle\rangle \quad (4.38)$$

and

$$d_n \{4\} = \langle\langle 4' \rangle\rangle - 2 \cdot \langle\langle 2' \rangle\rangle \langle\langle 2' \rangle\rangle \quad (4.39)$$

Estimates of the differential flow are then given by

$$v_n' \{2\} = \frac{d_n \{2\}}{\sqrt{c_n \{2\}}} \quad (4.40)$$

and

$$v_n' \{4\} = -\frac{d_n \{4\}}{\sqrt[4]{-c_n \{4\}^3}} \quad (4.41)$$

Whereas the generalized second order differential cumulants are given by

$$d_n \{2\} = \langle\langle 2' \rangle\rangle - \langle\langle \cos(n\Phi_1) \rangle\rangle \langle\langle \cos(n\phi_2) \rangle\rangle - \langle\langle \sin(n\Phi_1) \rangle\rangle \langle\langle \sin(n\phi_2) \rangle\rangle \quad (4.42)$$

The generalized fourth order cumulants can be found in appendix (A). The number of mathematical operations in the generalized forms of both the reference flow and the differential flow may be reduced by the use of the Q , q and p vectors. This is described in the appendix of [40].

The estimated differential flow in a Pb-Pb collision with center of energy $\sqrt{s_{NN}} = 2.76$ TeV plotted against the transverse momentum is shown in figure (4.9) for different centralities. The fourth order cumulant is generally lower than the second order cumulant, because the cumulants have different sensitivity to event-by-event fluctuations and because the fourth order cumulant is nearly unaffected by the non-flow effects.

4.2.4.3 Integrated flow

Integrated flow is defined as a weighted average with the invariant distribution used as a weight

$$v_n \equiv \frac{\int_0^\infty v_n(p_T) \frac{dN}{dp_T} dp_T}{\int_0^\infty \frac{dN}{dp_T} dp_T} \quad (4.43)$$

By the use of integrated flow, flow can be estimated with respect to centrality. Figure (4.10) shows the flow of figure (4.9) integrated with respect to p_T with the limits $0.2 < p_T < 5.0$ GeV/c plotted against the centrality.

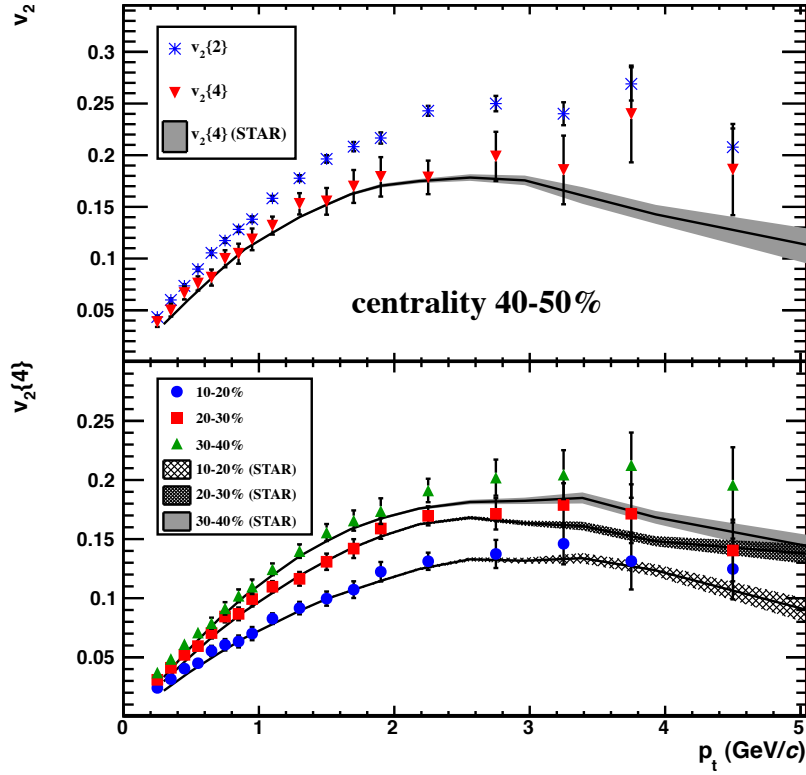


Figure 4.9: Differential flow in Pb-Pb collisions with center of mass energy $\sqrt{s_{NN}} = 2.76$ TeV plotted against the transverse momentum

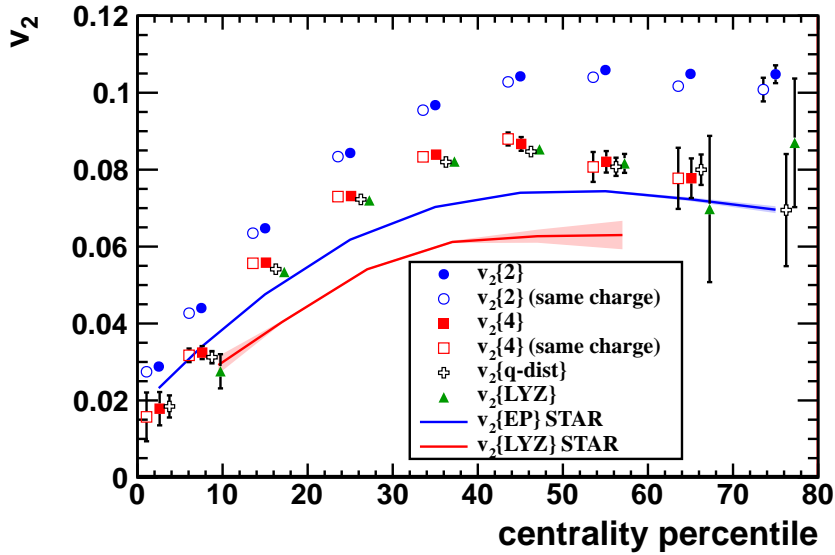


Figure 4.10: Elliptic flow integrated with respect to p_T with the limits $0.2 < p_T < 5.0$ GeV/c plotted against the centrality.

4.2.5 Lee-Yang zeroes method

The Lee-Yang Zeroes (LYZ) method is named after the authors (T. D. Lee and C. N. Yang) [43] of the theory of phase transition to which it might be resembled. Contrary to the cumulant method which do only study a finite order of correlations typically ranging between two and eight, the approach in the LYZ method is to study a large (in principle infinite) order of cumulants. In spite of the advantages of the cumulant- and LYZ method (suppression of non-flow effects), the most dominating method is still the event-plane method partly because it is more intuitive and partly because it is more handy. However as shown in subsection (4.2.4) the introduction of the flow vector to the calculations has also made the cumulant method handy. The LYZ method described below is the method introduced in [44], but the mathematical formality has been altered to resemble that of the event plane method [45] and thus is more intuitive. The estimation of the differential flow is a two step procedure, where first the reference flow is calculated and used in the second step which is the estimation of the differential flow. The estimate of the differential flow harmonic v'_n is defined as

$$v'_n\{LYZ\} \equiv \langle W_R \cos[n(\Phi - \psi_n^{EP})] \rangle \quad (4.44)$$

[38], where Φ corresponds to the azimuthal angle of the particles of interest used for calculating the differential flow. The event plane ψ_n^{EP} is the same as in the event plane method, although it is implemented differently [45]. Equation (4.44) is in close analogy with equation (4.9) and (4.10), wherefore the LYZ method in this notation is considered as an improved event plane method.

4.2.5.1 Integrated flow

The integrated flow is defined as

$$V_n \equiv \langle Q \cos[n(\psi_n^{EP} - \psi_n^{RP})] \rangle \quad (4.45)$$

where $Q = |\vec{Q}|$ is the flow vector as defined in (4.6). The weights may depend on rapidity and transverse momentum. The integrated flow is denoted by a capital V because the weights may not be dimensionless and in that case nor is the flow.

An estimation of the integrated flow is obtained by the projection of the flow vector onto a fixed arbitrary direction making an angle $n\theta$ with respect to the x -axis. The projection is defined as

$$Q_\theta \equiv Q_x \cos n(\theta) + Q_y \sin(n\theta) = Q \cos[n(\psi_n^{EP} - \theta)] \quad (4.46)$$

This can be inserted into a generating function:

$$G_\theta(r) \equiv \langle e^{irQ_\theta} \rangle \equiv \frac{1}{N} \sum_{j=1}^N e^{ir(Q_\theta)_j} \quad (4.47)$$

In the ideal case multiplicity is so high that event by event variations may be neglected and hence $\psi_n^{EP} \approx \psi_n^{RP}$ which imply that $V_n \approx Q$. Equation (4.47) may be solved to obtain

$$G_\theta(r) = J_0(rV_n) \quad (4.48)$$

where $J_0(x)$ denotes the Bessel function of the first kind of order zero. $G_\theta(r)$ is a function oscillating around zero. Although it is affected by variations in multiplicity, the location of the zeroes remains the same, which makes it advantageous to solve the function $G_\theta(r) = 0$. And hence V_n can be found to be

$$V_n = \frac{j_{01}}{r_\theta} \quad (4.49)$$

where r_θ is the position of first zero of $G_\theta(r)$ and $j_{01} \approx 2.40483$ is the position of the first zero of $J_0(x)$. A plot of $|G_\theta(r)|$ for $\theta = 0$ in the ideal case where there is no variation in multiplicity is shown in figure (4.11).

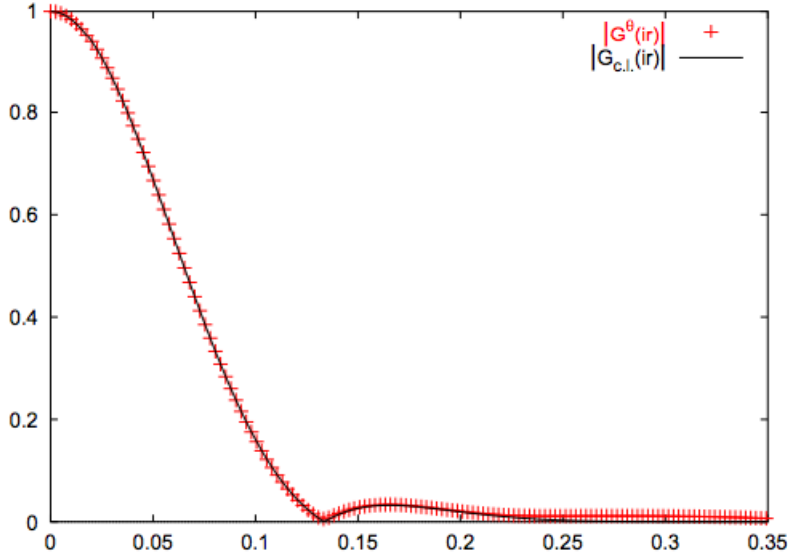


Figure 4.11: $|G_\theta(r)|$ for $\theta = 0$ calculated for 20000 simulated events with $\sqrt{s_{NN}} = 130\text{GeV}$ and each event yielding 300 particles. The solid line represent the expected value.

4.2.5.2 Differential flow

The differential flow can now be estimated. The final result is given in two forms, where one is derived from the other.

$$v'_n\{LYZ\} = V_n \frac{\langle \cos[n(\Phi - \psi_n^{EP})] J_1(r_\theta Q) \rangle}{\langle Q J_1(r_\theta Q) \rangle} \quad (4.50)$$

with $J_1(x) = -\frac{dJ_0(x)}{dx}$. The average in the numerator is over all selected particles in all events and the average in the denominator is over all events. This result is given under the assumption that r_θ is independent of θ which is generally not true since it requires a perfect symmetric acceptance of the detector. The other form is that of equation (4.44) where it is now possible to find the weight from equation (4.50) as

$$W_R = \frac{1}{C} J_1(r_\theta Q) \quad (4.51)$$

With C being a normalization constant given by

$$C = \frac{1}{V_n} \langle Q J_1(r_\theta Q) \rangle = e^{-\frac{j_{01}^2}{4x^2}} J_1(j_{01}) \quad (4.52)$$

Here χ is the resolution parameter given by

$$\chi = \frac{V_n}{\sqrt{\langle Q_x^2 + Q_y^2 \rangle - \langle Q_x \rangle^2 - \langle Q_y \rangle^2 - V_n^2}} \quad (4.53)$$

There is still a dependence on the integrated flow through r_θ in the weight, and hence V_n has to be calculated in order to calculate the weight.

The magnitude of χ is a measurement of the statistical errors. The main limitation of the LYZ arises from statistical errors and hence χ is a strong indicator of whether this method should be applied or not. Comparing the LYZ method to the cumulant method of fourth order, the LYZ method is easier to implement and generally suppresses non-flow effects better than the four-particle cumulant method. However statistical errors increases with decreasing χ and the method is not recommended if $\chi < 0.5$. On the other hand if $\chi > 1$, the statistical errors are even smaller than the cumulant method of fourth order. A rough estimate of χ is that it is given by $\chi \approx v_n \sqrt{M}$. In figure (4.9) and (4.10) the estimated flow from the LYZ method is shown.

Chapter 5

Morphology of High multiplicity Events in Heavy Ion Collisions

As described in the chapter 4 the determination of the flow harmonics can only be determined as an average over many events due to a limitation of the multiplicity. However the high multiplicities obtained in LHC and the improved resolution of the ALICE detector suggests that it might be possible to determine the flow harmonics in an event-by-event analysis. In this chapter it will be demonstrated that the techniques used for the study of cosmic microwave background radiation can be implemented in the study of relativistic heavy ion collisions. Since the techniques are developed for the study of one single event (the Big Bang), it is a natural thought that if the conditions in a heavy ion collision resembles those of the cosmic microwave background, the techniques might lead to an event-by-event analysis. The analogy between the cosmic microwave background and the heavy ion collisions is straightforward, since cosmic microwave background is believed to be remnants of the Big Bang and heavy ion collisions resembles the early conditions of the Big Bang. Indeed heavy ion collisions are used for the determination of the early stages of the Big Bang. The goal of the analysis is to study global structures of the collisions, which eventually will lead to an event-by-event determination of the flow harmonics and the corresponding reaction plane. However the analysis is still in progress and no final conclusion can yet be drawn.

5.1 Motivation

It is not an uncommon thought to consider a high energy heavy ion collision as a little Big Bang. The motivation is that the conditions in the little bangs, where a hot and dense fireball is created followed by a freeze out, is much akin to how the formation of the early universe around the first microseconds is believed to have happened. The commonalities are conspicuous. In both cases, the physical system is viewed at an initial time as exhibiting a phase space distribution with a high degree of symmetry overlaid with distributions of localized fluctuations [15]. The behaviour of the fluctuations are in both cases considered to be fluid like. In the case of the big bang the distribution arises from the Cosmic Microwave Background (CMB) radiation, which is an almost uniform (hence the high degree of symmetry) radiation of blackbody energy from all the sky. This radiation is believed to be the remnants of the very early universe. The CMB do

however exhibit very small variations in the radiation. The root of the mean squared of the variations is $18\mu\text{K}$ [16], which are the localized fluctuations. As for the heavy ion collisions the measured phase space distribution arises from the produced particles in the collision.

The system in both cases is considered to be rapidly expanding. Different particle species, at different times, separate themselves from the common fluid dynamic system. This property is an important tool for identifying the collective dynamics of the fluid. For the Big Bang physics the time of the decoupling of photons can be recalculated, and also it is possible to determine the abundances of primeordial light nuclei. As for the heavy ion physics the temperature for kinetic and hadronic freeze out can be determined, as well as determine the relative abundances of hadronic excited states. As a final example of the commonalities that the study of the fluctuations in CMB has led to a constraintment of the material properties of the universe. Namely that it consists of visible matter, dark matter and dark energy. Similarly it has been experimentally verified that the material properties of the plasma produced in a heavy ion collision, are very close to those of a perfect fluid [17].

However there are also differences, for example the difference in scale and the difference in fundamental forces governing the process. These differences may for a first approach be neglected. Of more importance is the fact that the Big Bang is one event whereas the heavy ion collisions are in principle an infinitely large amount of events.

5.2 CMB analysis

There are three ways of attacking the problem of implementing the CMB-methods in the analysis of RHIC's. This is schematically illustrated in figure (5.1). The three blocks on the top represents three ways of producing an event. Both JYG-Generator and HIJING are generators of simulated events, whereas ALICE-Data refers to data obtained from real collisions in the ALICE-Detector. JYG-Generator is a very simple event generator. HIJING (Heavy Ion Jet INteraction Generator) is the more complicated event generator which reproduces a number of the main features of heavy ion physics in the energy range of RHIC and LHC. However event-production using HIJING takes way longer time than the JYG-Generator. In this chapter the analysis shown is performed on data from HIJING unless otherwise noted, in the following chapters the analysis is performed on data from JYG-Generator. As it appears from the figure the advantage of using simulated events is that the symmetry plane and the amplitude of the flow harmonic is already known. Currently only a very limited amount of the analysis regarding the implementation of CMB-methods has been performed on real data.

The next step is to analyse the data either by GLESP (Gauss Legendre Sky Pixelization) a program package developed for CMB analysis. Or by the use of a modified and simplified version of GLESP. The modified version is written in the C++ programming language in order to be compatible with ROOT, which is a CERN program developed for the study of hadron collisions. This will be elaborated in chapter (6.1).

The last possibility which is analysis with AliROOT is not yet possible. AliROOT is a program build on ROOT. It is a collection of software libraries which takes analysis obtained from ALICE and the ALICE detector effects into account. To make the analysis in AliROOT would require GLESP to be implemented in AliROOT, which has not yet

been done.

All methods of analysis should lead to the final goal of achieving an event-by-event determination of the reaction plane and the amplitude of flow harmonics.

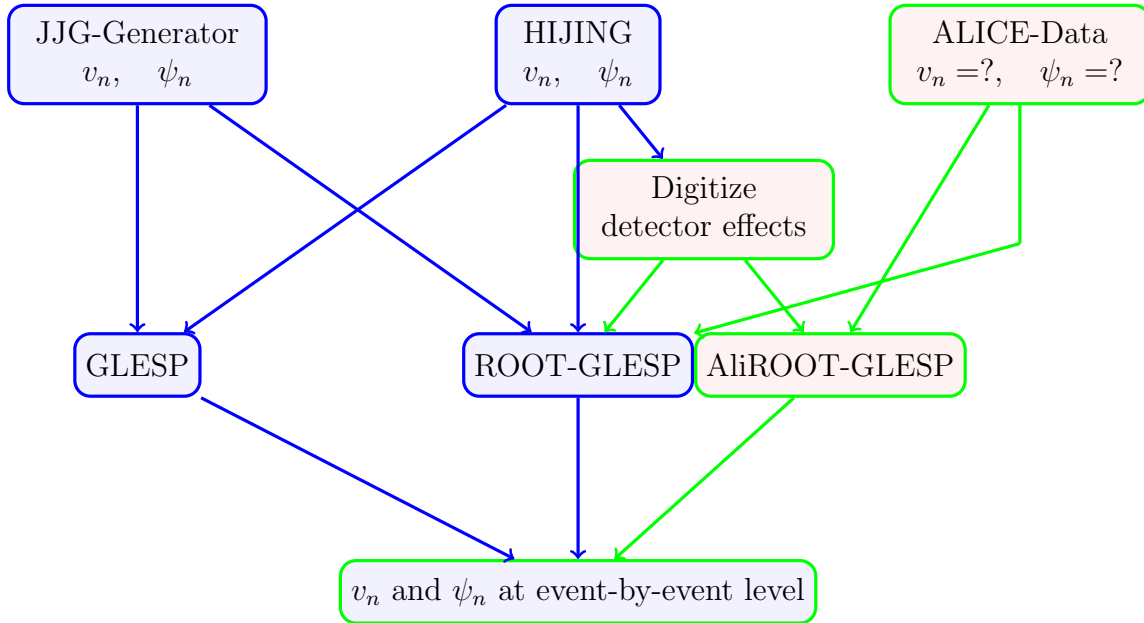


Figure 5.1: Systematic representation of how CMB-methods can be implemented in the RHIC analysis. “JJG-Generator” refers to a simplified event generator originally written by Jens Jørgen Gårdhøje.

5.2.1 The CMB-method

In cosmology, the CMB anisotropy is analysed by means of two-dimensional maps that essentially cover the full sky. A Mollweide projection is typically used for the mapping as shown in figure (5.2) where temperature fluctuations from the mean is visualized over the entire sky. The azimuthal angle runs along the equator and the polar angle runs vertically between the poles.

One way to make this visualization is by using the GLESP (Gauss LEgendre Sky Pixelization) program package. GLESP is a program package written in the C programming language (a FORTRAN version is also available), developed for the purpose to visualise and analyse a signal. The procedure in the analysis is to decompose the signal into spherical harmonics as defined in equation (3.9). From the $a_{l,m}$ -values obtained by equation (3.14) the powerspectrum

$$C(l) = \frac{1}{2l+1} \sum_{m=-l}^l |a_{l,m}|^2 \quad (5.1)$$

is evaluated as an indicator of the magnitude of symmetries with l multipoles.

5.2.2 Mollweide projection of heavy ion events

The Mollweide projection is dependent on the variables θ and ϕ . Such a signal can be obtained from a heavy ion collision. $f(\theta, \phi)$ will be considered as the particle multiplicity

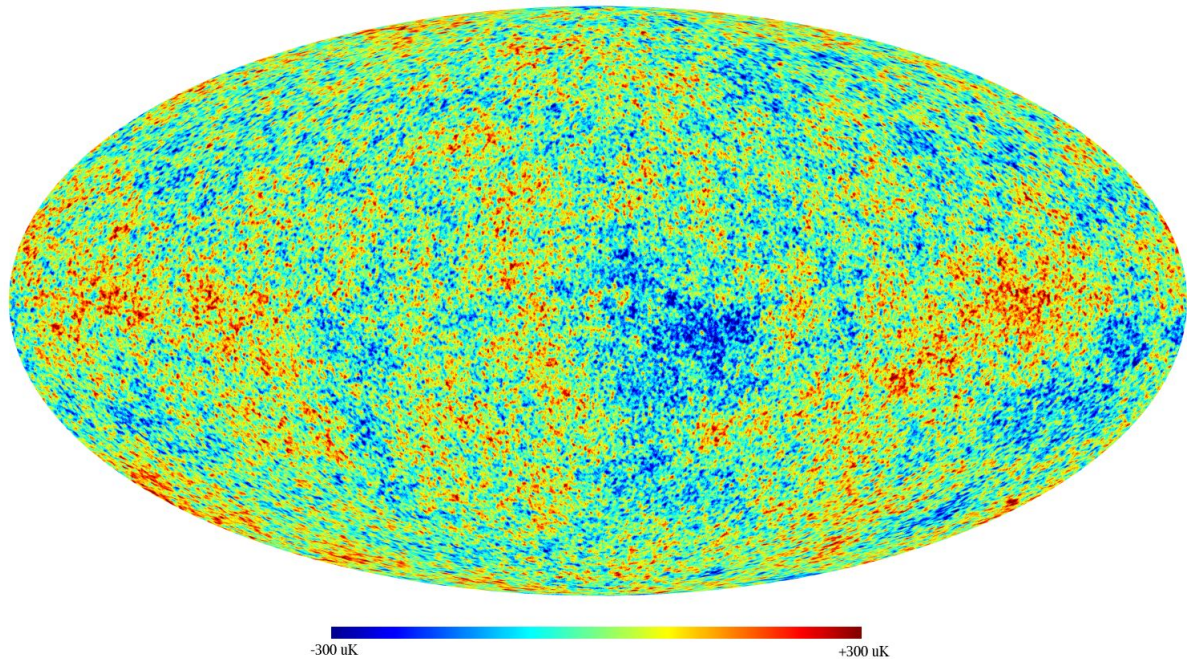


Figure 5.2: The temperature fluctuations from the CMB visualized in a Mollweide projection. In this representation the azimuthal angle ϕ ranging between 0 and 2π runs along the equator and the polar angle θ ranging between 0 and π runs from north to south.

inside a given window positioned at (θ, ϕ) . Particle production in heavy ion collisions in the case of collisions between identical nuclei, is known to exhibit a forward-backward symmetry. This is shown in figure (5.3), where the particle distribution from a Pb-Pb HIJING event is plotted both as a function of η which is the traditional way of plotting particle distributions, and as a function of θ . It is clear that there must be a general θ -dependence on the particle production. In the case of figure (5.3b), this dependence is symmetric around $\frac{\pi}{2}$, but one can easily imagine how the particle distributions from collisions with non-identical nuclei will break the symmetry, but maintain a θ dependency. The first step in the analysis is to remove this θ -dependence, so that underlying fluctuations and azimuthal asymmetries may become more visible. It turns out to be quite simple. The signal $f(\theta, \phi)$ can be plotted in terms of the spherical harmonics by the use of equation (3.13). This is shown in figure (5.4) for a HIJING event producing 17000 particles. However as discussed in section 3.2, there is no ϕ -dependence on the $m = 0$ mode and thus the $m = 0$ removes the signal with no ϕ -dependence. This is illustrated in figure (5.5) for the same event as in figure (5.4). It is seen that the polar caps have been removed and thus the θ -dependent forward-backward symmetry. Obviously this method is not bullet proof since the θ dependency shown in figure (5.3) might also have a dependency on ϕ . However a look at the powerspectrum shown in figure (5.6) convinces that the θ -dependence has indeed been removed. For a perfectly symmetric collision there would have been no odd modes of the powerspectrum, but although small there are odd modes in figure (5.6). The removal of the $m = 0$ mode do only very vaguely affect the odd modes, whereas the even modes become in scale with the odd modes. And thus it is concluded that the θ -dependent symmetry is successfully removed by removing the $m = 0$ part of the signal expressed in terms of spherical harmonics.

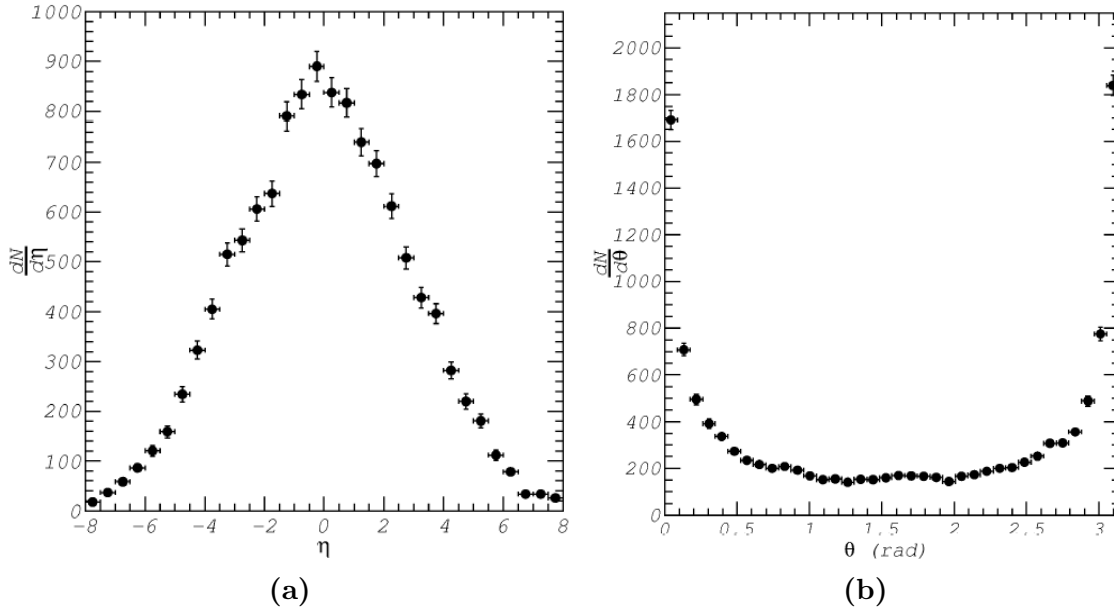


Figure 5.3: Semi peripheral Pb-Pb collision at $\sqrt{s_{NN}} = 2.76$ TeV. with a multiplicity of 12316 particles simulated by HIJING

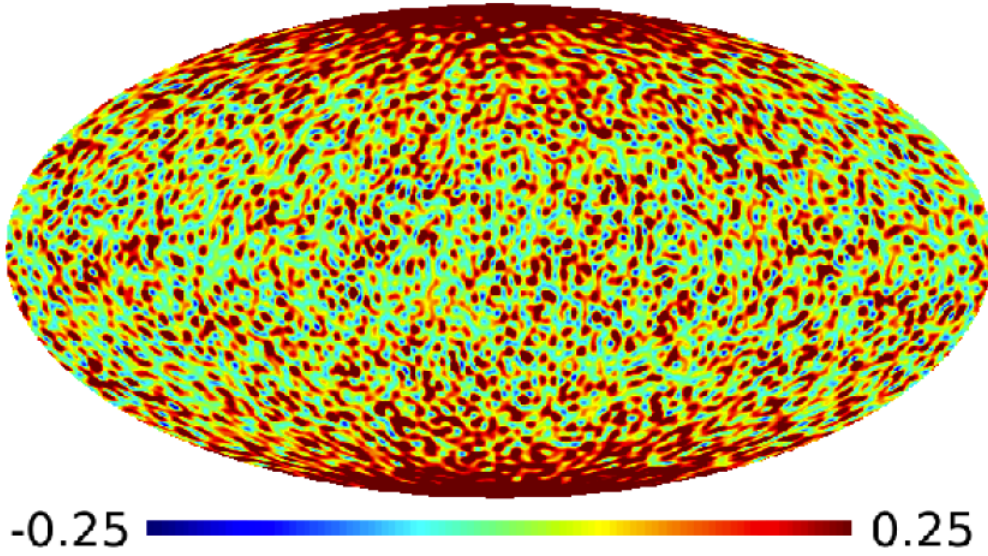


Figure 5.4: HIJING Pb-Pb event with no anisotropic flow producing 17000 particles, visualised in a Mollweide projection where the signal is given in terms of spherical harmonics from equation (3.13). The pixelization is 201×402 , and the color coding shows relative deviations from the mean.

5.2.3 Event-by-event Flow analysis

In order to obtain an estimation for the amplitude of the flow harmonics of order n , the signal will be denoted in a slightly different way as

$$S(\theta, \phi) = f(\theta, \phi) \left[1 + 2 \sum_n v_n \cos[n(\phi - \psi_n)] \right] \quad (5.2)$$

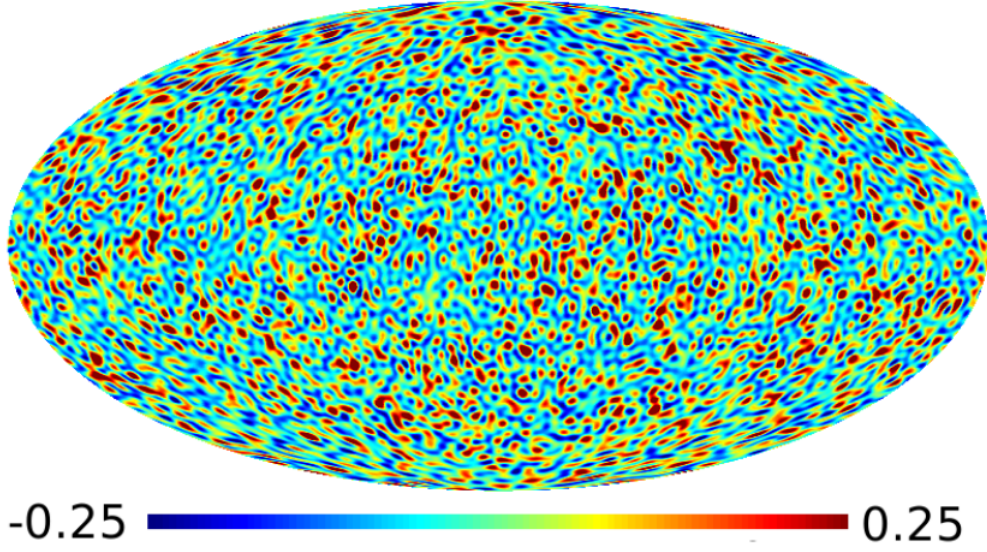


Figure 5.5: Same event as in figure (5.4) but with all $m = 0$ modes removed.

where ψ_n is the symmetry plane and $f(\theta, \phi)$ now denotes the signal without flow and hence is defined as

$$f(\theta, \phi) \equiv \left. \frac{dN^2}{d\theta d\phi} \right|_{v_n=0} \quad (5.3)$$

The weight coefficients of the spherical harmonics associated with $f(\theta, \phi)$ are labelled as $a_{l,m}$, whereas the weight coefficients of the spherical harmonics associated with $S(\theta, \phi)$ are labelled as $b_{l,m}$. Equation (5.2) can be rewritten as

$$S(\theta, \phi) = f(\theta, \phi) + \sum_n v_n [e^{in\psi_n} s^+(\theta, \phi) + e^{-in\psi_n} s^-(\theta, \phi)] \quad (5.4)$$

where

$$s^\pm = f(\theta, \phi) e^{\mp in\phi} \quad (5.5)$$

In this notation $S(\theta, \phi)$ can be decomposed into spherical harmonics as

$$b_{l,m} \approx a_{l,m} + \sum_n v_n (c_{l,m+n} e^{-in\psi_n} + c_{l,m-n} e^{in\psi_n}) \quad (5.6)$$

where

$$c_{l,m\pm n} = a_{l,m} g(l, m \pm n) \quad (5.7)$$

and

$$g(l, m \pm n) = 2\pi \sqrt{\frac{(2l+1)(l-(m \pm n))!}{4\pi(l+(m \pm n))!}} \sqrt{\frac{(2l+1)(l-m)!}{4\pi(l+m)!}} \times \int_{-1}^1 P_l^{m \pm n}(\cos \theta) P_l^m(\cos \theta) d \cos \theta \quad (5.8)$$

is a normalization factor. This type of equation is encountered in the CMB data analysis [46] for cases where the statistical isotropy of the signal is broken by regular modulations. The details of the derivations of equation (5.6) is given in [15].

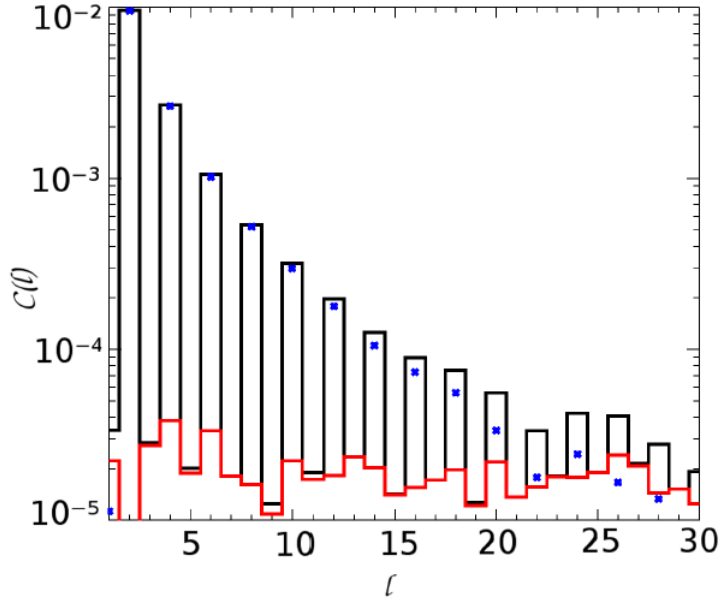


Figure 5.6: Powerspectrum of the HIJING event in figure (5.4). The black line is the total powerspectrum. The blue dots are the $m = 0$ modes only and the red line is the powerspectrum without the $m = 0$ mode.

5.2.3.1 v_n -modulation with $n = \text{even}$

In order to estimate the flow harmonics of even orders, equation (5.6) can be simplified by making a few approximations. This allows for an estimation of both the symmetry plane and the flow amplitude. In the case $m = 0$, equation (5.6) yields

$$b_{l,0} \approx a_{l,0} + \sum_n v_n (c_{l,n} e^{-in\psi_n} + c_{l,-n} e^{in\psi_n}) \quad (5.9)$$

Since the first term is expected to be the dominating one, which is evident from figure (5.6), the approximation can be made that $b_{l,0} \approx a_{l,0}$. The next step is to determine the coefficient $b_{n,n}$.

$$\begin{aligned} b_{n,n} &= a_{n,n} + \sum_{n'=1}^n (v_{n'} b_{n,n+n'} e^{-in'\psi_{n'}} + b_{n,n-n'} e^{in'\psi_{n'}}) \\ &= a_{n,n} + v_1 c_{n,n+1} e^{-i\psi_1} + v_1 c_{n,n-1} e^{i\psi_1} + \dots + v_n c_{n,2n} e^{-in\psi_n} + v_n c_{n,0} e^{in\psi_n} \\ &= a_{n,n} + v_1 c_{n,n-1} e^{i\psi_1} + \dots + v_n c_{n,0} e^{in\psi_n} \\ &\approx a_{n,n} + v_n a_{n,0} g(n) e^{in\psi_n} \\ &\approx a_{n,n} + v_n b_{n,0} g(n) e^{in\psi_n} \end{aligned} \quad (5.10)$$

Where it has been used twice that $|a_{l,0}| \ll |c_{l,n}|$. The step between second and third line is taken because all values of $c_{l,m}$ with $l < |m|$ vanish. In the fourth line the quantity

$g(n)$ has been inferred, it is defined as

$$g(n) = 2\pi \sqrt{\frac{(2n+1)}{4\pi}} \sqrt{\frac{(2n+1)}{4\pi} \frac{1}{(2n)!}} \times \int_{-1}^1 P_n^0(\cos\theta) P_n^n(\cos\theta) d\cos\theta \quad (5.11)$$

Exploiting one of the identities of complex numbers, $b_{n,n}$ can be written in terms of its magnitude as

$$b_{n,n} = |b_{n,n}| e^{i\phi_{n,n}} \quad (5.12)$$

where $\phi_{n,n}$ is the argument of $b_{n,n}$. Making use of equation (5.12) and by assuming the v_n is sufficiently large, such that $|a_{n,n}| \ll |v_n g(n)| |b_{n,0}|$. It is finally possible to obtain an estimate of v_n and the symmetry plane.

$$|v_n| \approx \frac{|b_{n,n}|}{|g(n)| |b_{n,0}|} \quad (5.13)$$

and

$$n\psi = \phi_{n,n} \quad (5.14)$$

$\phi_{n,n}$ is obtained by

$$\phi_{n,n} = \frac{\text{Im}[b_{n,n}]}{\text{Re}[b_{n,n}]} \quad (5.15)$$

5.2.3.2 v_n -modulation with $n = \text{odd}$

In the case of the odd harmonics, the approach has to be altered slightly since there is no dominance of $m = 0$ for odd l in the powerspectrum. The problem is circumvented by consideration of the first harmonics. In this case it is advantageous to work with $b_{2,1}$.

$$b_{2,1} = a_{2,1} + \sum_n v_n (c_{2,1+n}) e^{-in\psi_n} + c_{2,1-n} e^{in\psi_n} \quad (5.16)$$

Making the same approximations as in the even case $b_{2,1}$ can be expressed as

$$b_{2,1} \approx v_1 b_{2,0} g(1) e^{i\psi_1} \quad (5.17)$$

In analogy with the even case the flow harmonic of first order is then given by

$$|v_1| \approx \frac{|b_{2,1}|}{|g(1)| |b_{2,0}|} \quad (5.18)$$

With the symmetry plane

$$\psi_1 = \phi_{2,1} \quad (5.19)$$

From these calculations it is obvious that an estimation of any odd order flow harmonics can be obtained by

$$|v_n| \approx \frac{|b_{n+1,n}|}{|g(n+1)| |b_{n+1,0}|} \quad (5.20)$$

And the symmetry plane

$$n\psi_n = \phi_{n+1,n} \quad (5.21)$$

5.2.3.3 Analysis on elliptic flow

These equations have been tested in [15] for elliptic flow. For the analysis of symmetry plane a set of 202 HIJING events with $v_2 = 0.07$ were produced, and $\phi_{2,2}$ was plotted against ψ_2^{RP} . The results which are in almost perfect agreement with equation (5.14) are shown in figure (5.7a). The histogram in the right corner shows the distribution of $\psi_2^{RP} - \frac{\phi_{2,2}}{2}$.

For the estimation of the flow harmonics the JJG-Generator, which will be described in chapter 7, was used. The reason for the choice of the JJG-Generator was that each estimation was calculated as the mean of 10^5 events. The result is shown in figure (5.7b), with the error bars being one standard deviation. The slope on the curve is 1.11.

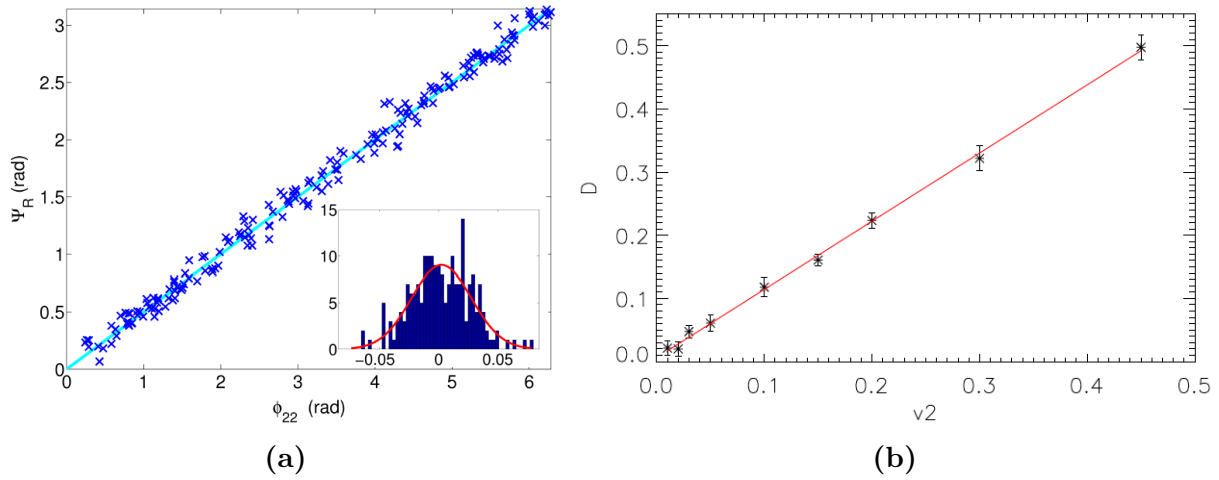


Figure 5.7: The results from analysis with GLESP confirming equation (5.13) and (5.14). (5.7a) shows the determination of the symmetry plane from 202 HIJING events with $v_2 = 0.07$ and the figure in the right corner is a histogram of the distribution $\psi_2^{RP} - \phi_{2,2}$. (5.7b) shows the estimation of v_2 . Each point represents the mean of 10^5 events. The error bars indicate one standard deviation.

Chapter 6

Implementation of GLESP into the ROOT framework

The method presented in chapter 5 was based on analysis with the GLESP package performed on events from HIJING. But until now only a very limited analysis has been performed and only on events containing elliptic flow only [15]. Unfortunately, if the method is to become a tool in the data analysis at LHC, the GLESP package is not suitable since it would require too much adaptation from outsiders. The CERN community uses the object-oriented program ROOT for data analysis. This chapter will be concerned with the task of rewriting the fractions of GLESP which is needed for the flow analysis into a version compatible with ROOT.

6.1 From GLESP to ROOT

ROOT is a program based on the programming language C++, but with a lot of additional features. One feature which will be exploited the most in this thesis is the ability to draw histograms and graphs. Although ROOT can be operated directly, the common way is to write subprograms which will be interpreted by ROOT. Thus the task of making GLESP compatible with ROOT, is the task of writing a program that can be interpreted by ROOT, which generates the same information as GLESP. The task is simplified by the fact that GLESP is written in C. C++ is based on C and is almost completely compatible with C.

6.1.1 The GLESP package

GLESP is a pixelization scheme developed for the CMB maps. The pixelization of the map is based on the Gauss-Legendre quadrature. This mapping allows for precise and efficient calculation of the $a_{l,m}$ coefficients in equation (3.14) [47]. In the following when referring to GLESP is not meant the pixelization scheme but the program package developed for this method of sky pixelization and calculation of $a_{l,m}$ coefficients.

GLESP contains 11 different operations each of which have a number of variations. Only five of these are of interest for the flow analysis, and only two of these have been rewritten into a form compatible with ROOT. The five operations are:

mappat: The purpose of *mappat* is to create a map as a representation for a given signal. The number of pixels can be varied as well as the way arranging the pixels. *mappat* produces an output file containing information about the signal and the pixelization of the map, however the map is not visualised with *mappat*.

f2fig: The purpose of *f2fig* is to visualize the information contained in the output file from *mappat*.

cl2map: The purpose of *cl2map* is to calculate the $a_{l,m}$ values from the information contained in the output file of *mappat*. *cl2alm* produces two output files, one containing the powerspectrum evaluated from the $a_{l,m}$ values, and the other containing information which can be translated to the $a_{l,m}$ values.

alm2dl: *alm2dl* creates an output file listing the $a_{l,m}$ values calculated in *cl2map*.

mapcut: *mapcut* can make cuts in the output file from *mappat* and thus limit the range of θ and ϕ . If the *mapcut* command is used *f2fig* and *cl2map* takes the output file from *mapcut* as input file.

These operations are all included in the ROOT version of GLESP in the following referred to as GiRo (Glesp In ROot). However only *mappat* and *cl2map* are directly rewritten from the source files, whereas it was somewhat simpler to implement the other operations by exploiting some of the features in ROOT.

6.1.2 Rewriting of mappat

The *mappat* operation is initiated in a bash shell with the command

```
./mappat hits.txt -A -nx 201 -np 402 -o map.fts
```

where “hits.txt” is the input file, it takes the form as shown in figure (6.1) where each line represent a particle and the first three columns is the position in η, θ and ϕ respectively.

```
BEGIN EVENT 1
-2.29084 168.445 173.678 1 1.8 3.6
-0.332037 108.684 151.411 1 1.8 3.6
-0.754721 129.64 88.853 1 1.8 3.6
1.92541 16.5924 117.101 1 1.8 3.6
0.457264 64.6687 240.802 1 1.8 3.6
2.02551 15.0309 66.819 1 1.8 3.6
-3.82089 177.49 97.1817 1 1.8 3.6
1.13775 35.5453 114.476 1 1.8 3.6
-0.9926 139.329 63.433 1 1.8 3.6
-1.46603 154.003 15.543 1 1.8 3.6
-0.154269 98.8041 103.827 1 1.8 3.6
```

Figure 6.1: Sample of an input file for the *mappat* command. Each line represent the position of a particle, where the first column is the position in η , the second column is the position in θ and the third column is the position in ϕ . The last three columns are unimportant

The flag “A” specifies the type of pixelization (how the pixels are arranged) for the map. In GiRo the flag is taken to be “A” for the pixelization type and it will be labelled as “A-pixelization”. However this may not be the best choice of pixelization type, as will become clear in the analysis part of the thesis, because the normalization factor $g(n)$ in equation (5.13) and (5.20) does not normalize the estimated flow correctly. This problem may however be solved by choosing a different kind of pixelization.

The flags “nx” and “np” specifies the amount of pixels in the θ and ϕ direction respectively and “o” specifies the name of the output file.

6.1.2.1 Pixelization

In the ϕ -direction each pixel is of equal size. But in the θ -direction the pixel size is calculated by use of the Gauss-Legendre quadrature integral approximation, which as the name imply is an approximation to an integral of a function.

$$\int_{-1}^1 f(x)dx = \sum_{i=1}^{\infty} w_i f(x_i) \approx \sum_{i=1}^n w_i f(x_i) \quad (6.1)$$

where the w_i are weights. It turns out that the values x_i at which the function $f(x)$ is evaluated are simply the roots of the Legendre Polynomial of n 'th order given by

$$P_n(x) = \frac{1}{2^n n!} \frac{d^n}{dx^n} ((x^2 - 1)^n) \quad (6.2)$$

And the weights can be calculated as

$$w_i = -\frac{2}{(1 - x_i^2)[P'_n(x_i)]^2} \quad (6.3)$$

The values of x_i and w_i are symmetric around zero. $x_i = \cos \theta_i$ are used as the center of the i 'th pixel in the θ direction, and the pixel will be associated with the weight w_i . The Legendre Polynomials for $n = 1, \dots, 5$ are shown in figure (6.2). For the evaluation of x_i and w_i GLESP follows a routine which is referred to as “gauleg” [48]. The C++ code of the routine can be seen in appendix B. Figure (6.3) and (6.4) shows the pixel position and the weights with $n = 62$ evaluated by the gauleg routine.

Particles from an event can be distributed according to their position in θ and ϕ on a map with the above described pixelization. In GiRo a two dimensional histogram will be used for this purpose (GLESP uses a one dimensional array of length $N_\theta \times N_\phi$). Using a 2D histogram makes it straightforward to visualise the signal, simply by drawing the histogram. In the following when histograms in ROOT are mentioned each pixel will be referred to as a bin, and the pixelization will be referred to as the binning. The C++ code for the creation of a histogram with the gauleg binning is given in appendix B. The maps showing the particle distribution from a simulated event as produced from GLESP and Giro respectively are shown in figure (6.5).

6.1.3 Evaluation of spherical harmonics coefficients

The initial step in the evaluation of the $a_{l,m}$ coefficients is to calculate the Fourier expansion of the signal in ϕ for each θ -bin (thus making N_θ Fourier expansions for arrays of size

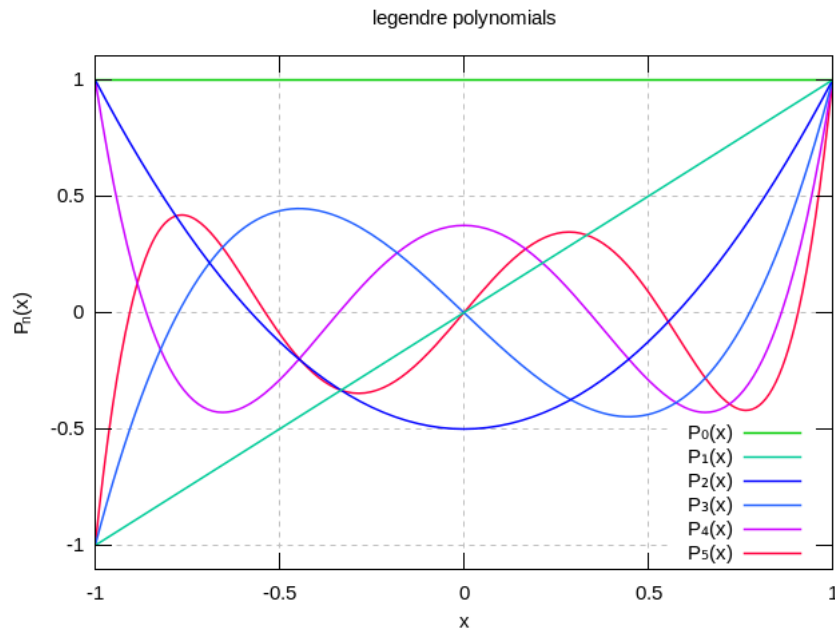


Figure 6.2: The first five orders of the Legendre Polynomials. The intersections with the x -axis is symmetric around zero but wider separated close to zero than at the end points.

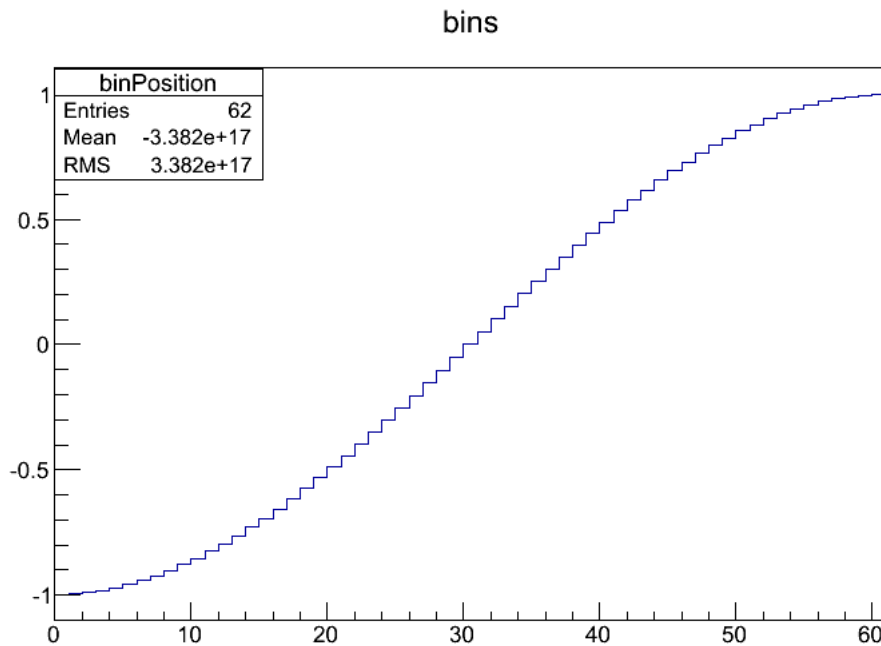


Figure 6.3: The values of x_i calculated for $n = 62$. The slope increases around zero indicating a larger separation of the bins in the central region of the histograms for which the values of x_i are used.

N_ϕ). GLESP makes use of a FFT provided by a C subroutine known as the Fastest Fourier Transform In the West (FFTW). By inserting the Fourier coefficients at the position of $f(\theta, \phi)$ in equation (3.14), the dependence on ϕ is eliminated. At this point GLESP can

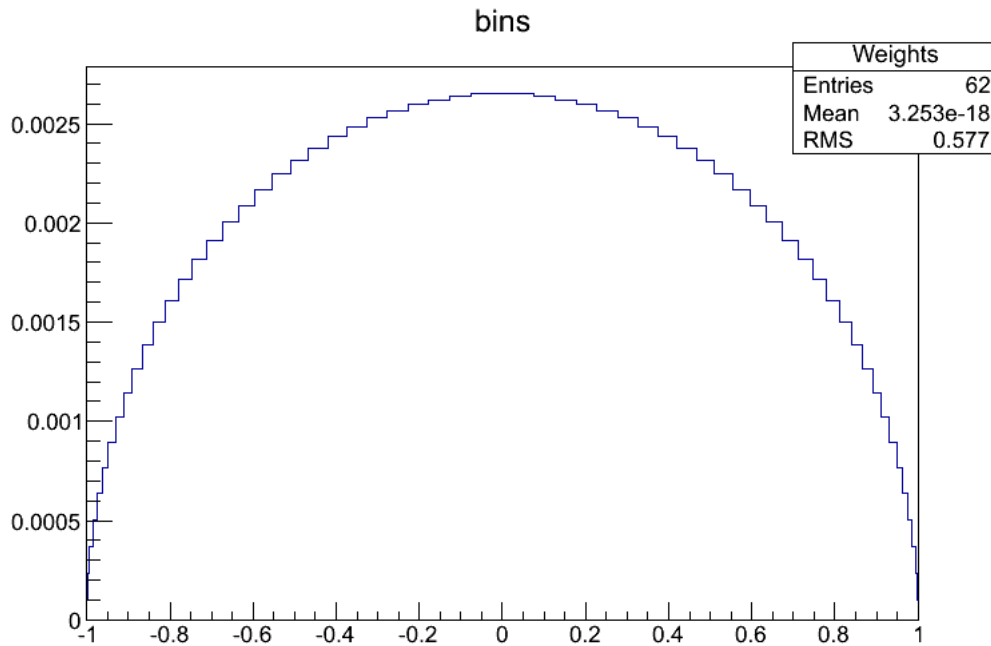


Figure 6.4: The values of w_i calculated for $n = 62$.

exploit the fact that the pixelization is based on the Gauss-Legendre quadrature for a fast evaluation of the spherical harmonics coefficients [47].

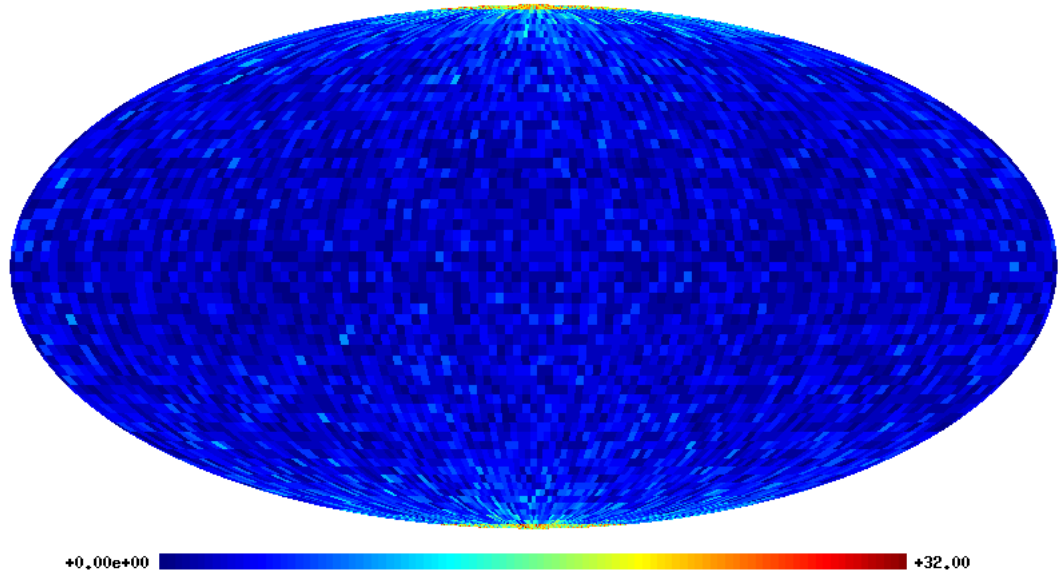
6.1.3.1 The GiRo code

Starting from the input file in figure (6.1), GLESP needs two operations in order to calculate the $a_{l,m}$ coefficients (*mappat* and *cl2map*). In ROOT the mapping and the evaluation of the $a_{l,m}$ -coefficients is gathered into one operation, such that the mapping cannot be done without calculating the $a_{l,m}$ coefficients¹. This has some advantages and disadvantage. The advantage is the obvious one, that only one command is needed in order to execute two (GLESP) operations. The disadvantages are twofold:

1. As mentioned above the pixelization may not be the best suited pixelization, and hence it would be advantageous if GiRo was written in a way where it was easy to implement and switch among different kinds of pixelizations.
2. Some calculations may only require either the mapping or $a_{l,m}$ coefficients. Especially the case, where only $a_{l,m}$ coefficients are needed from an already existing map, is laborious. In this case the data will have to be retrieved from the map and written into a text file of the form in figure (6.1) in order to recalculate the map and obtain the $a_{l,m}$ coefficients.

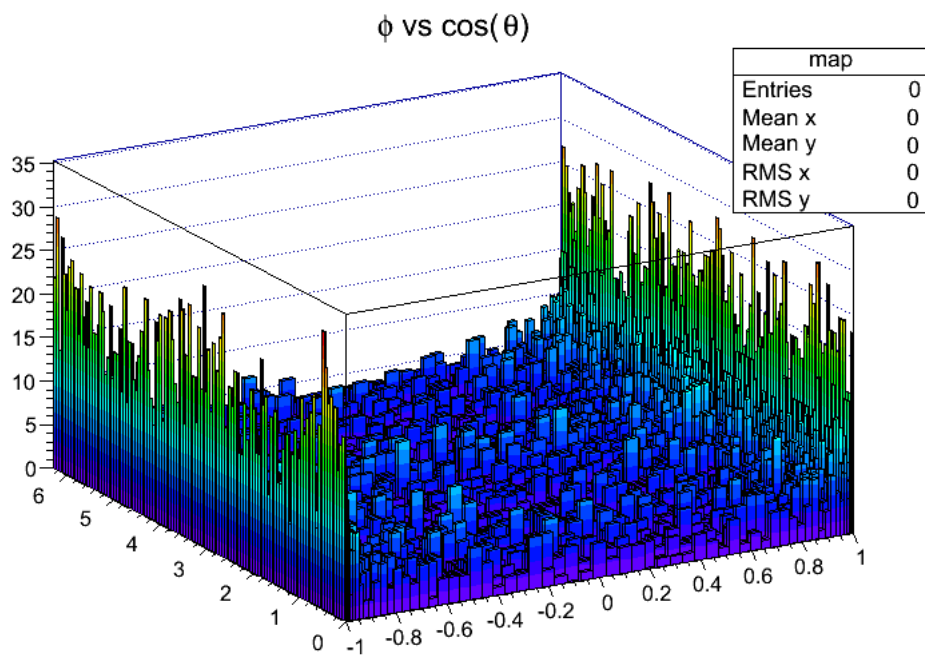
ROOT also make use of FFTW in order perform the Fourier transform of the map, and hence this step is exactly the same as in GLESP. In GiRo is implemented the possibility

¹This is not entirely true, because GiRo is a product of several functions. One can write a program which utilizes only some of these functions in order to e.g. only do the mapping.



//Users/bastianpoulsen/Documents/KU/Speciale/Programmer/nappat/jjg/MapComparison/v1r0_v2r1_v3r0_v4r0_v5r0_v6r0_v7r0

(a) GLESP



(b) GiRo

Figure 6.5: Map of a simulated collision with 30000 particles and the pixelization/binning 62×122

to reduce the range of θ upon which the Fourier transform is performed. This makes the *cutmap* operation in GLESP superfluous.

In the final evaluation of the $a_{l,m}$ coefficients through equation (3.14) ROOT has its own command for the calculation of $Y_l^m(\theta, \phi)$. This makes the coding very simple. Unfortunately it does not exploit the Gauss-Legendre quadrature binning of the map. Never the less this command has been used, and indeed GiRo is much slower than GLESP. The GiRo commands for the evaluations of the Fourier transform and $a_{l,m}$ coefficients are shown in appendix B.

6.1.4 End product of GiRo

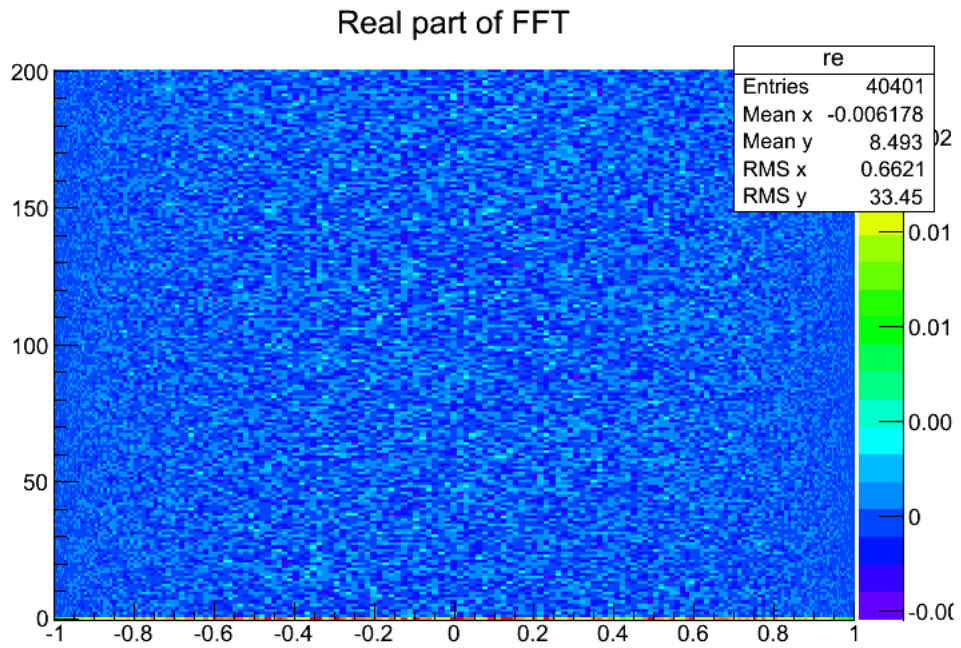
All results obtained by GiRo are stored in histograms and saved in a single root-file. After compiling the GiRo program, the information stored in the root-file is:

1. The positions of each bin in the $\cos \theta$ -direction and the corresponding weights as shown in figure (6.3) and (6.4).
2. A 2D histogram containing the particle distribution of an event as shown in figure (6.5b).
3. The coefficients of the Fourier expansion in ϕ separated into a real and an imaginary part, this is shown in figure (6.6).
4. The $a_{l,m}$ -coefficients separated into a real and an an imaginary part, this is shown in figure (6.7).
5. A powerspectrum calculated on the basis of the $a_{l,m}$ coefficients, this is shown in figure (6.8).

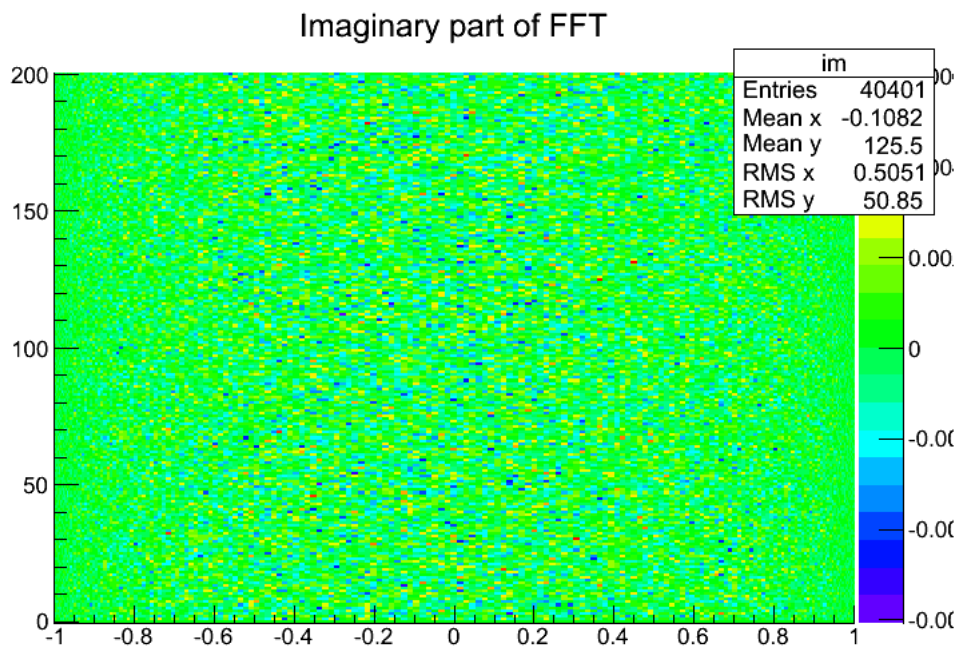
The ability to make cuts on the maps is not as extensive in GiRo as in GLESP. GiRo has the ability to select a region in θ which is not to be removed. GLESP can make cuts both in θ and ϕ and decide, whether the selected region is to be removed and the rest of the map is to be kept or conversely, if the selected region is to be kept and the rest of the map is to be removed. This means that unlike GLESP, GiRo only allows for an analysis on a continuous interval. One additional limitation is that GiRo only performs the cut in the subsequent calculations (at the Fourier transformation) and not on the map itself.

Two differences between GLESP and GiRo ought to be mentioned. The choice of storing all data in histograms by the use of root files is different from GLESP which does only provide information in ascii-files (text-strings). In the ROOT framework it is convenient to work with histograms since ROOT provides a lot of useful options for the histogram. The second difference is that GiRo stores the Fourier coefficients.

The output from GiRo is in almost perfect agreement with GLESP. The fractional deviations between GLESP and GiRo are in the order of 10^{-9} . This is illustrated in the figures (6.9)-(6.12).

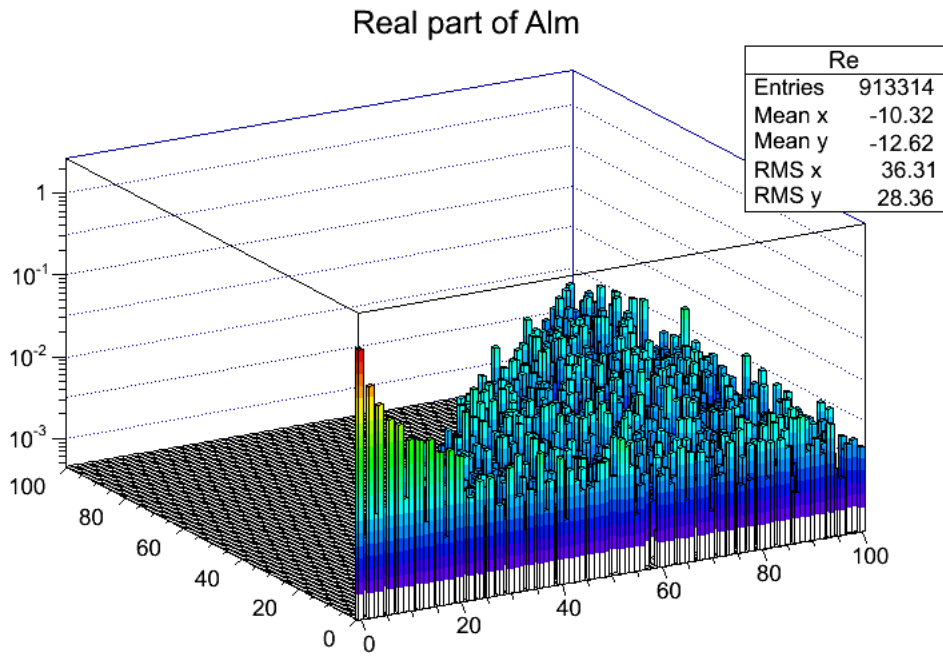


(a) Real

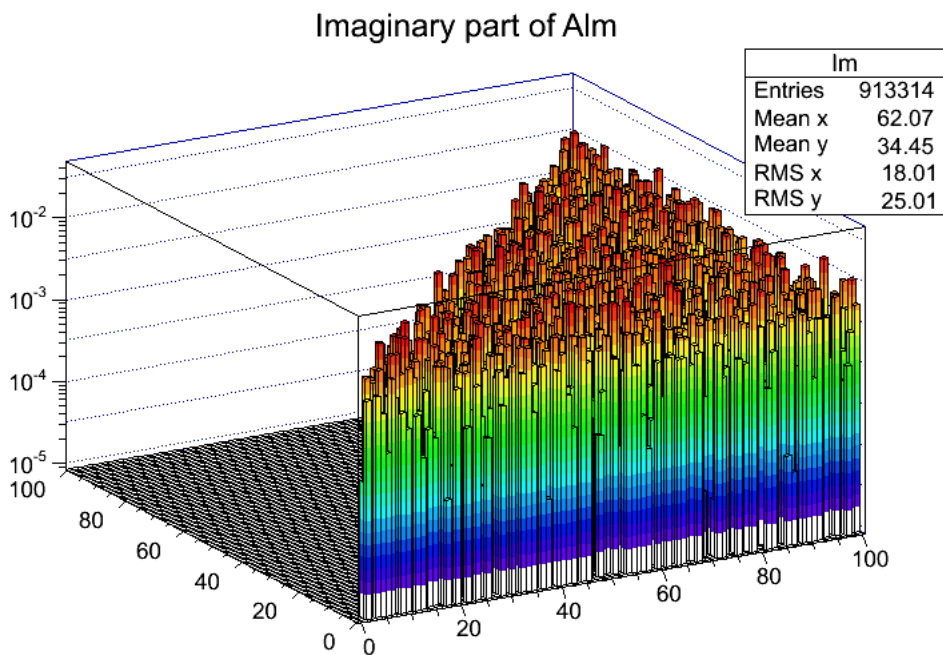


(b) Imaginary

Figure 6.6: The real and imaginary parts of the Fourier coefficients calculated by GiRo with a 201×402 binning, plotted in 2D histograms.



(a) Real



(b) Imaginary

Figure 6.7: The real and imaginary parts of the coefficients of the spherical harmonics calculated by GiRo with a 201×402 binning, plotted in 2D histograms.

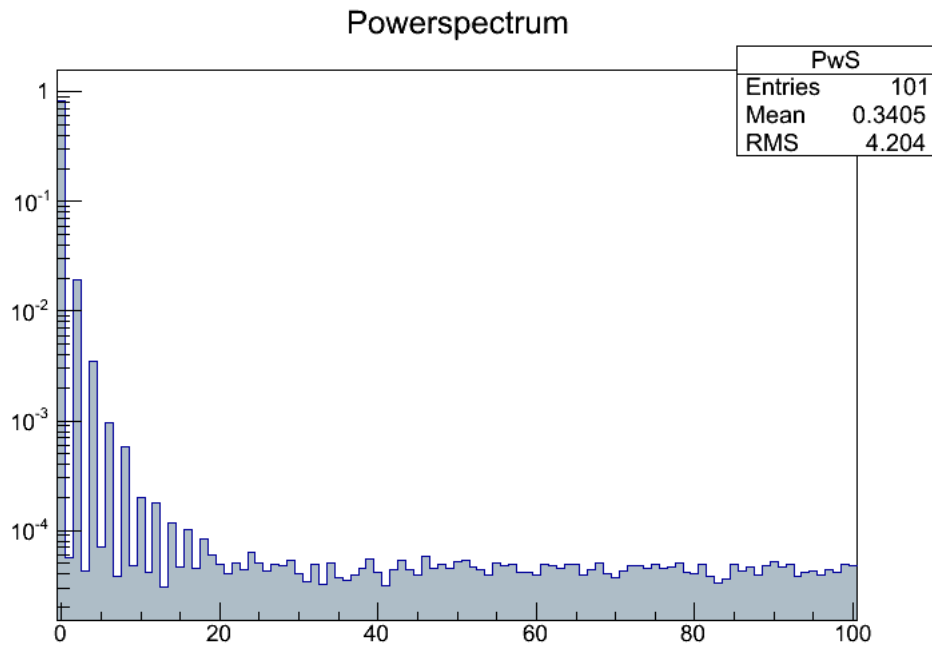


Figure 6.8: Powerspectrum with $l = 100$ calculated on the basis of the $a_{l,m}$ coefficients in figure (3.3)

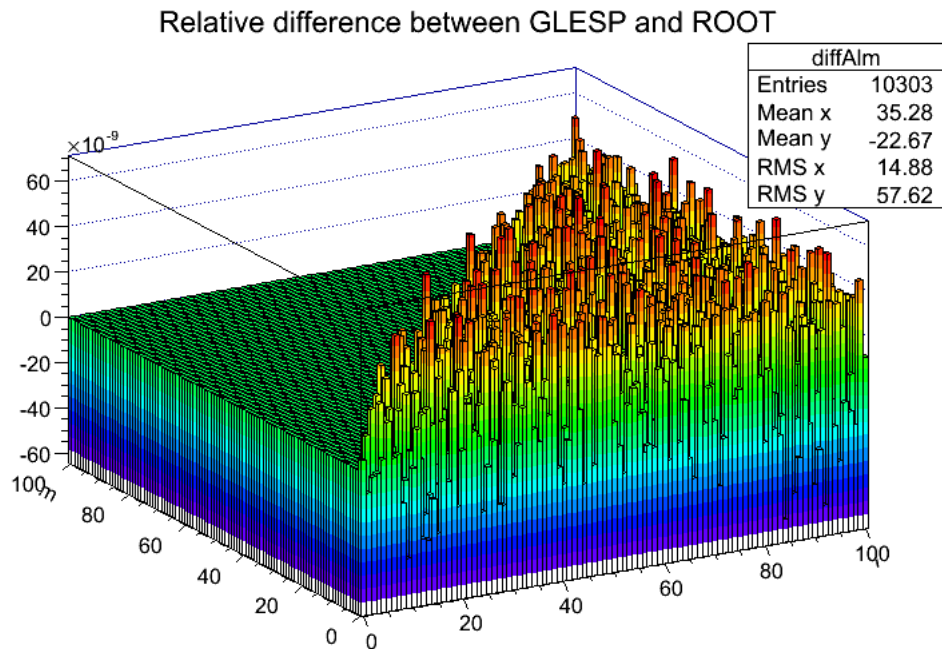


Figure 6.9: Relative deviations in $\text{Re}[a_{l,m}]$ between GLESP and GiRo. Calculated as $\frac{\text{GLESP}}{\text{GiRo}} - 1$.

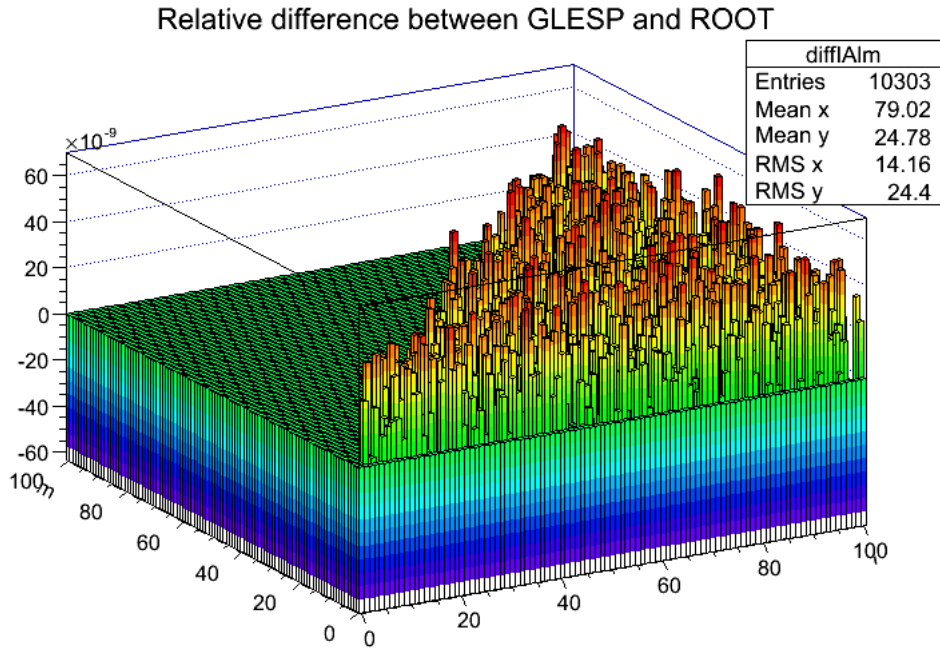


Figure 6.10: Relative deviations in $\text{Im}[a_{l,m}]$ between GLESP and GiRo. Calculated as $\frac{\text{GLESP}}{\text{GiRo}} - 1$.

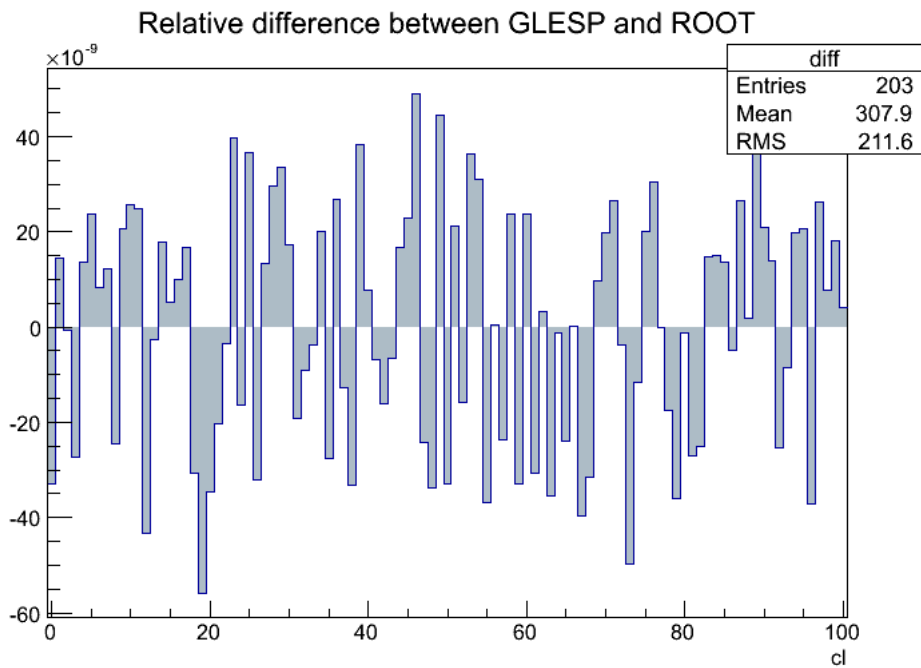
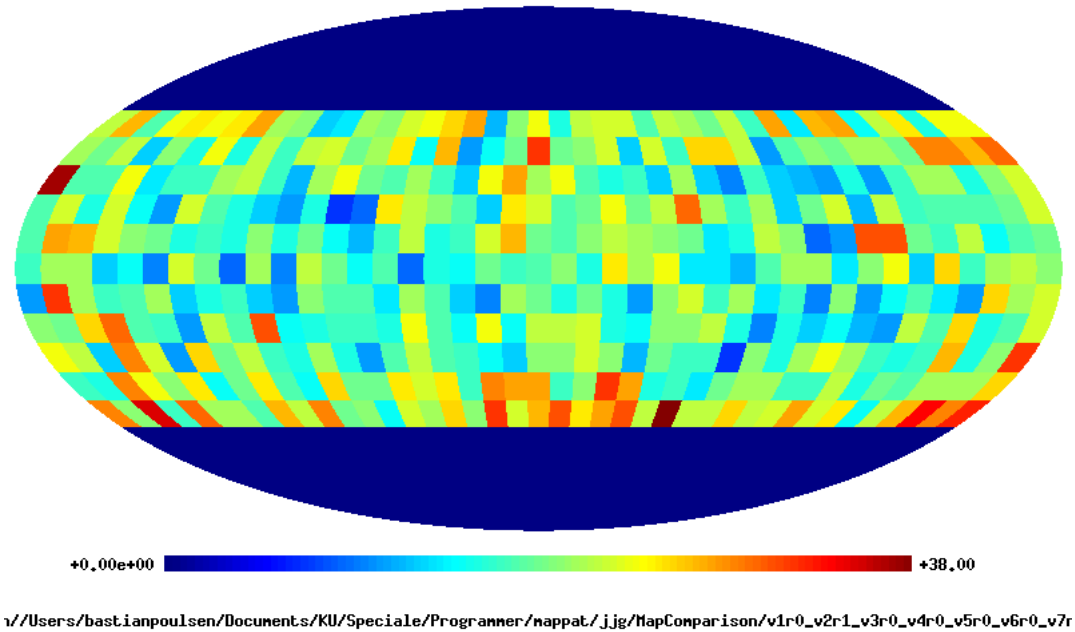
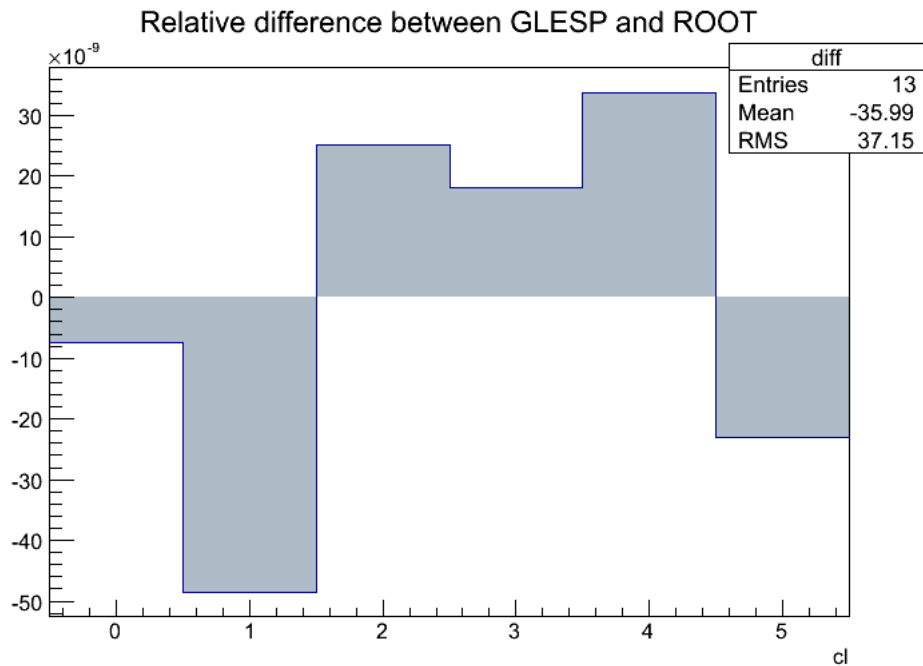


Figure 6.11: Relative deviations in powerspectrum between GLESP and GiRo. Calculated as $\frac{\text{GLESP}}{\text{GiRo}} - 1$.



(a) Map from GLESP



(b) Powerspectrum

Figure 6.12: Relative deviations in powerspectrum between GLESP and GiRo where a cut has been performed. Calculated as $\frac{\text{GLESP}}{\text{GiRo}} - 1$. Panel 6.12a shows the map after the cut operations have been performed (this map can not be produced in GiRo). Panel 6.12b) shows the relative deviations in the powerspectrum. The binning is 21×42 . The reason for this low resolution is that when using the *cutmap* operation with θ as lower limit and $\pi - \theta$ as upper limit, the map produced in GLESP was not symmetric around equator. Hence in order to have the same limits in GiRo and GLESP, the input limits in GLESP were guessed by looking at the map.

Chapter 7

The event generator

The HIJING event generator is too slow for the analysis performed in this thesis and a simpler but faster event generator was written adapted for the task of simulating fast events with a θ -dependence in the particle distribution. This chapter is concerned with the construction of the generator.

7.1 The JJG-Generator

The JJG-Generator takes its name from the author of the original program Jens Jørgen Gaardhøje. It is a program which generates a given number of particles where each particle is defined by its coordinates (θ, ϕ) . The particles are saved in an output file of the form of figure (6.1). The only information yielded by the event generator about the individual particles, is their position (θ, ϕ) . However it is possible to impose some global features on the event. The features are dijets, bubbles and flow up to eighth order. The ability to impose jets and bubbles are remnants of the early analysis, when it was still not known what direction the analysis with CMB-methods would take, and obviously they are not needed in this analysis.

7.1.1 Particle distribution

The particles are generated by the use of a random number generator. Two random numbers are needed for each particle namely a value of θ generated in the range $\theta \in [0; \pi]$ and a value of ϕ generated in the range $\phi \in [0; 2\pi]$. Both θ and ϕ are generated with a random number generator with the seed set to be zero, meaning that the generator is time dependent, and as long as the time interval between two events is larger than 100 ns. the events are not identical. In ϕ the particles are uniformly distributed in the range. The particles generated in θ are initially not generated as a distribution in θ , but as a distribution in η . In order to take the forward-backward symmetry into account the distribution is generated as a Gaussian distribution with a width of 2.4 and a mean at 0. Although not identical this is a signal comparable to that shown in figure (5.3a). From η a value of θ is calculated through equation (1.3). The particle distribution in θ and η from the JJG-Generator are shown in figure (7.1), and distribution taking both the position in θ and ϕ into account is shown in figure (7.2).

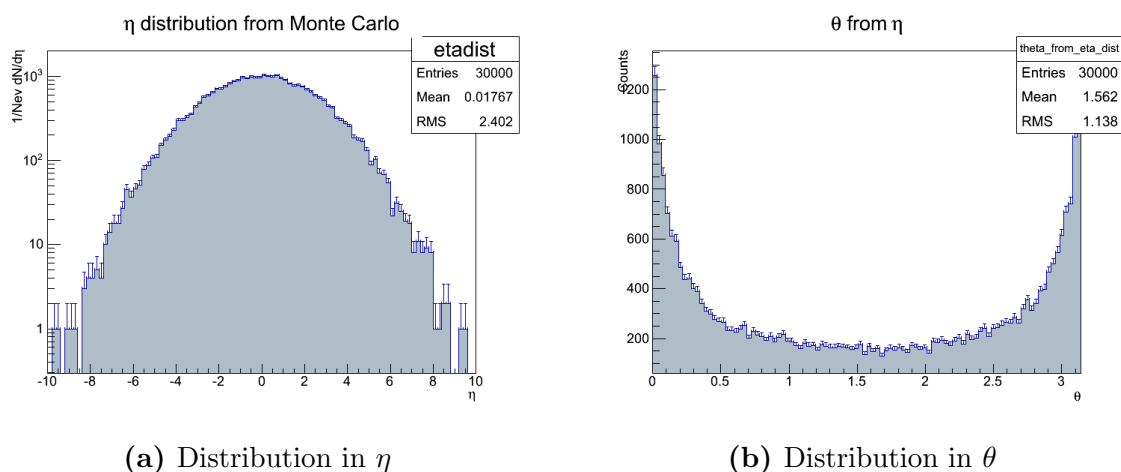


Figure 7.1: The particle distribution in η and θ from the JJG-Generator, with 30000 particles and a bin width of 0.2 and $\frac{\pi}{100}$ respectively.

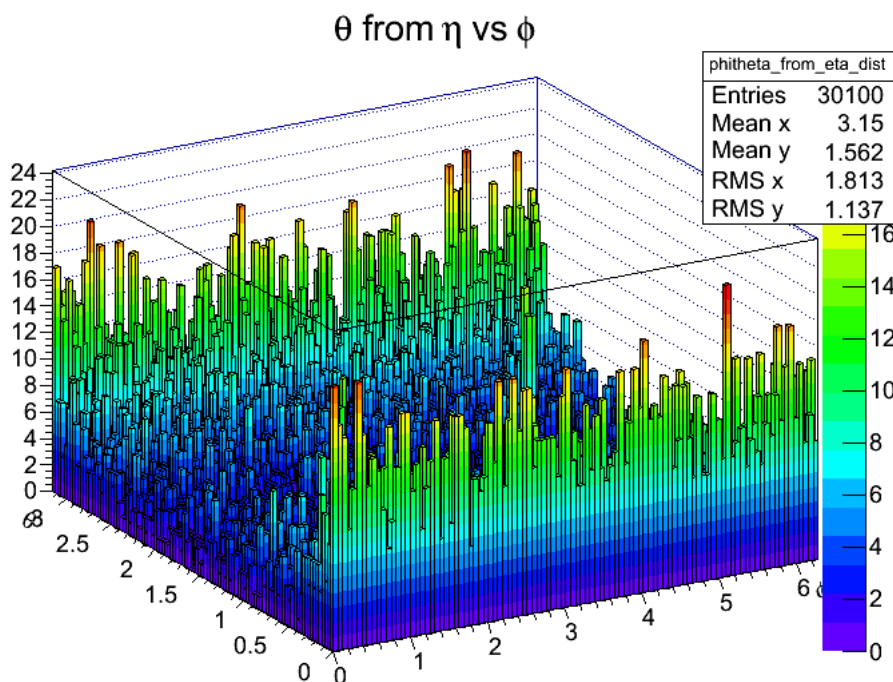


Figure 7.2: The particle distribution with respect to θ and ϕ from the JJG-Generator, with 30000 particles and a bin width of $\frac{\pi}{100}$ and $\frac{2\pi}{100}$ respectively.

7.1.2 Flow and cuts

The JJG-Generator has in its present form the ability to impose flow of up to eighth order, where both the magnitude of the flow harmonics v_n and the reaction plane ψ_n can be varied. The flow is imposed by the use of the sum in equation (4.4) and hence $f(\phi)$ is

given by.

$$f(\phi) = \sum_{n=1}^8 \cos[n(\phi - \psi_n)] \quad (7.1)$$

This way of imposing the flow, maintain the anisotropic properties, but with a different normalization than that of equation (4.4). It is dictated by the fact that there is almost a 1:1 correspondence between the input flow and the estimated flow in the analysis when using the A-pixelization. However it may lead to confusion since the results in chapter 5 are obtained by following equation (4.4), and hence estimations of v_n from JJG-Generator events must be scaled with a factor of two in order to be comparable to chapter 5. A warning is issued at this point, that in all of subsequent analysis, flow from the JJG-Generator is imposed by (7.1), and the flow estimations has not been scaled by the factor of two. The ϕ distribution with imposed flow for various orders is visualized in figure (7.3). Figure (7.3c) has a change in the reaction plane and figure (7.3e) has two order of flow of uneven magnitude.

The event multiplicity, the value of each individual v_n and the value of each individual ψ_n are all input parameters, which can be varied without opening the source file of the JJG-Generator. This makes it easy to make a systematic analysis of the effects of these parameters.

It is also possible to make cuts in the η -distribution just as in GiRo, simply by omitting particle production in a certain range. Since most of the subdetector systems in ALICE cover the entire range in ϕ , it has currently not been necessary to implement a cut on ϕ , although it can easily be done.

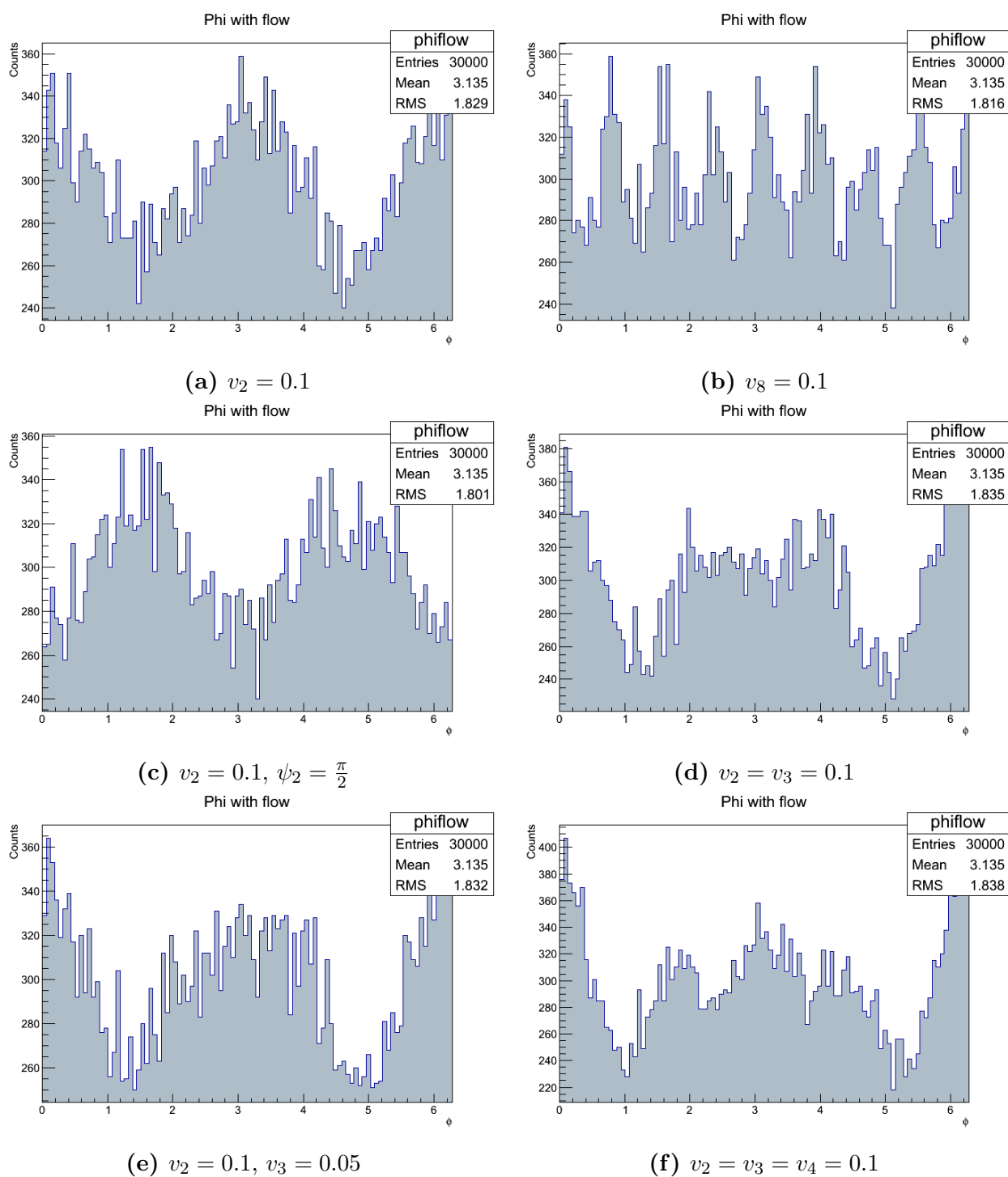


Figure 7.3: ϕ -distribution from events with various flow harmonics from JJG-Gen, the reaction plane is zero if not otherwise noted.

Chapter 8

Analysis of simulated events with a single flow harmonic

Previous chapters have been concerned partly with the theoretical basis and partly with a description of the analysis tools. This and the following chapter are concerned with the analysis of simulated events. The goal is to test and confirm as many aspects as possible of equation (5.13), (5.14), (5.20) and (5.21). In this chapter only simplified events with only one flow harmonic will be considered. The chapter is divided into three sections, describing the analysis of elliptic flow, the analysis of even flow harmonics and the analysis of odd flow harmonics. Once again the warning from chapter 7 must be sounded, that the analysis is performed on events where flow is imposed by the use of equation (7.1) and not equation (4.4), thus making the flow coefficients v_n only half the magnitude of the conventional flow coefficients.

8.1 Settings

The principle in the analysis is generally independent of what aspects of equation (5.13) or (5.20) are to be analysed. A series of 1000 events with equal input parameters will be produced as a statistical background. And/or a series of 50 events will be produced where the input parameters may be altered. Unless otherwise stated all calculations are based on events with a multiplicity of 30000 particles. All analysis has been performed by use of the A-pixelization. By coincidence the approximation $v_2 \approx \frac{|b_{2,2}|}{|b_{2,0}|}$ is almost valid when using the A-pixelization. It was only discovered late, in the process that the factor $g(n)$ had to be applied, and even later it was discovered that the application of this factor needed another pixelization. Consequently the analysis is dominantly performed without the use of $g(n)$ factor and most results will thus be presented without the application of this factor. For this reason the validity of the results obtained in [15] summarized in subsection 5.2.3.3 can not be confirmed in this thesis.

8.2 Analysis of elliptic flow

An obvious place to start the analysis would be by considering events containing only elliptic flow. Partly because it is the dominant flow harmonic in real events and partly

because it is not influenced by other flow harmonics and hence the approximation in (5.13) may be closer to an actual equal sign than for higher order harmonics. The first approach is to generate a series of 50 events each with a specific amplitude of v_2 and check whether the estimated flow will yield the same result. Two event types are chosen for the first analysis, one type with $v_2 = 0.1$ and one type with $v_2 = 0.5$. The result is shown in figure (8.1).

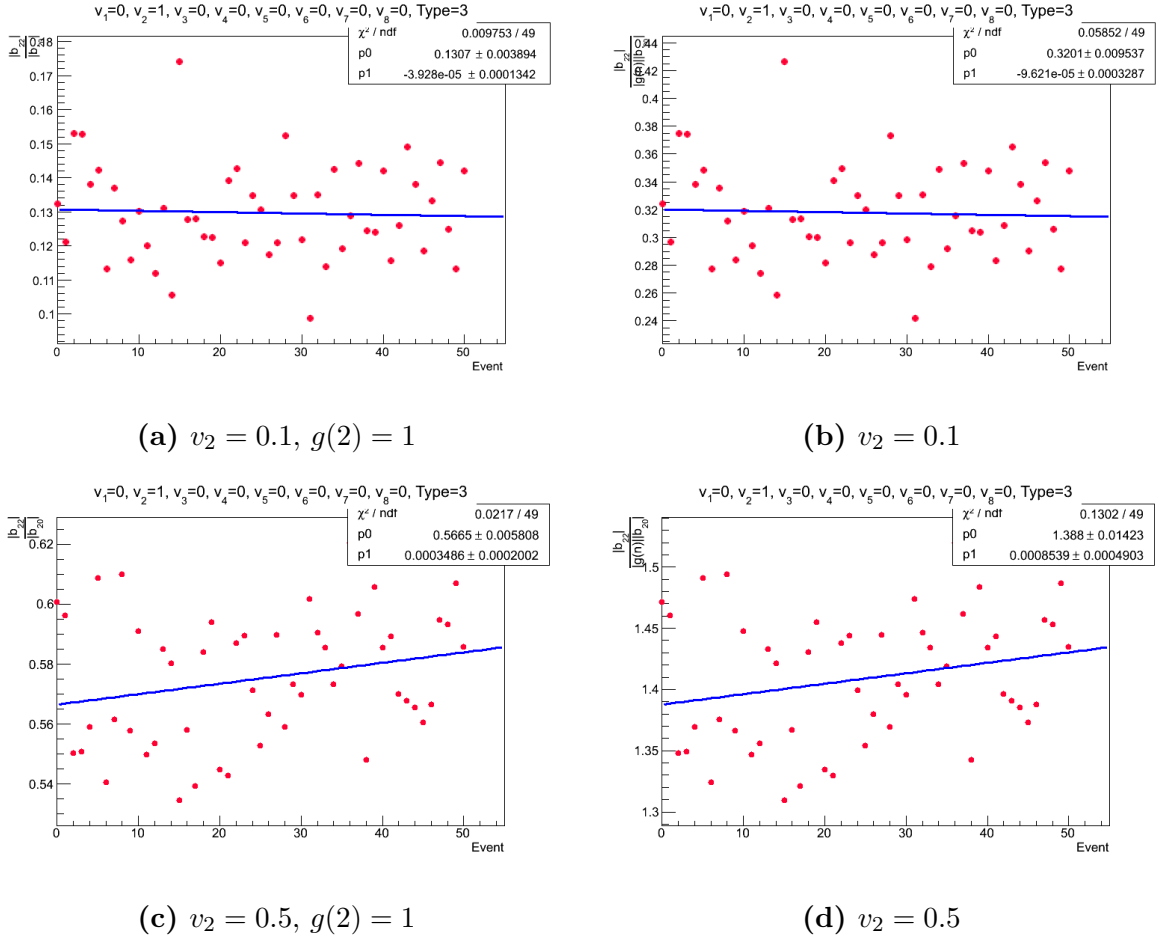


Figure 8.1: Plots of estimated flow with $v_2 = 0.1$ and $v_2 = 0.5$. Each red dot represents the estimate from one event, and the blue line is the best linear fit. The flow is estimated by the use of equation (5.13), but on the figures in the left panel the $g(2)$ factor has been omitted, which is indicated by the notation $g(2) = 1$. The binning is 201×402 , and the calculations is based on a collision with 30000 particles. The title on the files indicate which flow harmonics are imposed, where 1 indicate that flow has been imposed and 0 indicates that it has not.

As it appears from the figures the estimator $\frac{|b_{2,2}|}{|b_{2,0}|}$ is flow dependent, which can be seen by realizing that the flow estimators $\frac{|b_{2,2}|}{|b_{2,0}|}$ are distributed around $\sim 0.13 \pm 0.02$ and $\sim 0.58 \pm 0.04$, for events with $v_2 = 0.1$ and $v_2 = 0.5$ respectively. However it is also evident that the results are not in perfect agreement with equation (5.13), especially not when taking into account the $g(n)$ factor.

The choice of binning was dictated by the choice in [15] to be 201×402 . However this might not be the best choice since this leaves in the order of 80000 bins for only 30000

particles. A better choice might be 21×42 bins. The binning can in principle be chosen freely, however two things may influence the choice.

1. The highest even ordered flow harmonic n which can be estimated equals the highest number of multipoles l . The multipoles depend on the binning with an upper bound at $2l_{\max} + 1 = \cdot N_{\theta}$ and $N_{\theta} = 2N_{\phi}$.
2. High resolution (binning) relative to multiplicity, says little about collective behaviour.

The 21×42 is a good choice displaying the collective behaviour of the particle motions, and flow harmonics up to an order $n = 10$ can be calculated. Since the highest flow order is 8 in these events, an even better choice might have been 17×34 which improves the statistics. However in order to be consistent with the subsequent analysis the 21×42 binning is preferred. A comparison between maps with the 21×42 binning and 201×402 binning can be seen in figure (8.2).

As it appears from figure (8.2a), the bin content is fluctuating between one and three for most of the map. The relative fluctuations is very high as compared to figure (8.2b), and may to a much higher degree be ascribed to statistical fluctuations. Hence the low resolution map is better suited for the analysis. Estimations of the flow using this binning are shown in figure (8.3). And figure (8.4) shows a 1D histogram displaying the distribution of estimated flow on 1000 events with $v_2 = 0.1$. There are two mean values in the legend (white box in the upper right corner) of the figures. The first mean value, is the mean of the estimated flow. The second mean value, is the mean of the Gaussian fit. The value associated with ‘‘Sigma’’ (σ) is the value of one standard deviation.

A quick look at the figures reveals that by choosing a low resolution, the deviations from the mean is actually reduced, and in the case of the event with $v_2 = 0.5$, the mean of the estimated flow value is very close to the true flow. Another important fact when going to a low resolution map, is that v_n is less overestimated.

The proportionality factor between the flow and the mean of the estimated flow in figure (8.4a) is remarkably close to the slope of the curve on figure (5.7b). This is a peculiar coincidence since the estimated flow in figure (8.4a) is calculated without the $g(2)$ factor, whereas the $g(2)$ factor has been included in the calculation in figure (5.7b).

The next task in the analysis is to check whether it is possible to recreate figure (5.7b). The result is shown in figure (8.5), where the real flow is plotted against the estimated. At the very low values of v_2 the flow is not properly estimated e.g. $v_2 = 0.01$ is estimated to nearly 0.04, however as soon as leaving this limit there seems to be a beautiful correspondence between the true and the estimated flow. The blue line on the figure represents the best linear fit, where ‘‘p0’’ in the legend is the point of intersection with the 2.-axis and ‘‘p1’’ is the slope of the curve.

8.2.1 Determination of the symmetry plane

The last task of the first approach in the analysis of elliptic flow, is to check whether it is possible to recalculate the reaction plane. In the case of the 50 events shown in figure (8.5), the reaction plane for all events is $\frac{\pi}{9}$ (20°) (The reason for not just taking the default zero is to avoid fluctuations in the symmetry plane leading to an symmetry plane determination at $\sim \pi$.) The symmetry plane determination is shown in figure (8.6). It

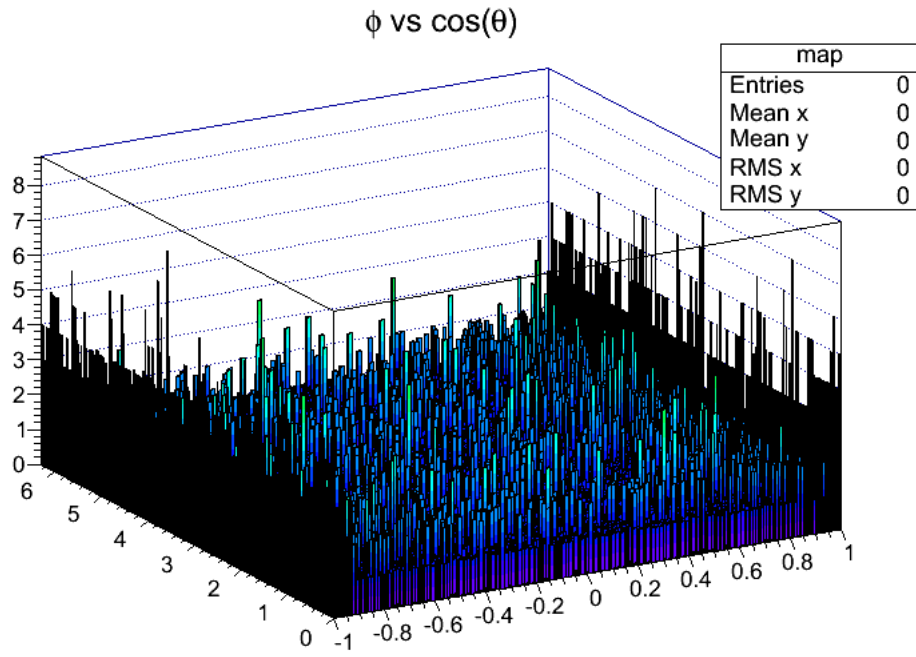
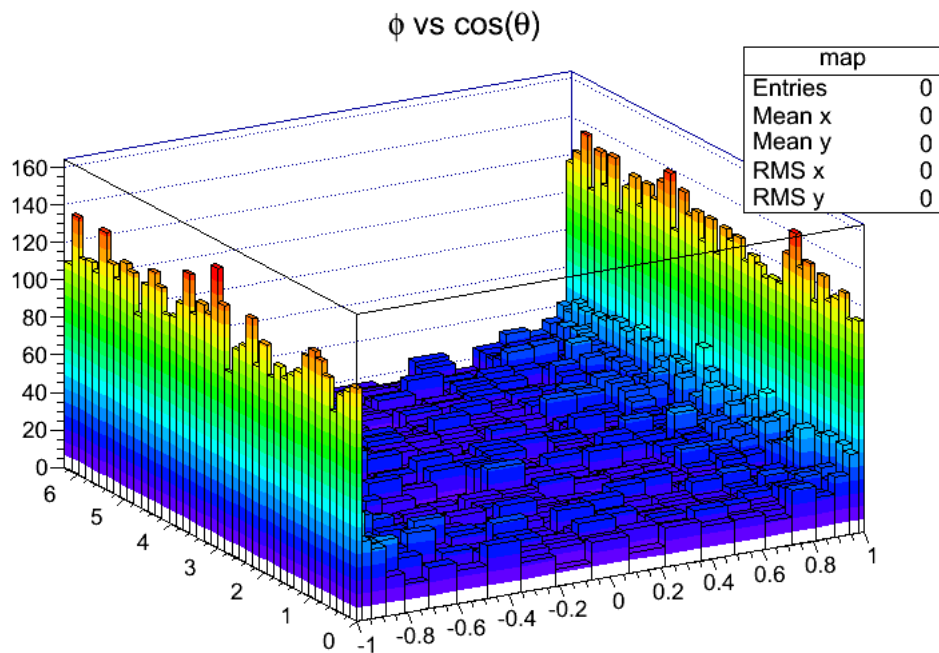
(a) 201×402 (b) 21×42

Figure 8.2: Two maps of an event with 30000 particles and no flow imposed. The binning is 201×402 and 21×42 respectively.

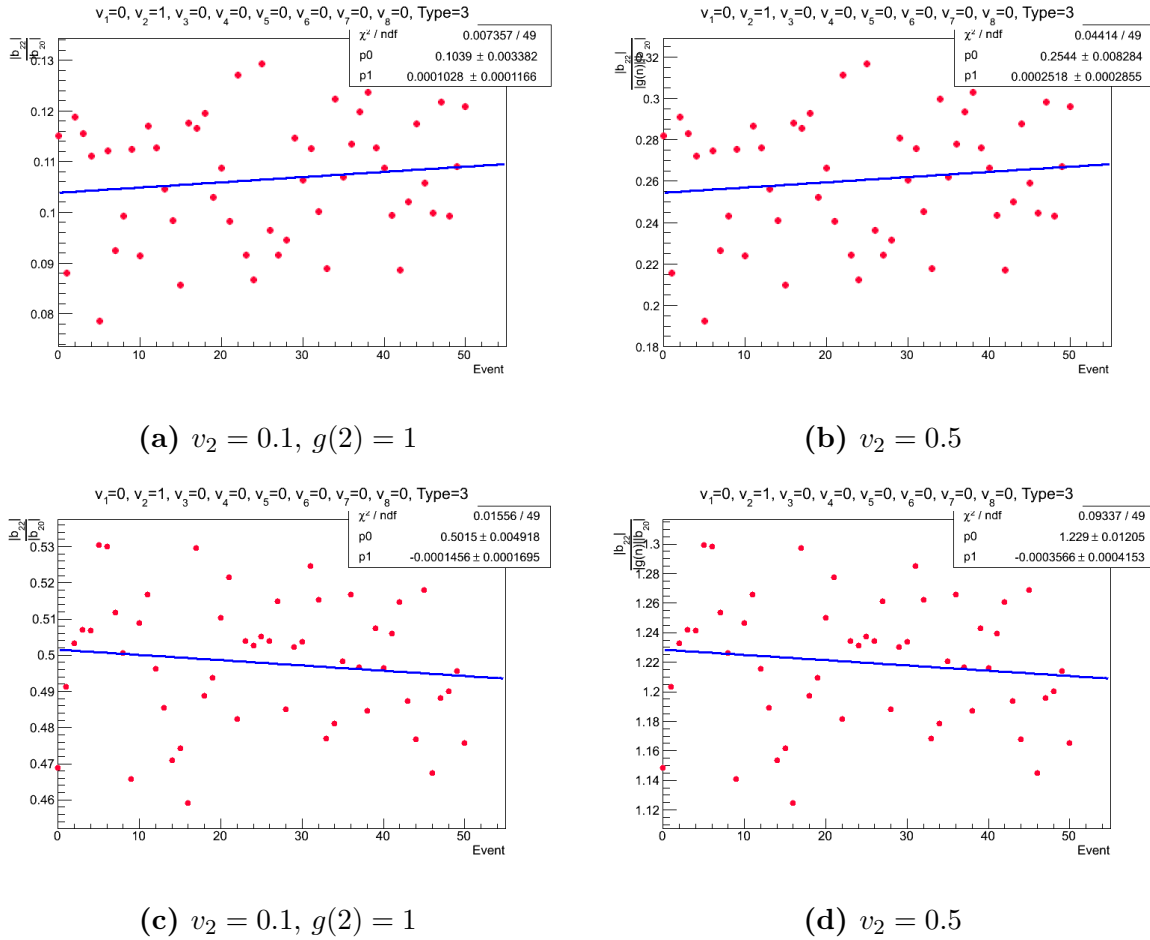


Figure 8.3: Low resolution flow estimation. The events are the same as in figure (8.1), but the binning is 21×42

appears from the figure that at high values of v_2 , the symmetry plane is quite precisely determined, whereas for lower values of v_2 , uncertainty increases. Obviously in the case of $v_2 = 0$ the symmetry plane cannot be determined. The Gaussian mean of the symmetry plane for 1000 events with $v_2 = 0.1$ and $\psi_2 = \frac{\pi}{9}$ is very close to that of ψ_2 as can be seen in figure (8.7).

Figure (8.8) shows the symmetry plane for 50 events with $v_2 = 0.1$. Starting at zero for each new event, the orientation of reaction plane is rotated by $\frac{\pi}{90}$. The intersection of the fitted line with the 2.-axis is almost perfectly zero (had the line been extended to intersect the 2.-axis), and the slope of the curve is within one standard deviation with respect to 1.

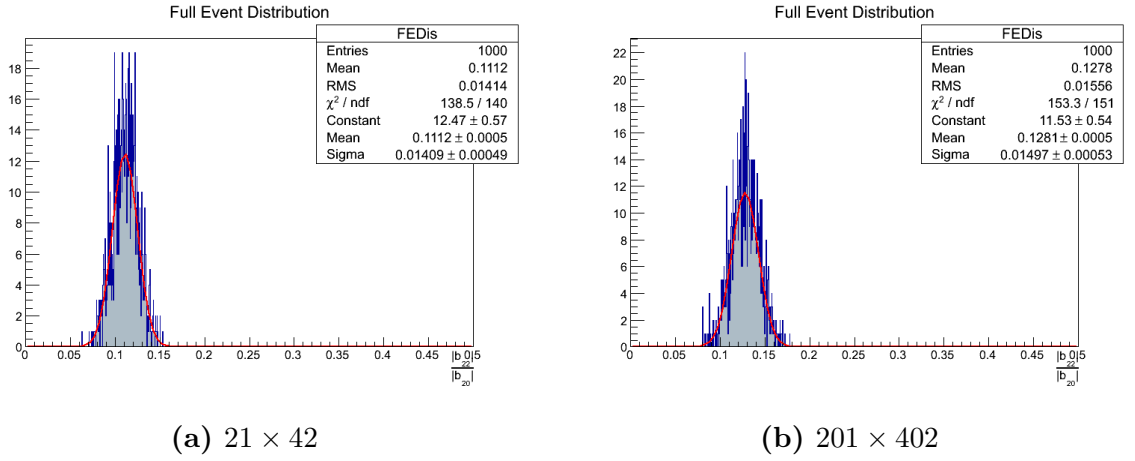


Figure 8.4: Histograms of flow estimation on 1000 events with $v_2 = 0.1$ for low and high resolution binning respectively, the red curve represents a Gaussian fit. The legend in the upper right corner has two mean values, the first is the true mean of the estimated flow. The second is the mean of the Gaussian fit, where “Sigma” represents the value of one standard deviation. The standard deviation is increased for the high resolution map, and furthermore there is a shift to the right.

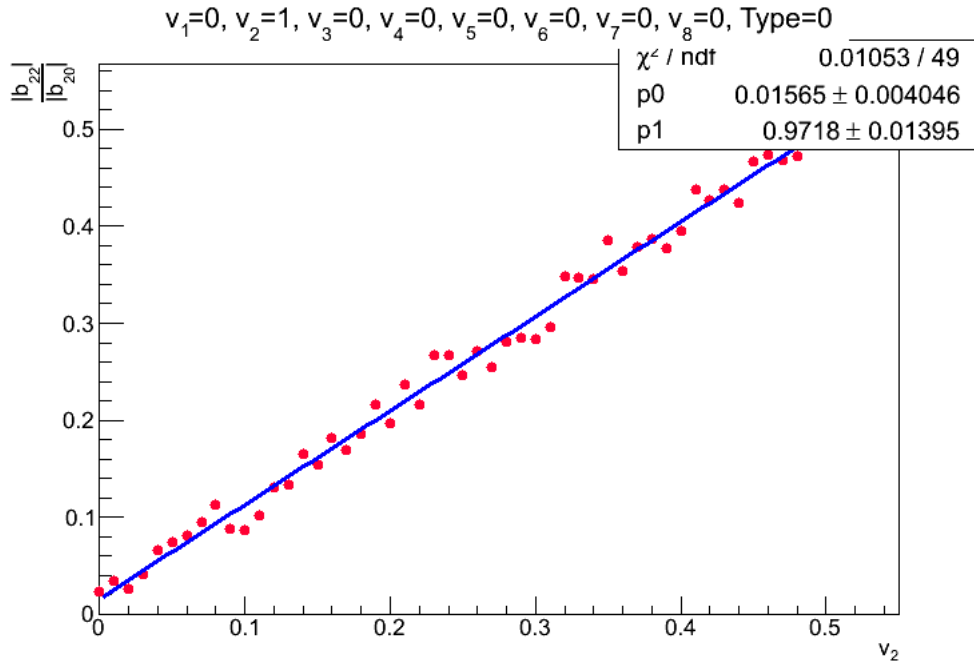


Figure 8.5: Graph of the elliptic flow estimation $g(n)$ factor omitted, on a series of 50 events with 30000 particles. Starting at zero for each new event the flow amplitude was increased by 0.01. Each red dot represents one event, and the blue line represents the best linear fit. “p0” in the legend is the point of intersection with the 2.-axis and “p1” is the slope of the curve. The proportionality factor (p1) is just within the limit of one standard deviation from the mean in figure (8.4a).

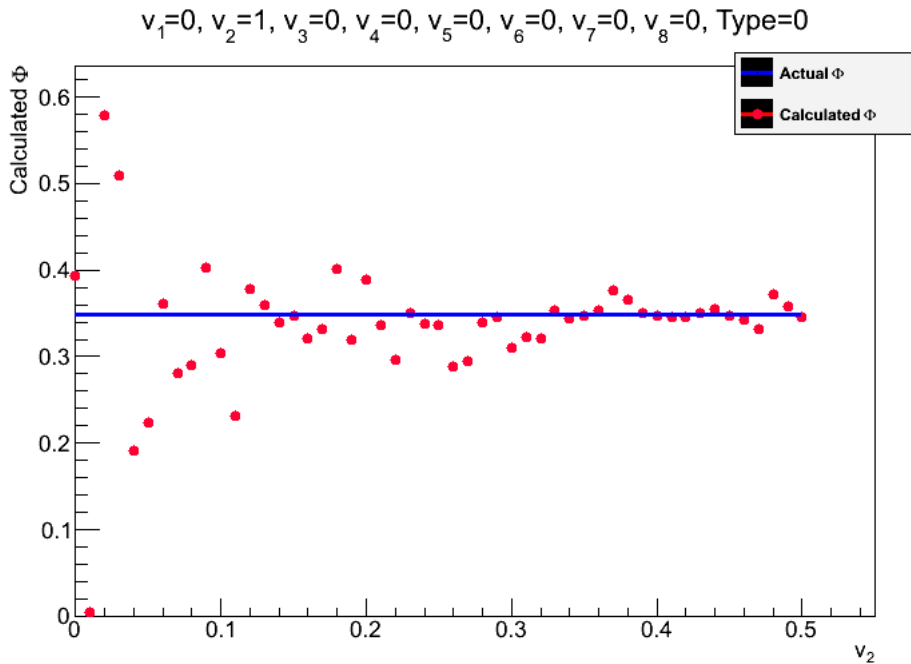


Figure 8.6: Symmetry plane determination for the 50 events shown in figure (8.5), the reaction plane is $\frac{\pi}{9}$ represented by the blue line.

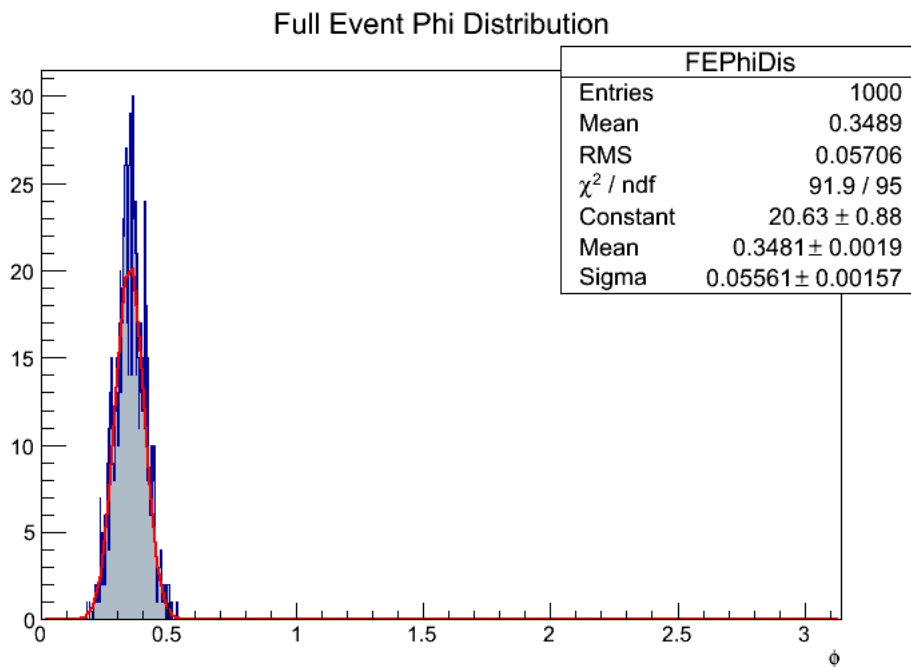


Figure 8.7: Symmetry plane determination for 1000 events each with $v_2 = 0.1$ and $\psi_2 = \frac{\pi}{9}$. The read curve represents a Gaussian fit.

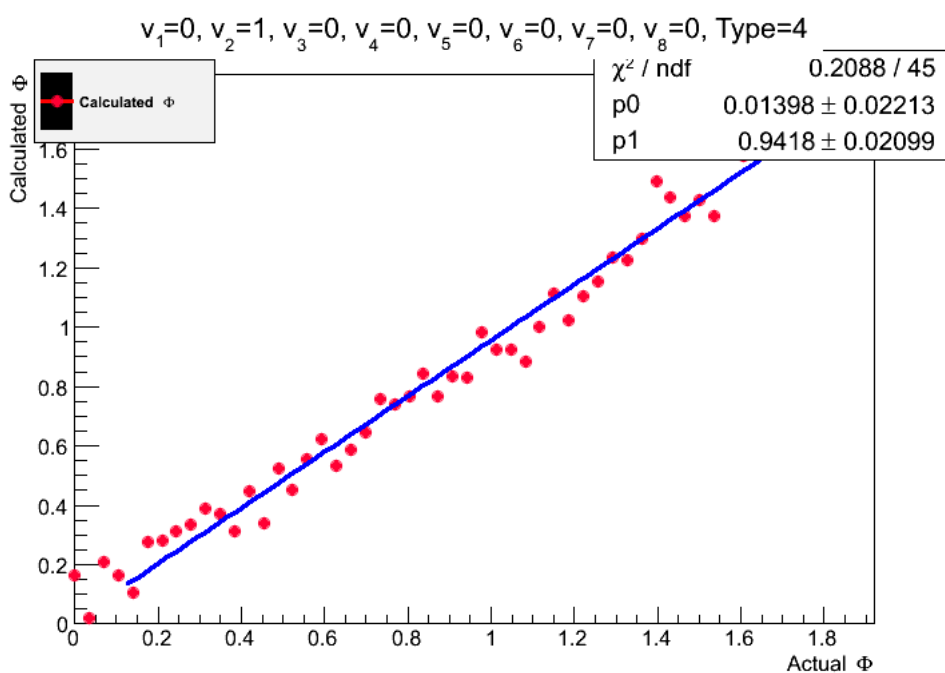


Figure 8.8: 50 events with $v_2 = 0.1$ and the reaction plane rotated by $\frac{\pi}{90}$ for each new event. Each red dot represents one event and the blue line represents the best linear fit. The fit has been cut off at the start point in order to avoid confusion between determination as zero or π .

8.3 Higher even order flow estimation

The preceding section found that there was a relation between the flow harmonic v_2 and equation (5.13) although the $g(n)$ factor had to be removed. However when the $g(n)$ factor was removed, there was an almost perfect agreement between the results obtained in GiRo and those obtained in [15]. The next step would be to check whether this is just a coincidence or equation (5.13) can also be applied to higher order flow harmonics. In the following calculations the $g(n)$ factor will be omitted. Figure (8.9) shows the

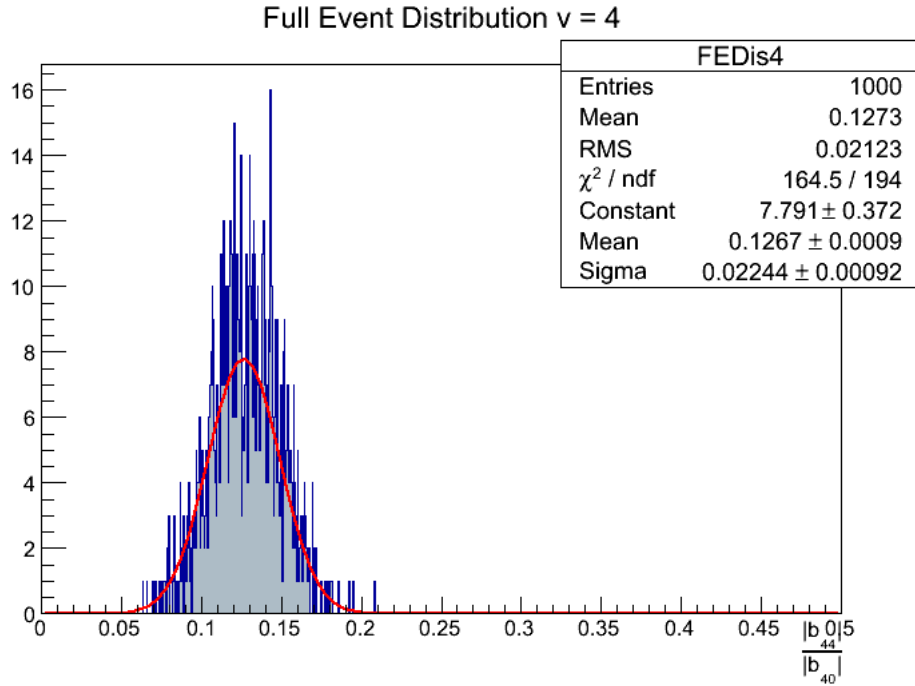


Figure 8.9: The distribution of estimated flow for 1000 events with for $v_4 = 0.1$. The $g(4)$ factor has been omitted. The red curve represents a Gaussian fit.

distribution of estimated flow for 1000 events with $v_4 = 0.1$. When comparing figure (8.9) with (8.4a), it is seen that the tendency for overestimation is increased a little in v_4 , and that the value of one standard deviation has also increased. This is reflected in figure (8.10), where the estimated flow is plotted against the v_4 . The slope of the curve is that of the proportionality factor between v_4 and estimated mean of v_4 in figure (8.9). The fluctuations from the linear fit are larger than those in figure (8.5). From figure (8.11) and (8.12) it is seen that the tendency of the flattening of the Gaussian curve and the overestimation of the flow harmonics is intensified when going to higher orders.

Hence it appears that although equation (5.13) is not entirely correct in case of the A-pixelization, the method still seems to be valid when leaving out the $g(n)$ factor. However the estimated value of the flow harmonics is generally too high, a tendency which is intensified when going to higher orders, where also the uncertainty of the estimation increases.

It is remarkable that quite the opposite seems to be the case in the symmetry plane determination, where the uncertainty actually decreases when going to higher orders of

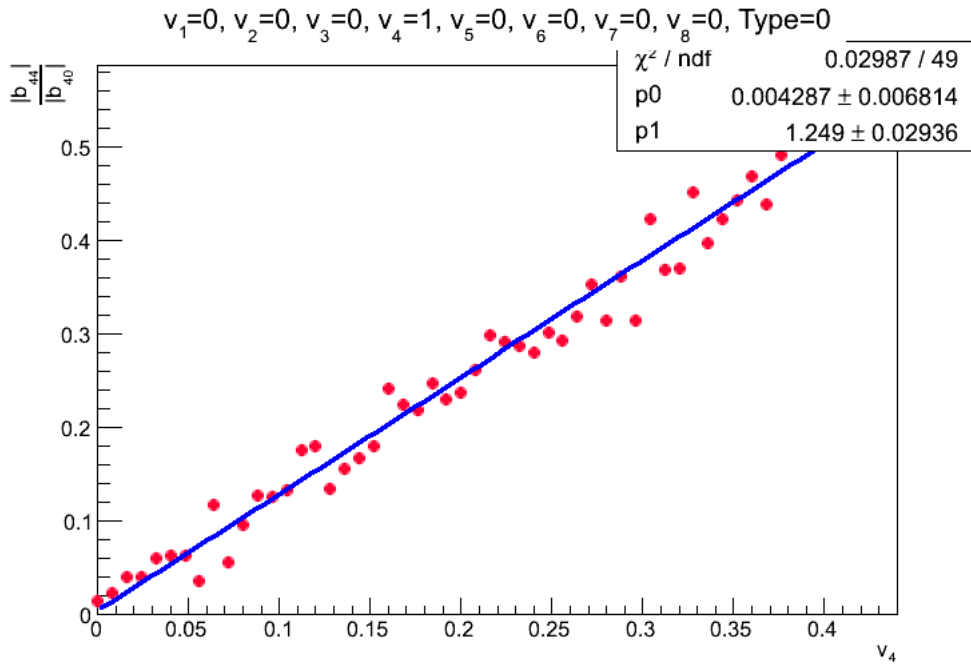
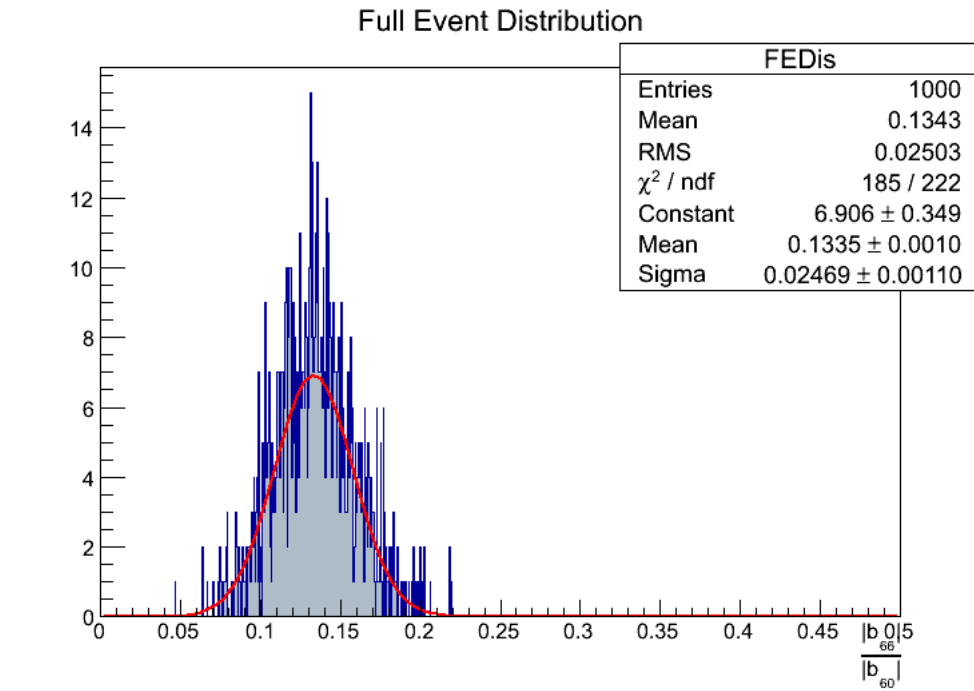
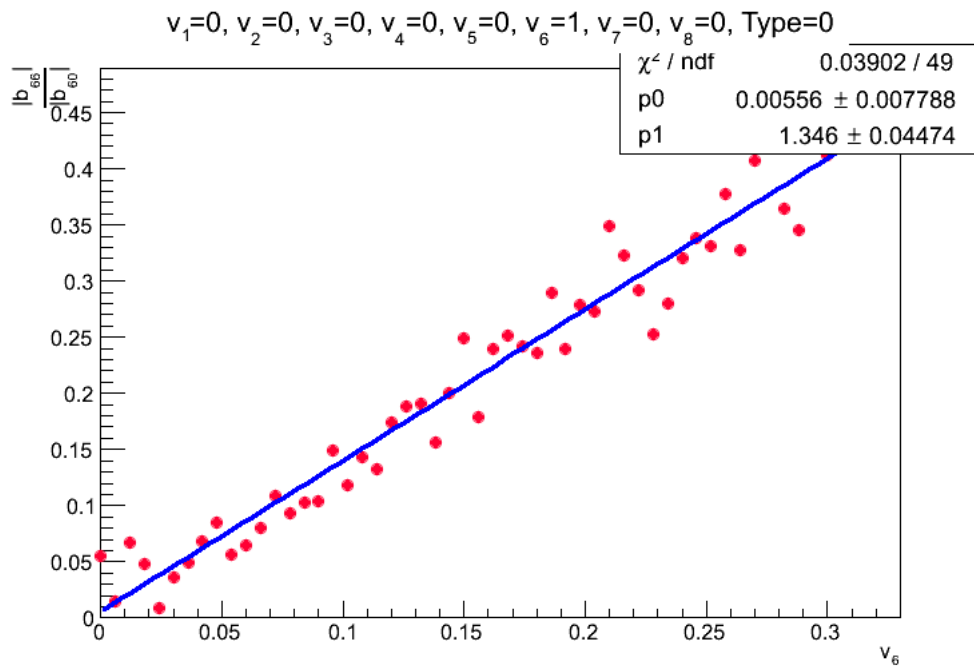


Figure 8.10: The estimated value of v_4 plotted against v_4 for 50 events containing only v_4 . Each red dot represents one event and the blue line is the best linear fit.

v_n . This is illustrated in figure (8.13) to (8.14). By making a comparison between figure (8.14b) and (8.6) it is seen that the symmetry planes are distributed tighter around the reaction plane in figure (8.14b) (Note the different scales). However it must be taken into account that the range upon which ψ_n is defined, decreases for larger values of n , hence the uncertainty on ψ_n relative to the range upon which ψ_n is defined, still increases with n .



(a) $v_6 = 0.1$



(b) Increasing v_6

Figure 8.11: Estimation of v_6 . The figure on panel 8.11a shows the distribution of 1000 events with the red curve being a Gaussian fit. The figure on panel 8.11b shows the estimated flow plotted against the true flow, where each red dot represents one event and the blue line represents the best linear fit.

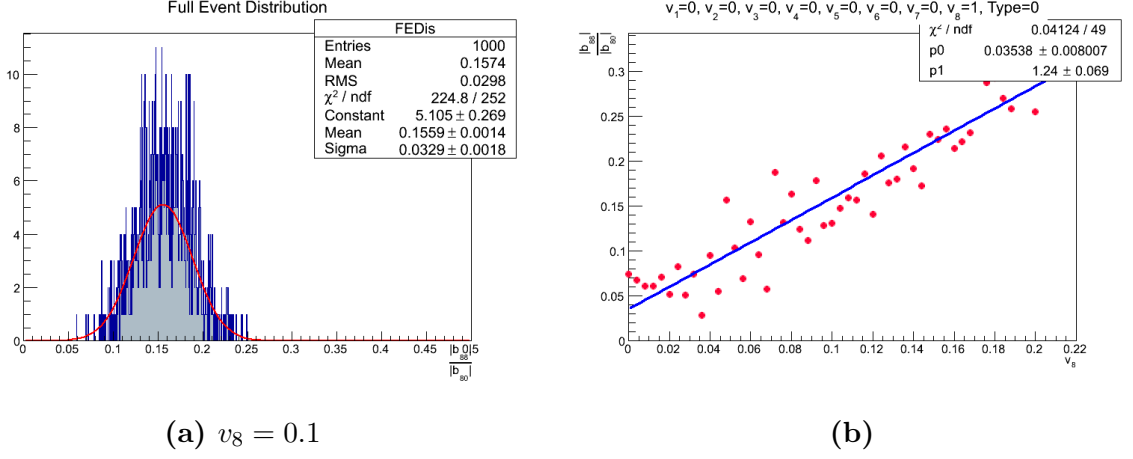


Figure 8.12: Estimation of v_8 . The figure on the left panel shows the distribution of 1000 events with the red curve being a Gaussian fit. The figure on the right panel shows the estimated flow plotted against the true flow, where each red dot represents one event and the blue line represents the best linear fit.

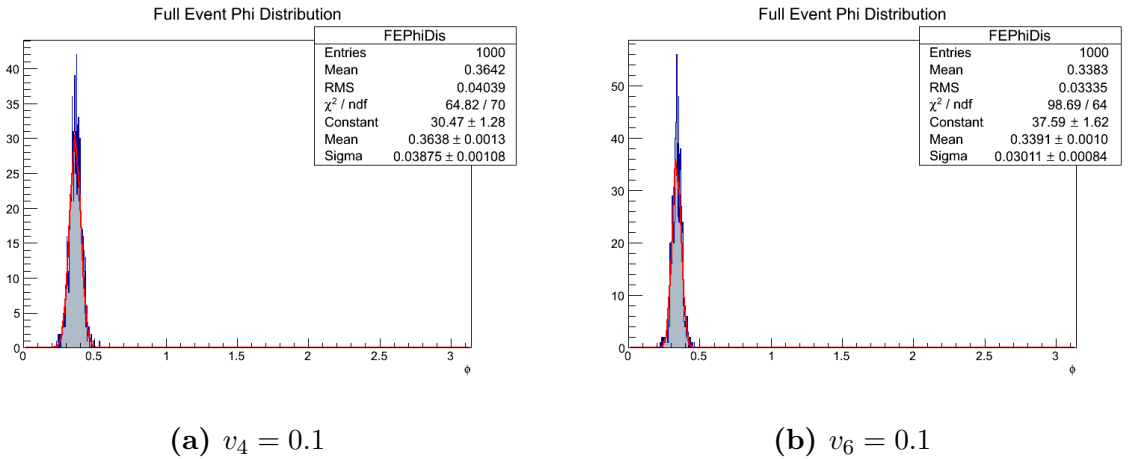
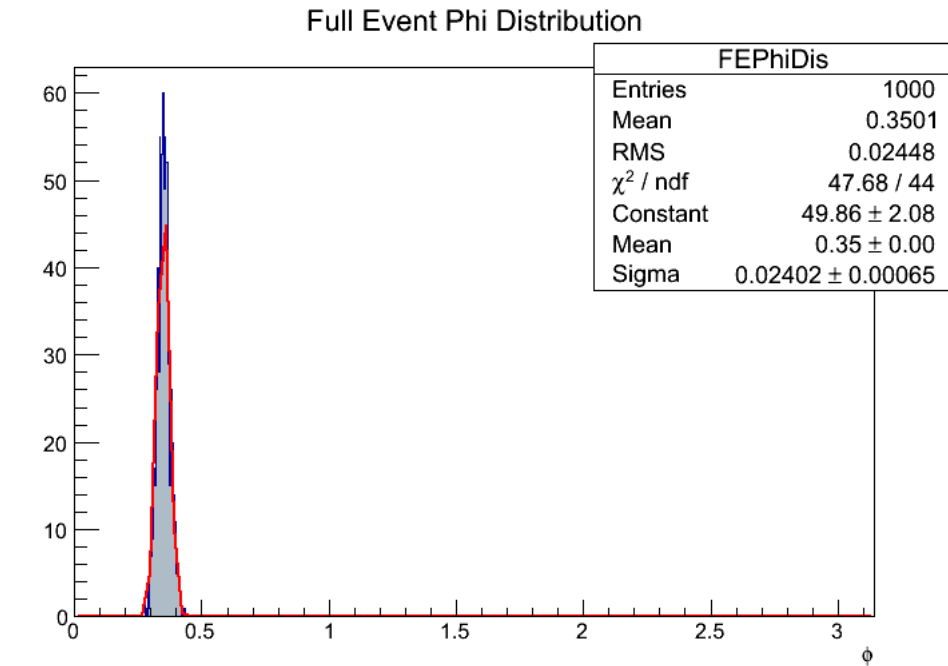
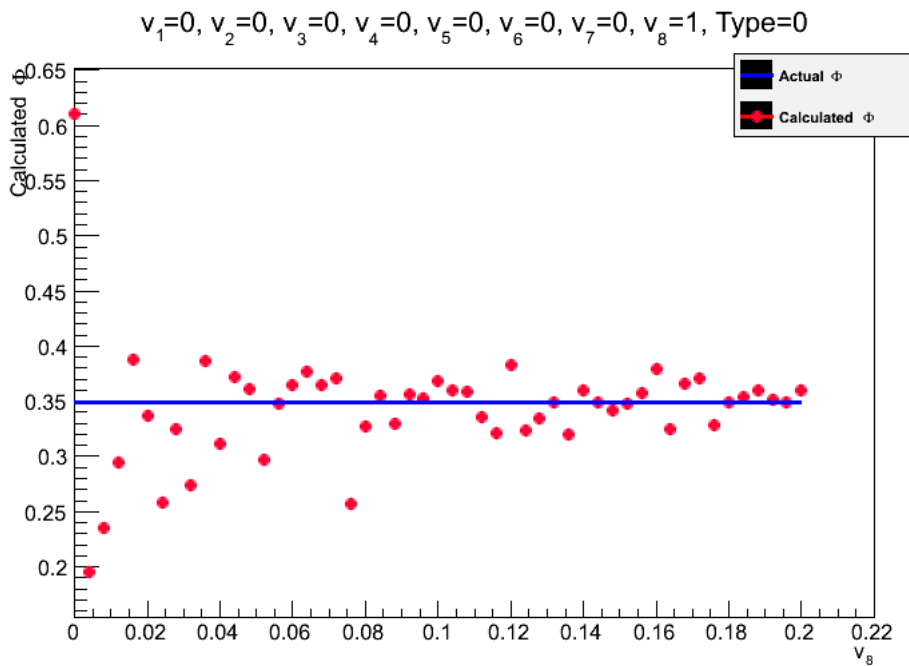


Figure 8.13: Symmetry plane determination of ψ_4 and ψ_6 , where the left panel displays the distribution from 1000 events.



(a) $v_8 = 0.1$



(b) increasing v_8

Figure 8.14: Symmetry plane determination of ψ_8 , where panel 8.14a displays the distribution from 1000 events and panel 8.14b shows the symmetry plane as a function of increasing v_8 .

8.4 Odd order flow estimation

In the case of odd flow harmonics, based on the experience from the case of even flow harmonics, the $g(n)$ factor will immediately be omitted from equation (5.20). Apart from that, the same initial approach is taken, and 50 events are produced each with $v_3 = 0.1$. However equation (5.20) is not in any sense able to give a proper estimation of the input value of v_3 as can be seen in figure (8.15). The reason for this becomes clear

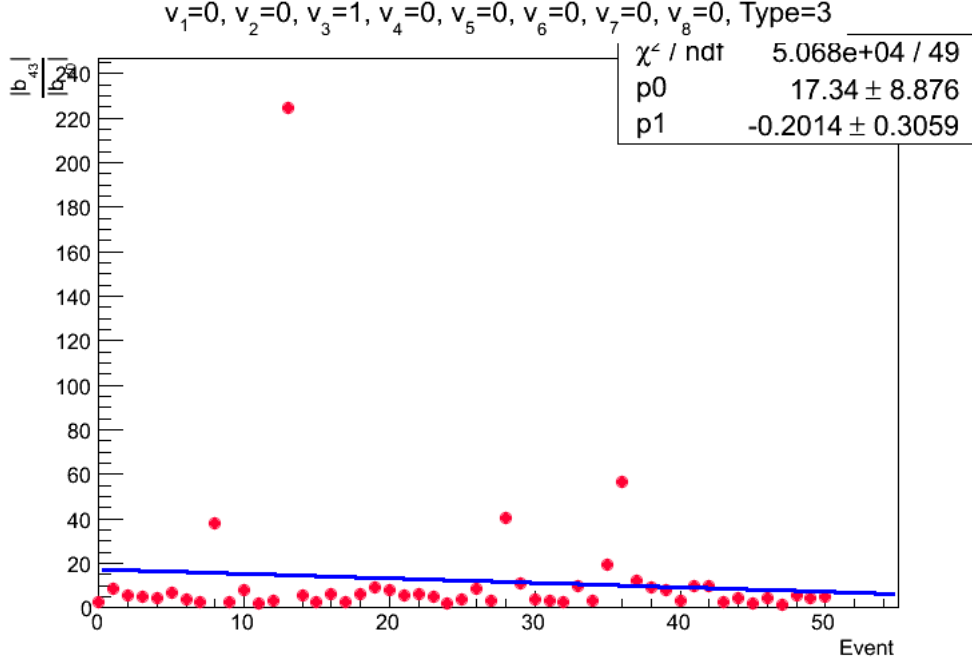


Figure 8.15: Flow estimation on 50 events with $v_3 = 0.1$.

by considering the spherical harmonic $Y_4^3(\theta, \phi)$. This harmonic is antisymmetric in θ as can be seen in figure (8.16). Hence the signal must be calculated as an average over the northern hemisphere and the southern hemisphere. This triples the calculations (one for the entire map, one for the northern hemisphere and one for the southern hemisphere) if it is desired to estimate both the even and odd order harmonics, however the calculations are trivial.

In the case of odd harmonics equation (3.14) will be evaluated as

$$a_{l,m} = \frac{\int_0^1 \int_0^{2\pi} [Y_l^m(\theta, \phi)]^* f(\theta, \phi) d\phi d \cos(\theta) + \int_{-1}^0 \int_0^{2\pi} [Y_l^m(\theta, \phi)]^* f(\theta, \phi) d\phi d \cos(\theta)}{2} \quad (8.1)$$

which can be done by using the cut operation described in section 6.1.3.1. When calculating the $a_{l,m}$ coefficients by equation (8.1), a plot like that in figure (5.7b) can also be obtained for the odd harmonics. This is illustrated for v_3 in figure (8.17). It appears from figure (8.17) that not only is the linear dependence of v_3 on the $a_{l,m}$ coefficients maintained, but the slope of the curve is also in accordance with the pattern seen from the even ordered harmonics.

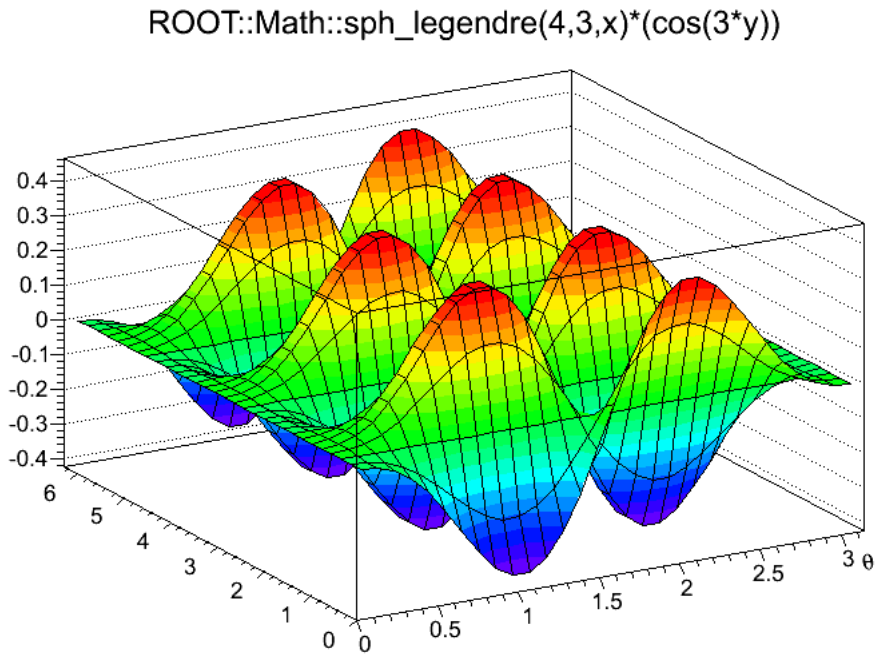


Figure 8.16: $\text{Re}[Y_4^3(\theta, \phi)]$

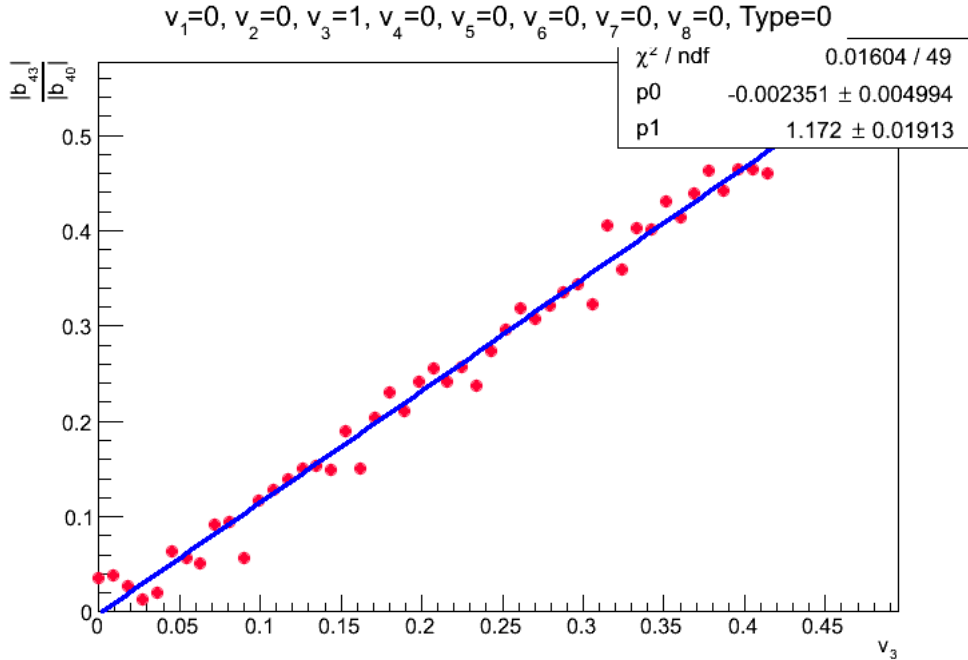


Figure 8.17: v_3 estimation by average over northern and southern hemisphere: Estimated flow plotted against true flow.

A Gaussian fit to the distribution of 1000 events is seen in figure (8.18), interestingly the mean is actually closer to 1 than for any of the even order harmonics. The standard deviation for v_3 is a little larger than v_2 , but smaller than for v_4 . To check that this is not a coincidence the distribution of estimated flow for 1000 events with $v_7 = 0.1$ is shown in figure (8.19), where it is clear from the figure that both the mean and the standard deviation are very close to that of v_4

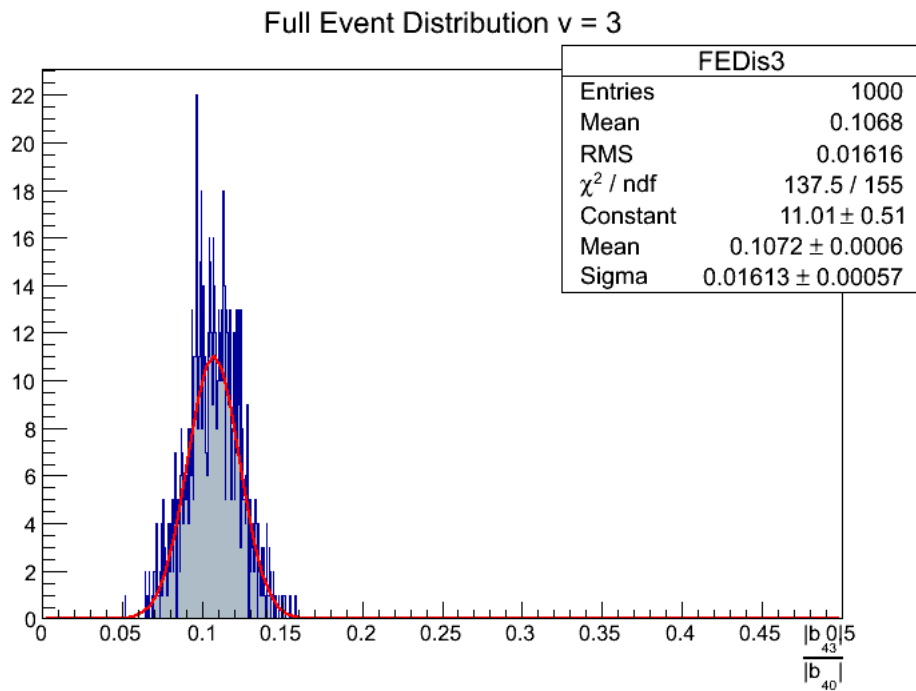


Figure 8.18: Distribution of estimated flow from 1000 events with $v_3 = 0.1$

However an interesting thing happens when considering the 5th harmonic shown in figure (8.20). It appears that both the mean and the standard are twice as large as expected. This fact is not explained. In the subsequent analysis it will not be mentioned, but it appears through the entire analysis.

8.4.1 Conlusional remarks

As a conclusion for this chapter, the analysis so far has revealed that it is possible to use the spherical harmonics to give an estimation of the flow harmonics v_n . When omitting the $g(n)$ factor all estimated values of v_n is fairly close to the true value of v_n . However both in the case of even and odd harmonics the uncertainty increases when going to higher harmonics. When leaving out the 5th harmonic, the value of v_n is generally better estimated for odd harmonics than for even.

The choice of binning is important in the analysis, a higher resolution allows for estimation of higher order flow harmonics, but if the particle multiplicity do not match the high resolution there will be an increase in uncertainty. In the analysis performed above the binning was chosen to be 21×42 , although even better results would be obtained

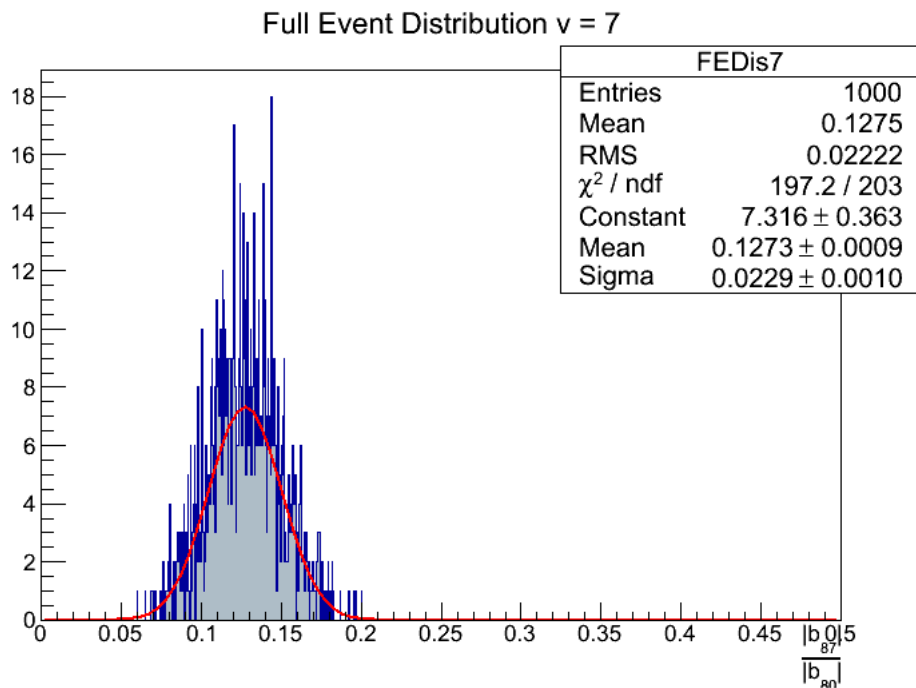


Figure 8.19: Distribution of estimated flow from 1000 events with $\nu_7 = 0.1$

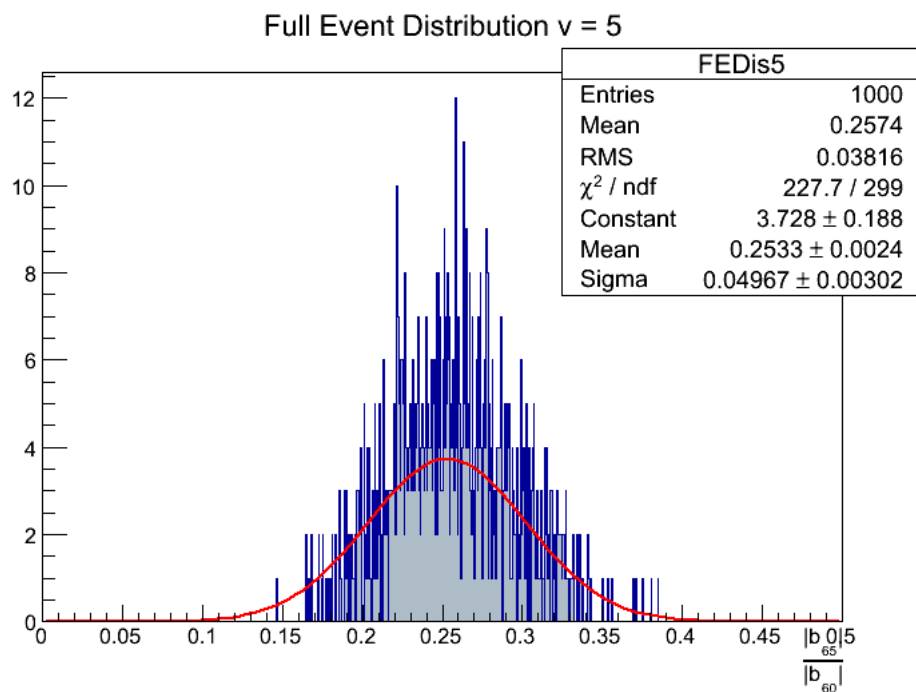


Figure 8.20: Distribution of estimated flow from 1000 event with $\nu_5 = 0.1$

if the choice had been 17×34 , since this allows for analysis of all eight flow orders and increases the statistic in each bin.

Chapter 9

Analysis of multiflow events

Chapter 8 was concerned with the analysis of only a single flow harmonic in each event. The analysis provided knowledge about the basic properties of equation (5.13), (5.14), (5.20) and (5.21). However the analysis is based on a simplified case since an event is generally expected to contain several flow harmonics although with varying amplitude. In this chapter the analysis is focused on multiflow events. The analysis considers two scenarios: one where the orientation of reaction planes for all harmonics are equal, and one with unequal reaction plane orientation.

9.1 Analysis with equal reaction planes

The analysis with multiflow and equal reaction planes is still a simplified case, since this scenario is definitely not expected in a real collision. However this case exhibits some nice features, which are worth noting. In all events analysed in this section, the particle multiplicity will be 30000 and the orientation of the reaction plane is $\frac{\pi}{9}$. Figure (9.1) shows the distribution of 1000 events with imposed flow $v_n = 0.1$ for all orders up to 8. It appears that the estimate of the individual flow harmonics is almost unaffected by the other harmonics. Especially the estimate of the elliptic flow is almost identical in the multiflow case to the single flow case. A comparison between figure (9.1f) and (8.12a) shows that the standard deviation is actually decreased a little in the multiflow case where also the overestimation is reduced.

The determination of the symmetry planes is comparable to the case of single flow events, which is illustrated in figure (9.2). As in the previous chapter, it appears that when going to higher orders the uncertainty on the determination is diminished.

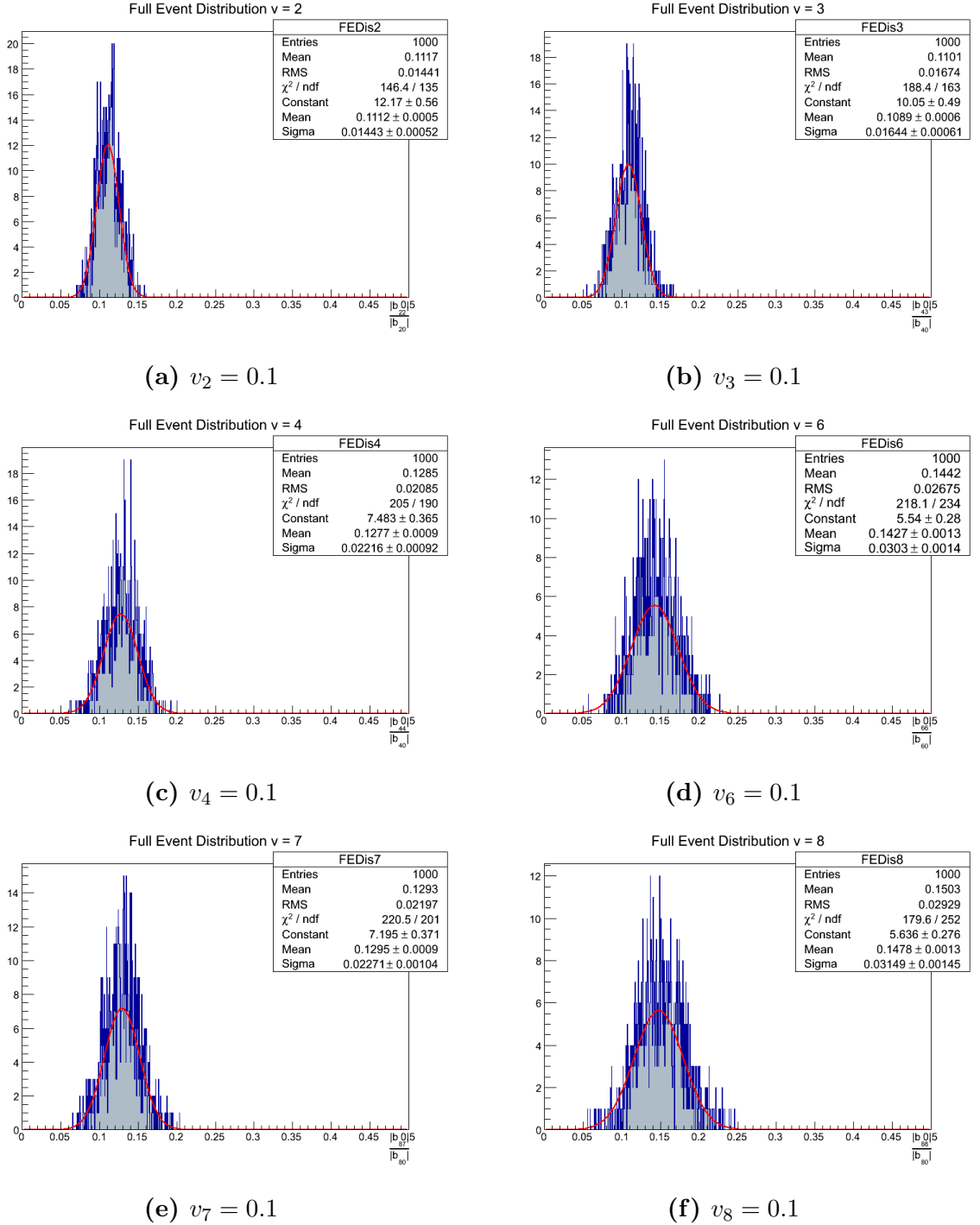


Figure 9.1: The distribution of estimated flow from 1000 events with $v_1 = v_2 = \dots = v_8 = 0.1$ and $\psi_1 = \psi_2 = \dots = \psi_8 = \frac{\pi}{9}$.

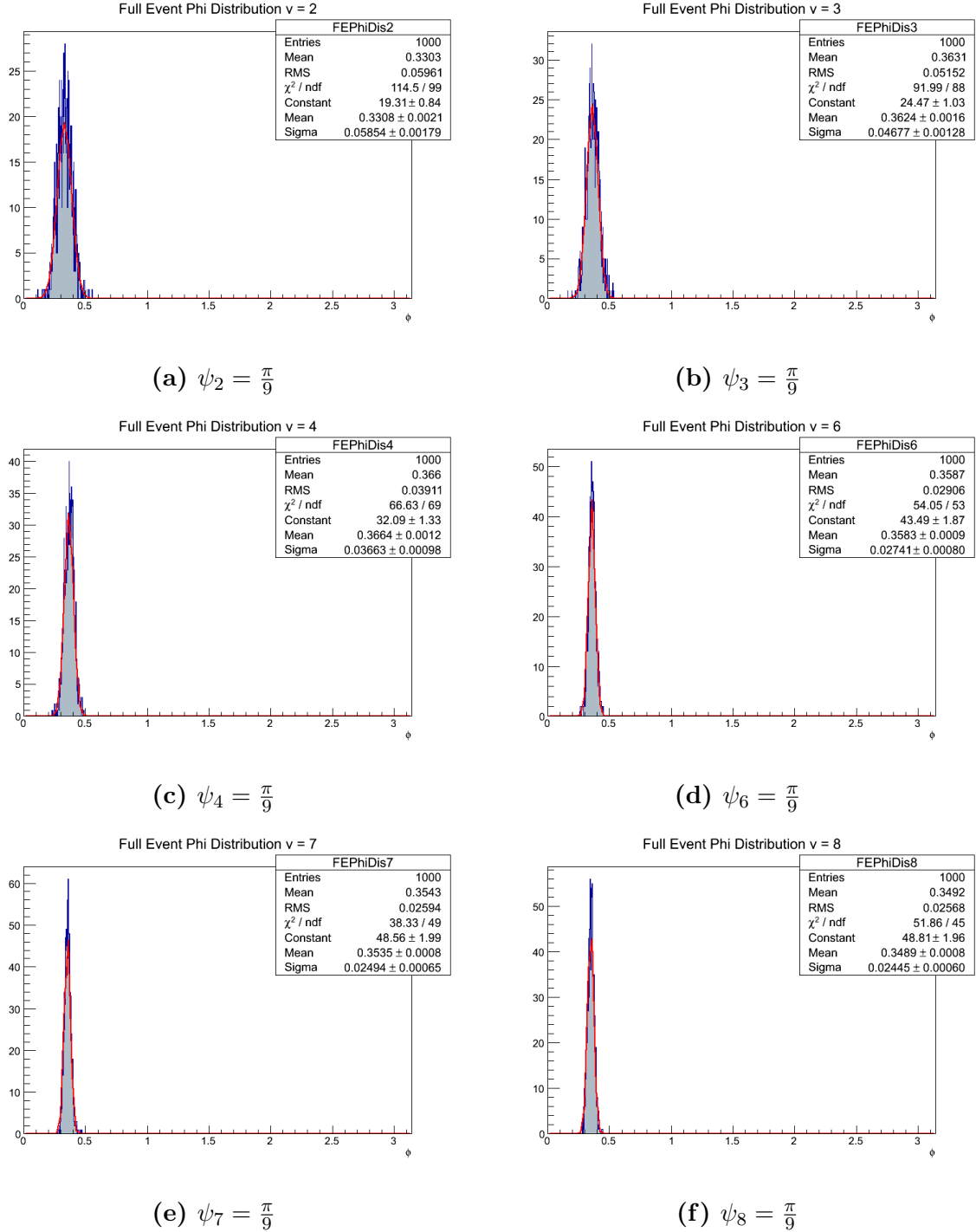


Figure 9.2: The distribution of symmetry planes for 1000 events with $v_1 = v_2 = \dots = v_8 = 0.1$ and $\psi_1 = \psi_2 = \dots = \psi_8 = \frac{\pi}{9}$.

9.2 Analysis with unequal reaction planes

It still remains to check whether the results up when the reaction planes are not the same for all harmonics. Again 1000 events with all flow harmonics ($n = 1 - 8$) at $v_n = 0.1$ are considered, but in this case the reaction planes are defined by

$$\psi_n = \frac{\pi}{9} + \frac{n\pi}{18} \quad (9.1)$$

It appears from the result shown in figure (9.3) that the flow estimation from these events is nearly unaffected by the change.

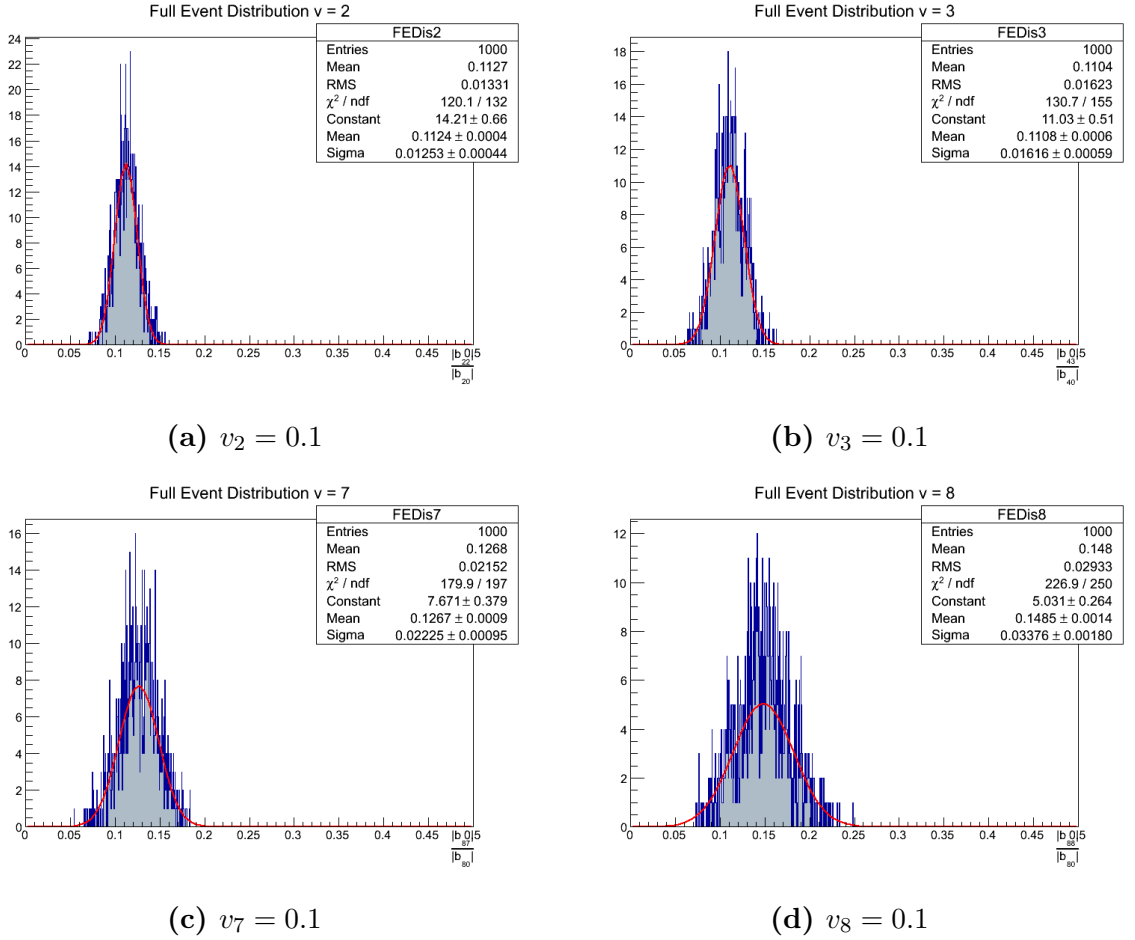


Figure 9.3: The distribution of estimated flow for 1000 events with $v_1 = v_2 = v_3 = v_4 = v_5 = v_6 = v_7 = v_8 = 0.1$ and $\psi_n = \frac{n\pi}{18}$.

A reproduction of figure (5.7b) may now be attempted. Since flow harmonics do not generally have the same amplitude and the second order harmonics is the strongest, the flow amplitudes are imposed relative to each other and are related by the equation:

$$v_n = \begin{cases} v_n = 0.5v_0, & n = 1 \\ v_n = (1.2 - n0.1)v_0, & n \geq 2 \end{cases} \quad (9.2)$$

where v_0 is the variable determining v_n . Following equation (9.2), a series of 50 events is produced with all flow harmonics imposed. v_0 starts at zero and is increased by 0.01 for each event. In the case of low order harmonics the results are actually in very good agreement with previous result from simpler cases. The case of elliptic flow is shown in figure (9.4). When going to higher order harmonics the uncertainty on the results increases

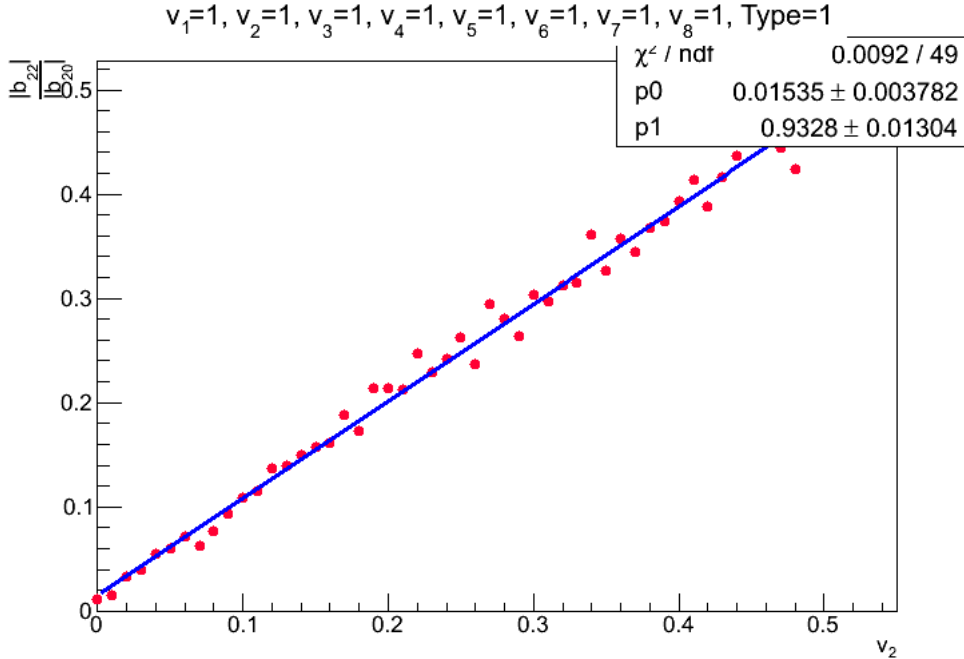


Figure 9.4: Estimation of v_2 with all flow harmonics present and related by equation (9.2) and the reaction planes given by equation (9.1).

dramatically as can be seen in figure (9.5). This should however not be a surprise since when increasing the amplitude well above 0.1 the signal is heavily influenced by lower order harmonics.

The symmetry plane determination is well behaved in the case of low order harmonics. But when going to higher order harmonics results become unreliable. The symmetry plane determination of odd harmonics has an additional source of error. The reason is that values approximating the limits of the range upon which ψ_n is defined, may be determined either near the lower limit or near the upper limit. This concept is illustrated in figure (9.6). Since the symmetry planes of the odd harmonics is determined as an average between the southern and northern hemisphere, the chance of the splitting is doubled. This is illustrated in figure (9.7) for the fifth harmonic.

However the situation with all harmonics achieving values obtained by inserting $v_0 = 0.5$ into equation (9.2), is very unlikely. In figure (9.9) and (9.8) the analysis has been performed by use of equation (9.2). As in the previous analysis a series of 50 events are considered. All flow harmonics but one are kept at a constant value given by $v_0 = 0.2$. The remaining flow harmonic is increased by letting v_0 increase by 0.01 for each event. Figure (9.9) shows the analysis performed on the flow harmonic, where the estimated flow

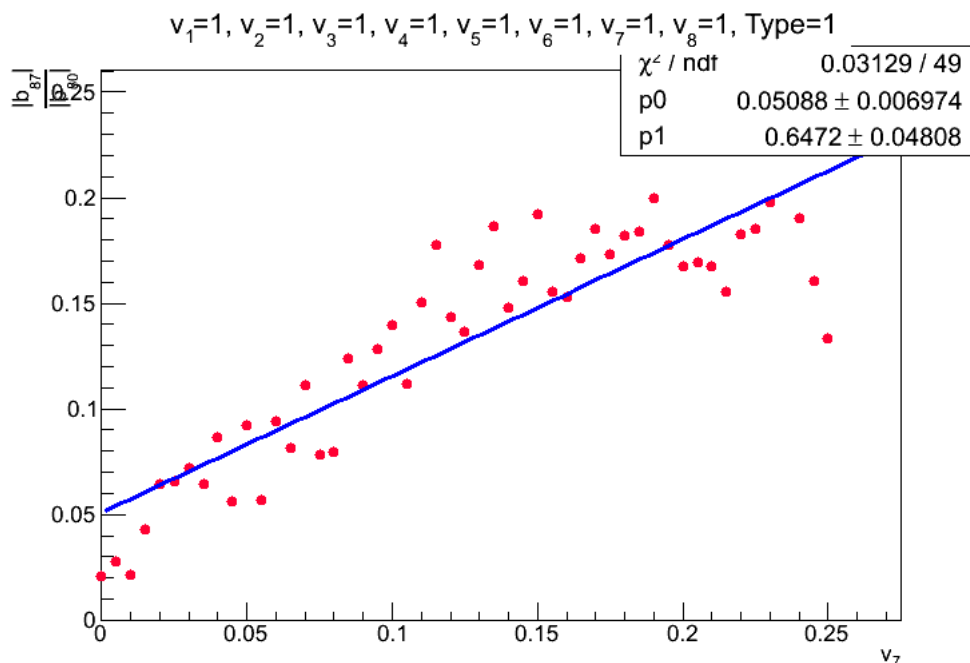


Figure 9.5: Estimation of v_7 with all flow harmonics present and related by equation (9.2) and the reaction planes given by equation (9.1).

of the one harmonic which is not kept constant is plotted against the true flow of that harmonic.

9.2.1 Remarks on the flow analysis

The results so far in the single and multi flow analysis clearly shows a linear dependence of the estimated flow on v_n . Apart from the 5th flow harmonic, the equations $v_n = \frac{|b_{n,n}|}{|b_{n,0}|}$ and $v_n = \frac{|b_{n+1,n}|}{|b_{n+1,0}|}$ for even and odd ordered harmonics respectively, seems to be good approximations when taking into account corrections for higher orders. However it appears from the figures that the slope of the curves is exactly the same as the proportionality factor of the 1000 event distributions of estimated flow. E.g. comparing figures with increasing elliptic flow (figure (8.5),(9.4) and (9.8b)) to 1000 event distribution of estimated elliptic flow (figure (8.4a), (9.2a) and (9.3a)) it is seen that the slope of the curves is generally just below 1, whereas the proportionality factor of the 1000 event distributions is around 1.1. This may be due to small variations in the linearity for various sizes of v_2 . Hence in order to get a more comprehensive understanding of the flow estimation, statistics have to be achieved for more values of v_n instead of just for $v_n = 0.1$. This has not been performed in this thesis.

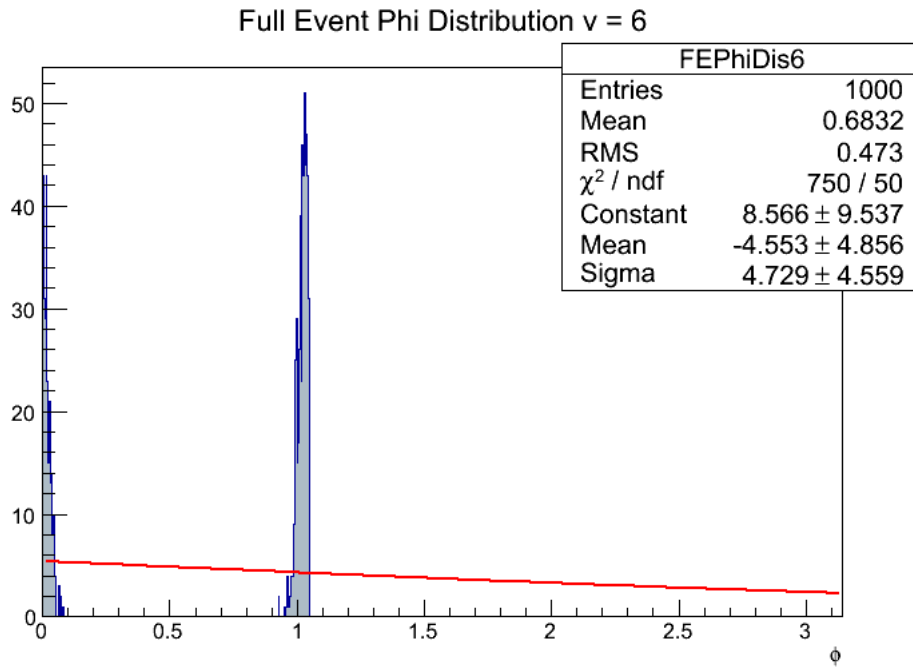


Figure 9.6: Symmetry plane determination of $\psi_6 = \frac{\pi}{3}$. Since ψ_6 is only defined in the range $\psi_6 \in [0; \frac{\pi}{3}]$ the symmetry plane approximates either the upper or the lower limit.

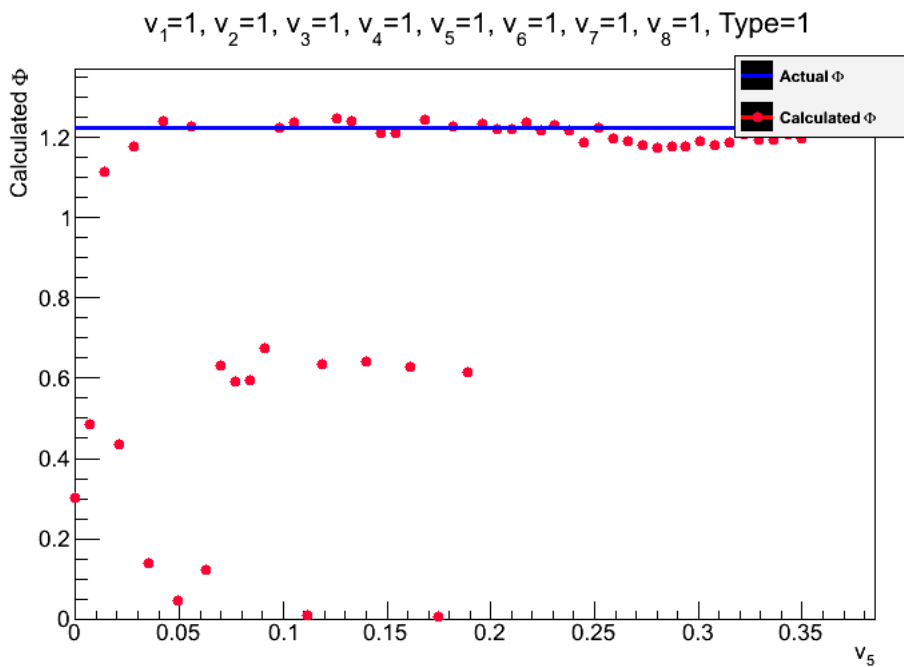


Figure 9.7: Symmetry plane determination of ψ_5 . The symmetry plane is determined in three different bands

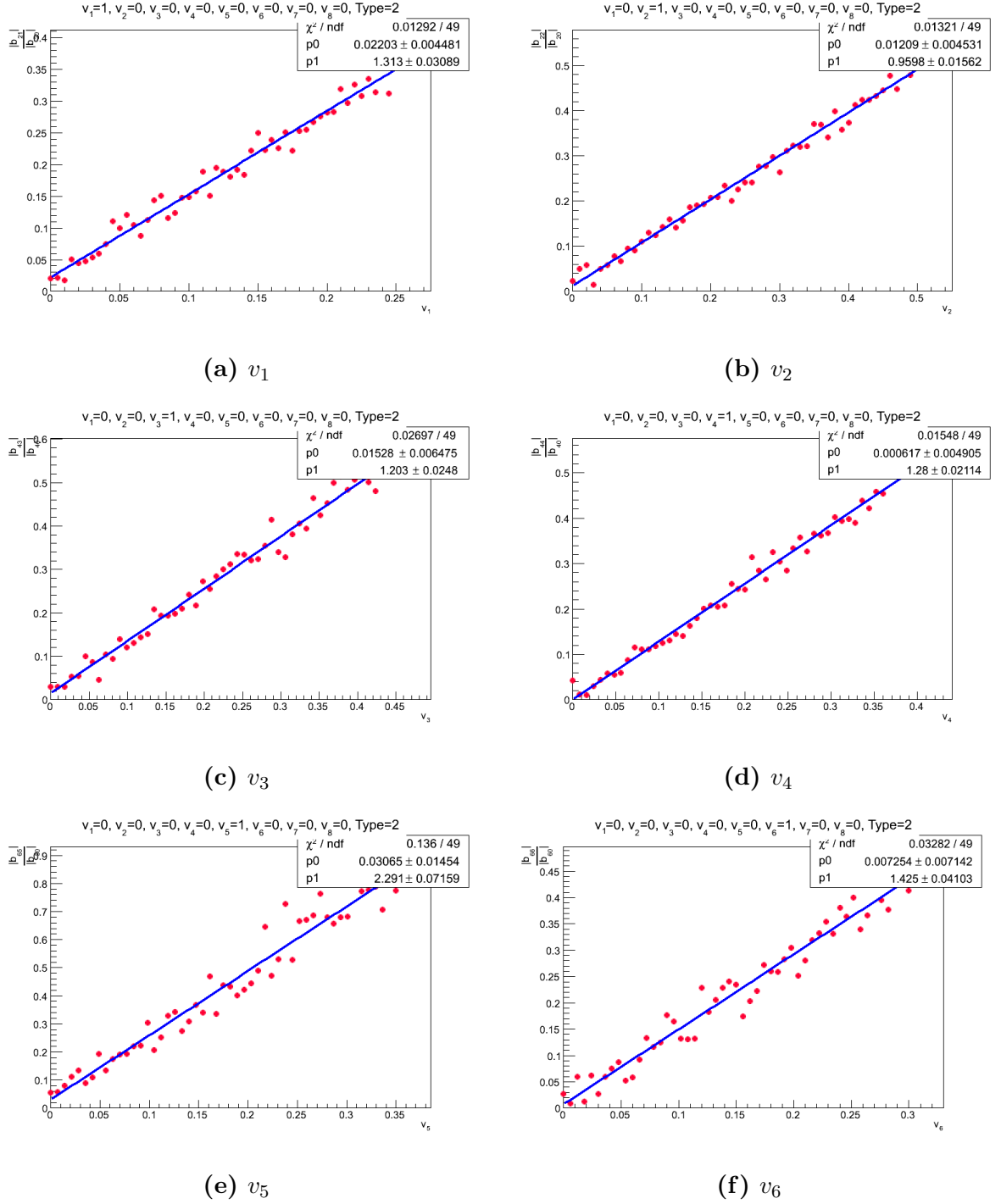


Figure 9.8: Analysis of a series of 50 events with all flow harmonics but one kept at a constant level given by $v_0 = 0.2$ in equation (9.2). Each panel represents the flow estimation of the harmonic which is not kept constant and plotted against the true flow of that harmonic.

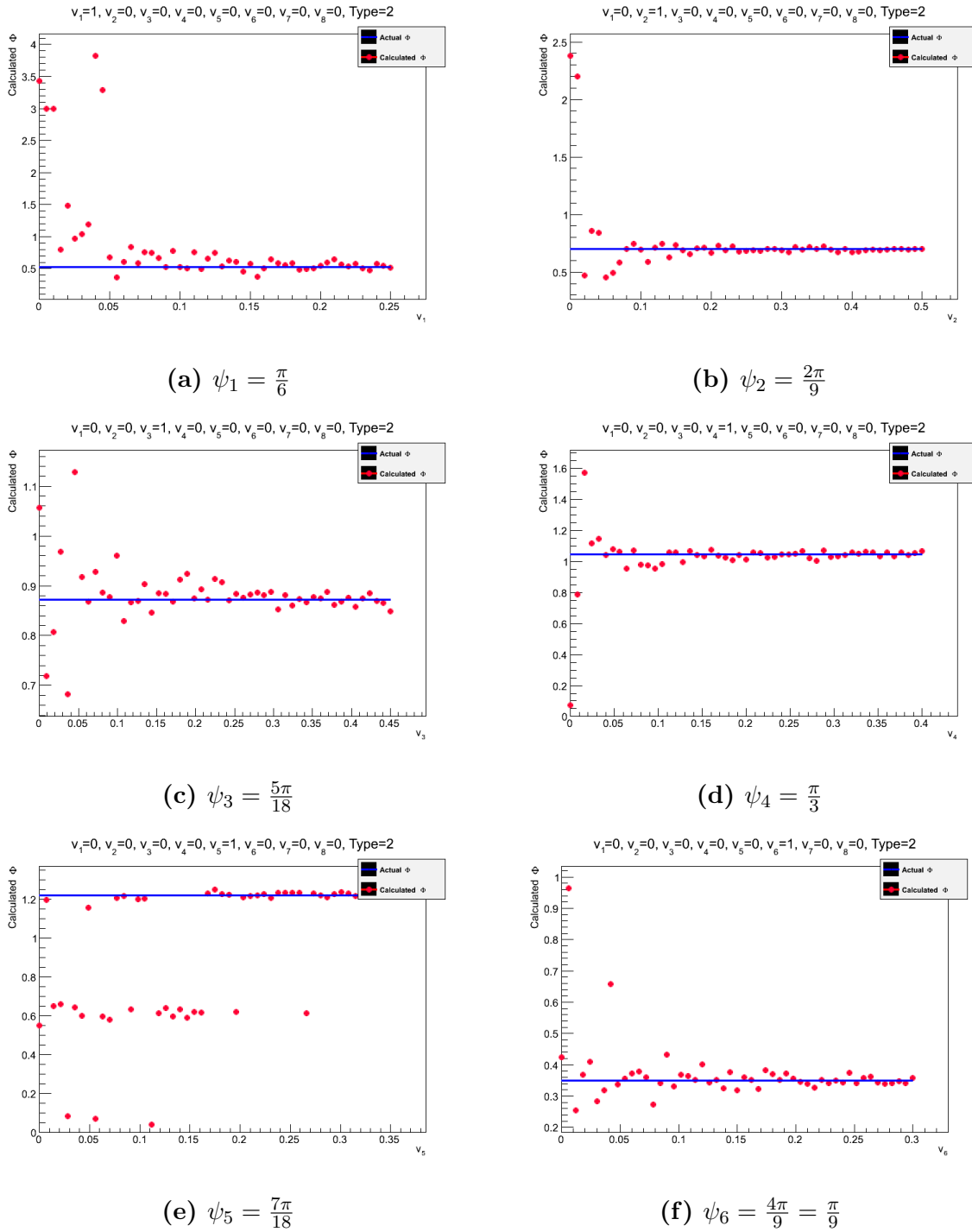


Figure 9.9: Analysis of a series of 50 events with all flow harmonics but one kept at a constant level given by $v_0 = 0.2$ in equation (9.2). Each panel represents the symmetry plane determination of the harmonic which is not kept constant and plotted against the true flow of that harmonic.

Chapter 10

Multiplicity- and mapsize dependence

In the previous chapters it was demonstrated that the flow harmonics do indeed contribute to the estimation of the values of v_n and symmetry plane and that even with a multiple of harmonics present in an event, the flow harmonics may still be estimated with a high degree of precision. However very little has been said about how the size of the map, upon which the analysis is performed, and the particle multiplicity affects the analysis. An understanding of these parameters is necessary in order to understand the analysis on real data. In chapter 11 analysis will be performed on real data from the TPC subdetector system. Since the TPC only covers the range at $\cos \theta < \pm \frac{\sqrt{2}}{2}$ and the particle multiplicities are in the order of 2-300, the interpretation of these results must obviously be seen in the light of simulated events behaviour under these conditions.

This chapter is focused on a description of the behaviour of the estimated flow when particle multiplicity is reduced and the map is narrowed in θ .

10.1 Analysis with maps narrowing in θ

The procedure in this analysis is very simple. Just as in previous analysis a series of 50 events is analysed. However in this case the analysis is performed using different mapsizes for each series of events. In order to make the simulations as realistic as possible, the analysis is performed using the method described in the previous chapter, with all but one harmonics kept at a constant level related to each other by $v_0 = 0.1$ from equation (9.2). The results are shown in figure (10.1). The figure clearly shows the same dependency on the spherical harmonics as has been demonstrated throughout the entire analysis. And in all cases (maybe with the exception of figure (10.1e)) all estimated flow values are tightly distributed around the blue line representing the best linear fit. However the slope of the curve varies, and there is no pattern, or at least not a simple one, between the variations in θ range and the slope. It might be suspected that just like in the case with full θ range, the different flow orders are in some sense comparable. However this does not seem to be the case. This is illustrated in figure (10.2). Both figure (10.2a) and (10.2b) displays a slope which do not seem to be related either to each other or to that of the elliptic flow. In the case of figure (10.2a) it furthermore appears that the uncertainty has increased when comparing it to (9.8c), since the estimated values are not as tightly packed around

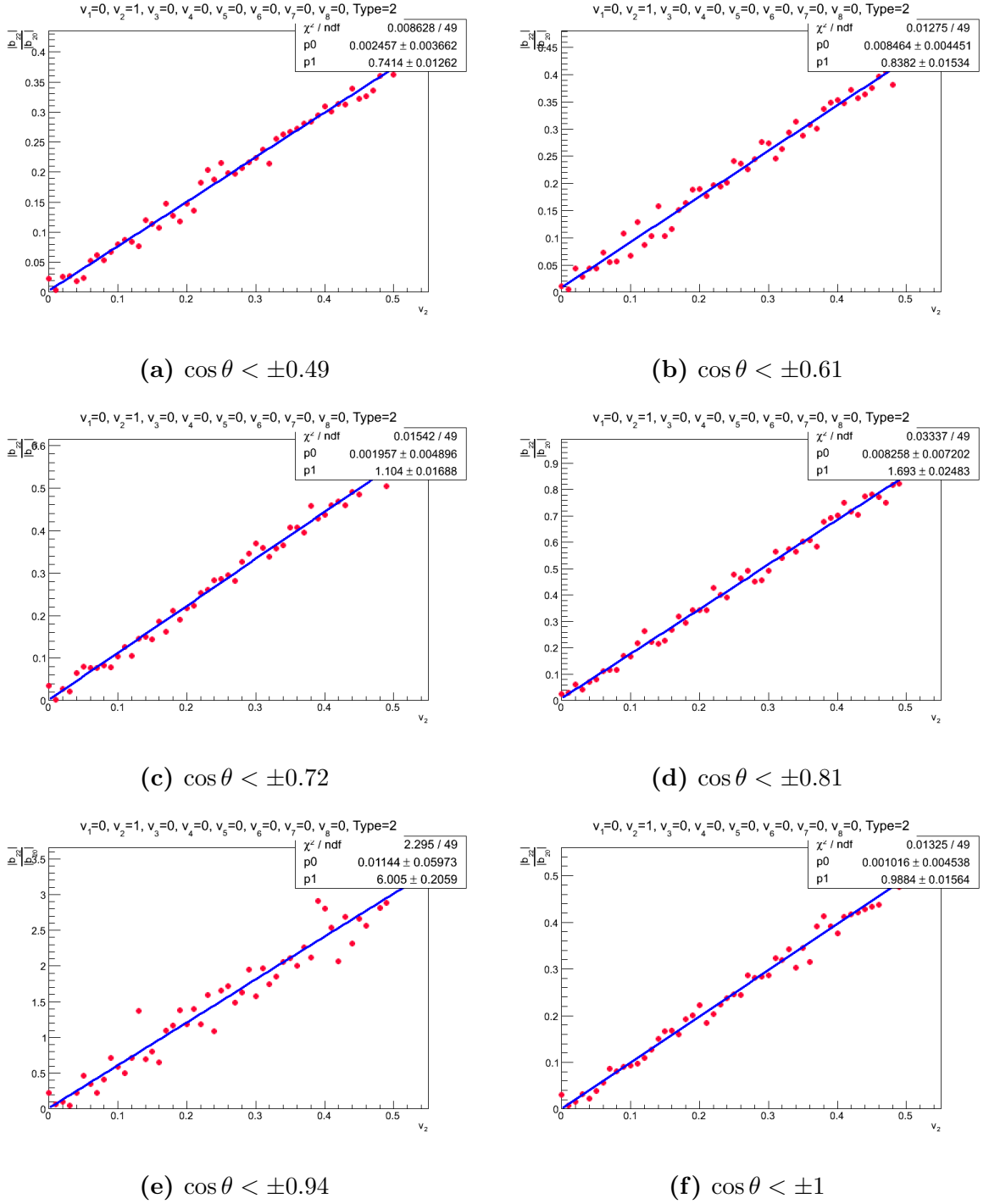


Figure 10.1: Analysis performed with varying map size. Each panel represent a series of 50 events where all harmonics but one is kept constant in all the events and related by $v_0 = 0.1$.

the linear fit in figure (10.2a) as in figure (9.8c). Table (10.1) displays the slopes for all harmonics up to eighth order when varying the range in θ . The values are both calculated with and without the $g(n)$ factor. As it appears from the table, no simple pattern can be found between the slopes and the range in θ .

The $g(n)$ factor is claimed to correct for this variation in slope with different sizes of

n	$\cos \theta$							
	± 1	± 0.94	± 0.81	± 0.72	± 0.61	$\pm .49$	± 0.36	± 0.22
1	1.361	%	1.173	0.7186	0.4516	0.2982	0.1678	0.075
	13.34	%	29.75	7.800	3.801	2.680	2.200	2.269
2	0.9884	6.005	1.693	1.104	0.8382	0.7414	0.6606	0.6025
	2.421	14.41	3.564	2.128	1.529	1.385	1.441	1.934
3	1.218	5.957	2.345	6.381	2.659	0.8128	34.78	0.1348
	6.494	31.21	12.14	41.80	38.65	37.53	5.424	3.067
4	1.276	2.598	1.590	2.902	12.65	1.704	1.001	0.7394
	10.68	21.86	13.36	20.19	59.92	5.530	2.707	2.340
5	2.217	1.422	5.587	4.332	3.529	6.517	0.6858	0.1872
	15.54	9.982	36.03	24.01	19.61	63.05	121.3	4.513
6	1.426	1.764	%	2.242	2.010	8.379	1.880	0.8737
	43.33	53.56	%	140.1	116.5	96.77	8.484	3.086
7	1.237	4.202	1.586	2.323	%	4.617	1.938	0.2861
	12.72	43.22	16.68	22.70	%	28.91	30.03	10.38
8	1.542	2.160	2.199	4.002	3.280	2.229	%	1.213
	174.9	245.0	225.6	667.4	183.4	79.65	%	5.343

Table 10.1: Table of the slopes for various ranges in θ of. The “%”, indicates that the relation with the coefficients of the spherical harmonics was not present in the given range. The table is arranged so that the slope is displayed, when evaluated with and without the $g(n)$ normalization factor, where the upper value inside a row of n is without the $g(n)$ factor and the lower value is with the $g(n)$ factor included in the calculations.

map. If that is true it requires a different pixelization than the one used in this thesis. Analysis of real events in the current pixelization will have to first calculate the slope of the curve for a given map size by the use of simulated events. When the slope is calculated, flow estimations from real events can be corrected. The symmetry plane determination is not affected by this tendency.

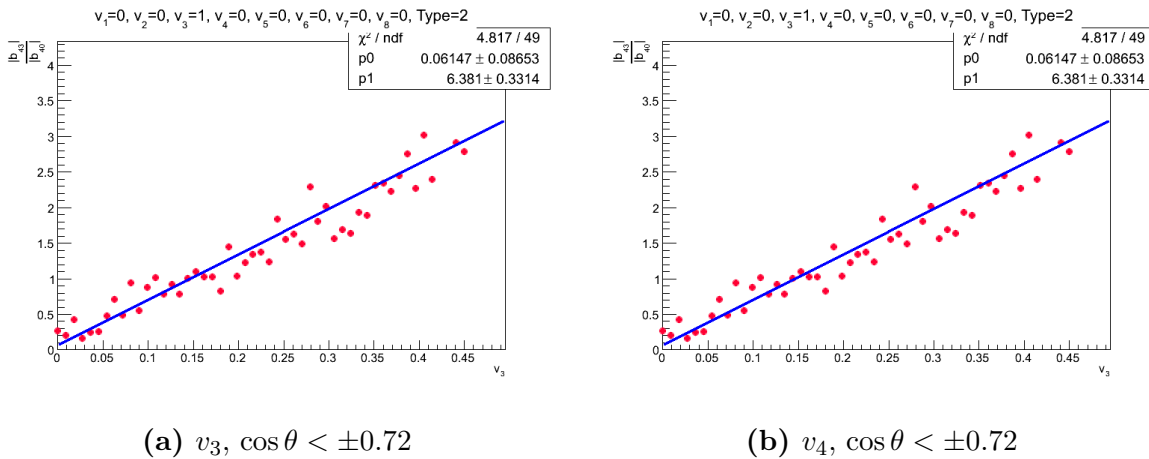


Figure 10.2: Series of 50 events with all harmonics but one are related by $v_0 = 0.1$ and kept constant. The mapsize is $\cos \theta < \pm 0.72$.

10.2 Multiplicity dependence

The second parameter to be considered is the multiplicity dependence. The analysis aims for an understanding of real data from the TPC and hence it is only performed on events with $\cos \theta < \pm 0.72$ (the reason for not choosing $\cos \theta < \pm \frac{\sqrt{2}}{2}$ is simply that with the 21×42 binning the bins at $\pm \frac{\sqrt{2}}{2}$ extends to 0.72). The analysis is performed by considering the distribution of the estimated flow from 2000 events with $v_2 = 0.1$ and $\psi_2 = \frac{\pi}{2}$ ($\frac{\pi}{2}$ is chosen so that the orientations of the symmetry planes is not split between the upper and lower limits of the range of the symmetry plane, when the standard deviation is increased as shown in figure (9.6)). The results from the analysis are shown in figure (10.3) and (10.4) for flow estimation and symmetry plane determination respectively. In the case of flow estimation the standard deviation increases with decreasing multiplicities as expected. It is not surprising that the standard deviation is increased when the map is reduced in range to $\cos \theta < \pm 0.72$ as compared to the entire range, since this is a loss of information. However it is interesting to observe that as multiplicity is decreased the mean of the estimated flow is more over-estimated with low multiplicities.

In the case of the symmetry plane determination, uncertainty is also increased with decreasing multiplicities. However the mean of the symmetry planes remains approximately at the value of the reaction plane.

The estimated values of v_1, v_3 and v_4 and ψ_1, ψ_3 and ψ_4 with multiplicity 1000 is shown in figure (10.5). It appears that when going to higher orders, the distribution of estimated flow obtain a tail. Both the tail of the third and the fourth harmonic extends outside the drawn histogram, in particular the third harmonic has a very long tail.

One last thing needs to be considered before going to the analysis of real data. That is the symmetry plane distribution for odd harmonics which can be seen in figure (10.6). The results are important because the real data has an odd behaviour in the case of odd symmetry plane determination. From figure (10.6) it is seen that in case of v_1 and $M = 1000$, the symmetry plane cannot be determined, whereas in the case of triangular flow the symmetry plane is determined with a rather high uncertainty.

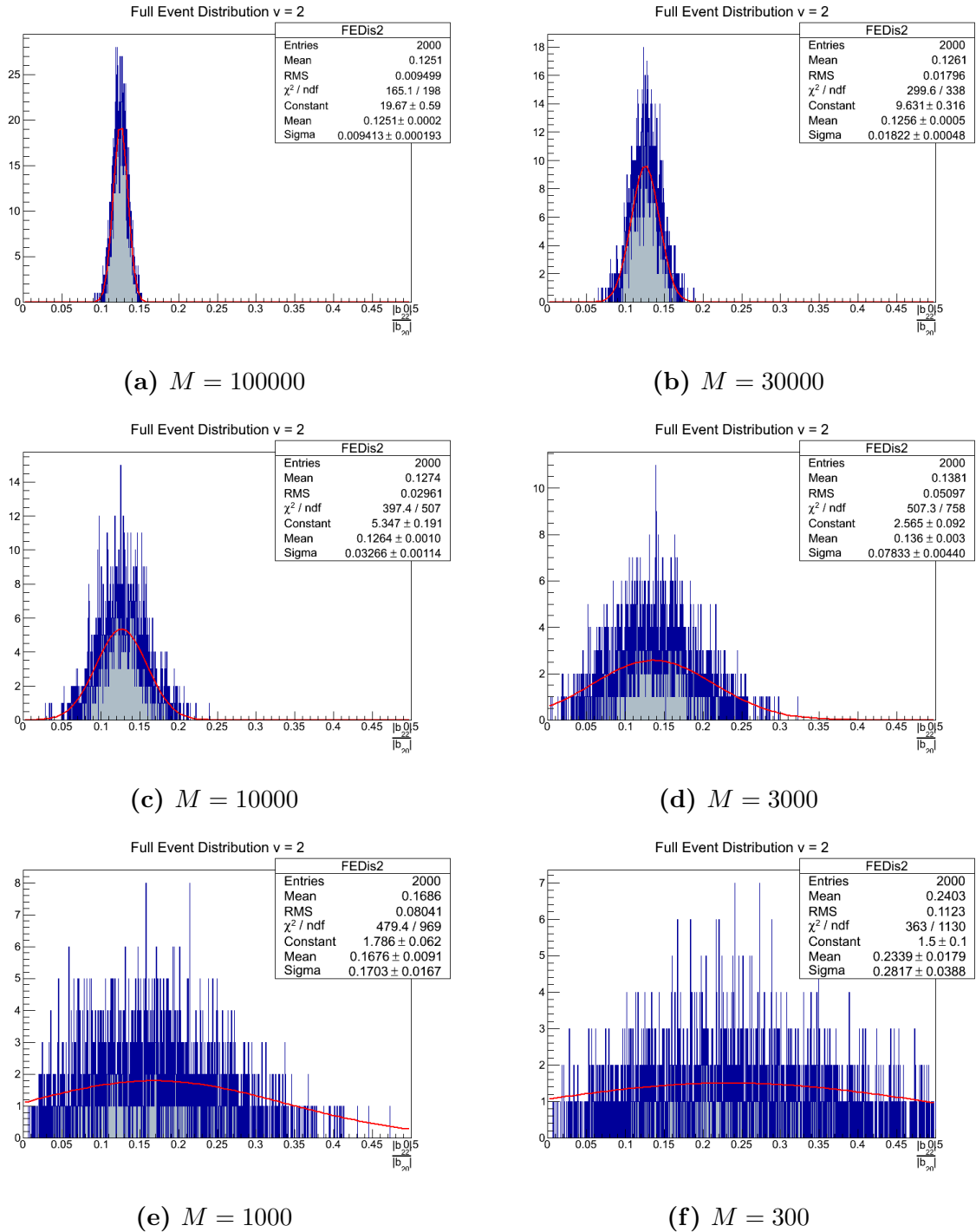


Figure 10.3: Estimated flow on 2000 events with multiplicities M ranging between 300 and 100000, $v_2 = 0.1$ and $\psi_2 = \frac{\pi}{2}$. The analysis is performed in the range between $\cos \theta < \pm 0.72$.

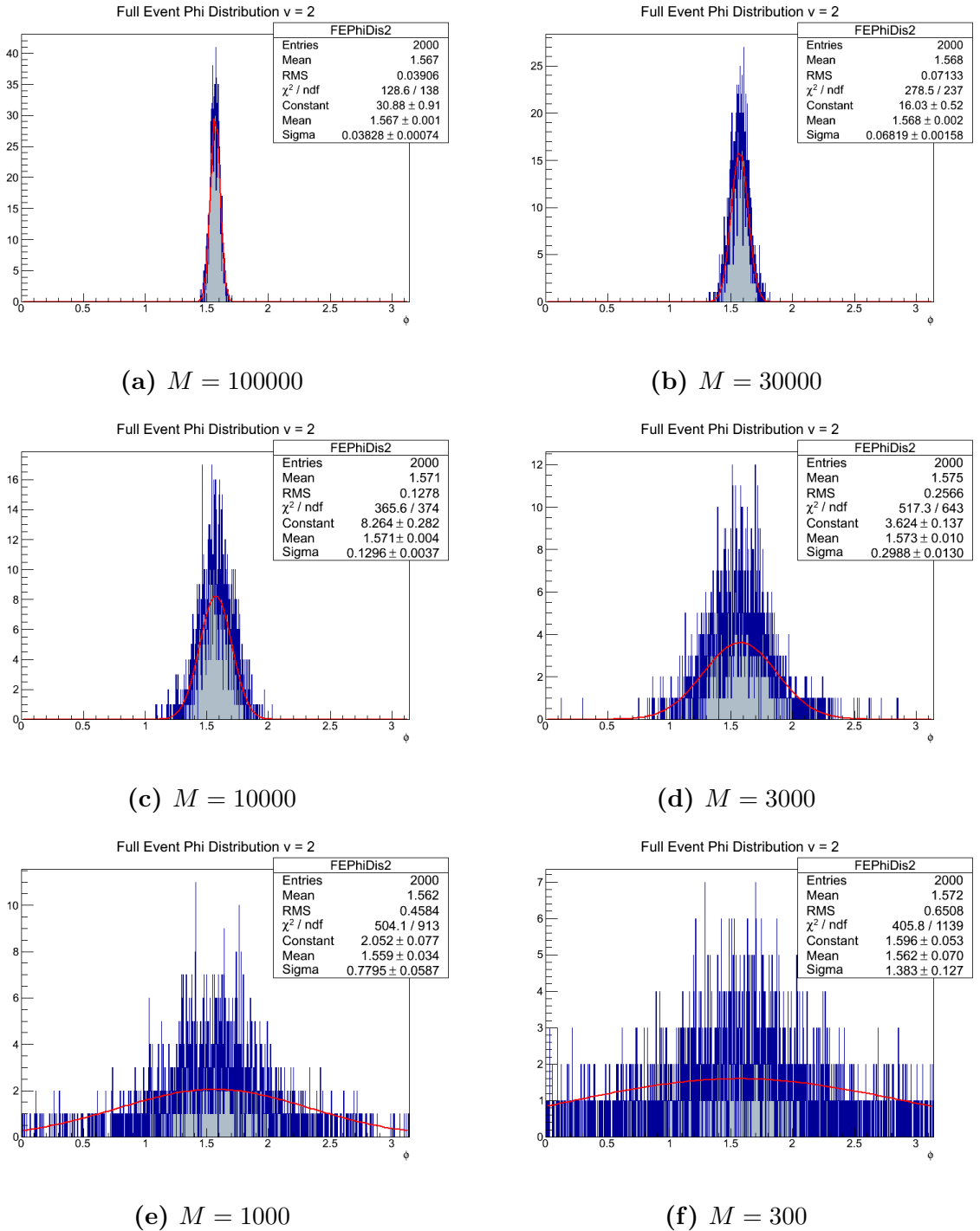


Figure 10.4: Symmetry plane determination on 2000 events with multiplicities ranging between 300 and 100000, $v_2 = 0.1$ and $\psi_2 = \frac{\pi}{2}$. The analysis is performed in the range between $\cos \theta < \pm 0.72$.

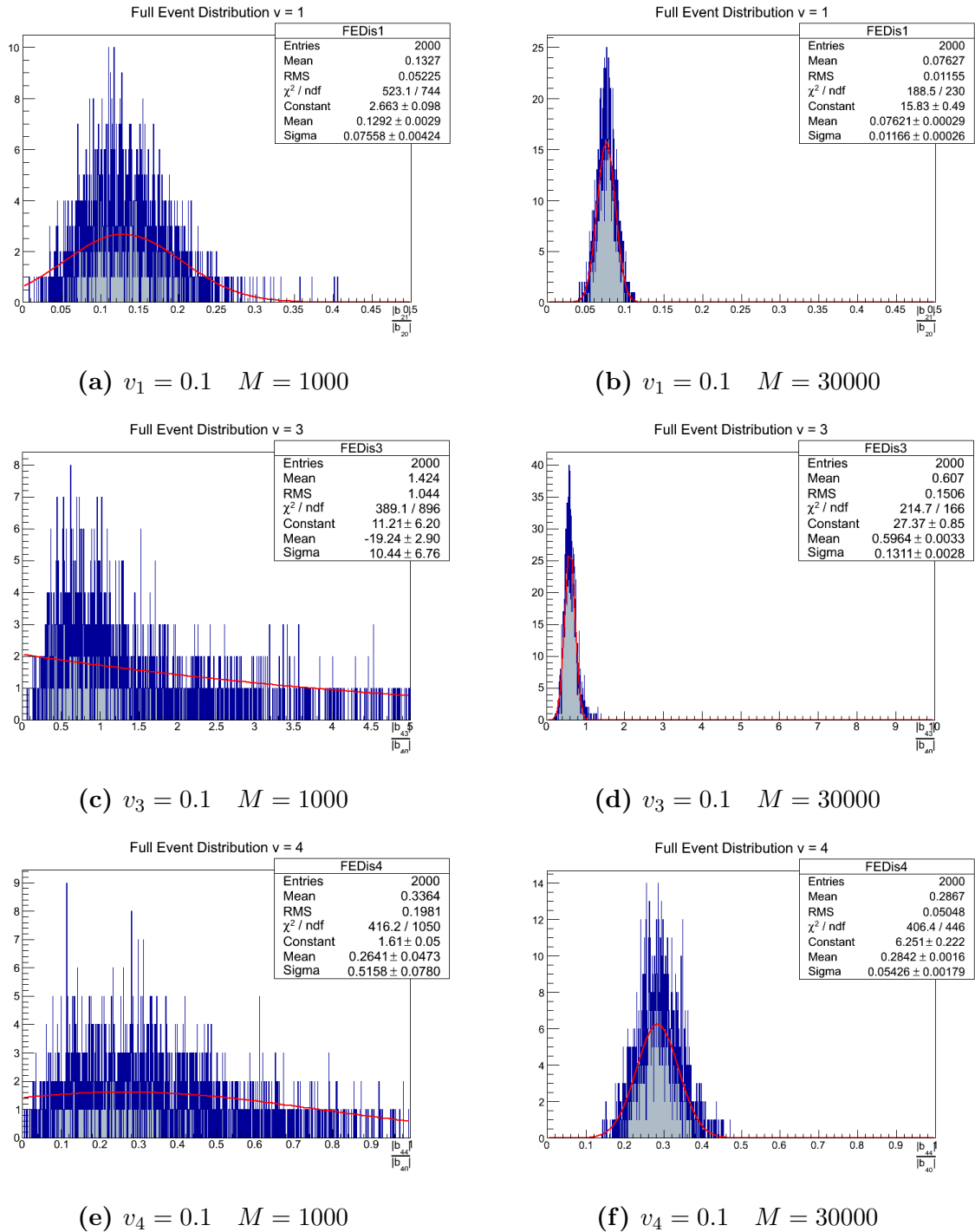


Figure 10.5: Estimated flow on 2000 events with multiplicities at 1000 and 30000, for $\nu_1 = 0.05, \nu_3 = 0.09$ and $\nu_4 = 0.08$. The analysis is performed in the range between $\cos \theta < \pm 0.72$.

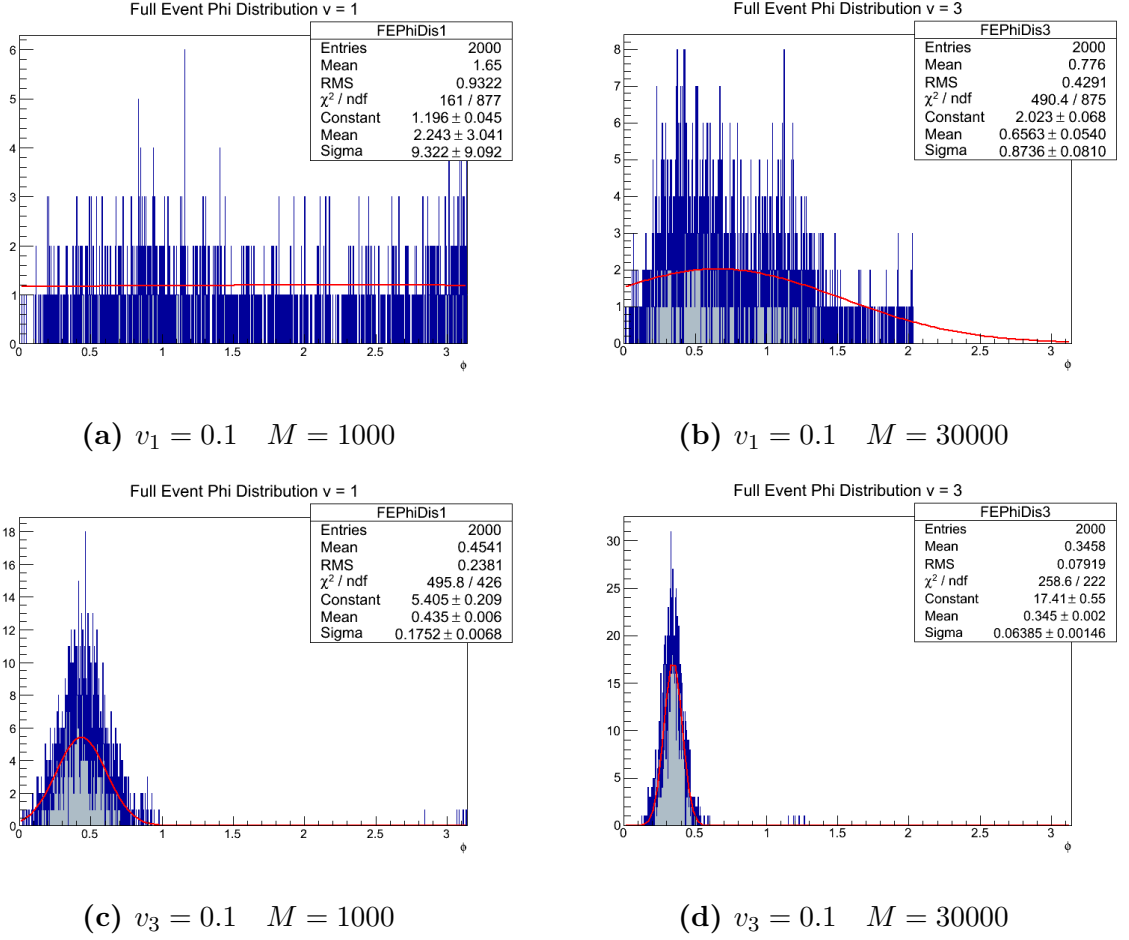


Figure 10.6: Determination of ψ_1 and ψ_3 from 2000 events in two scenarios with multiplicities $M = 1000$ and $M = 30000$, In both case $v_1 = v_3 = 0.1$ and $\psi_1 = \psi_3 = \frac{\pi}{2}$. The analysis is performed in the range between $\cos \theta < \pm 0.72$.

Chapter 11

Analysis on real events

Eventually the method can be applied to the analysis of real data. This is done by using data from the TPC subdetector system in ALICE. This is the very first approach of analysing real data and hopefully a more extensive analysis will be performed regarding this matter. Not much can be concluded from the analysis so far beyond that the method is not falsified. It appears at the moment that this is mainly due to the limitations of the TPC and in particular due to the limitations in multiplicity. Furthermore it is difficult to know how to interpret the results and which part to keep and which to discard. However the results look promising. Especially the analysis of elliptic flow appears to have prospects and indeed encourages for further analysis.

11.1 TPC analysis

The analysis is performed on data from 1992 events in the TPC subdetector system. The 1992 events are the same as those analysed in figure (4.10) with a centrality of 40 - 50%. Hence if the analysis is good the elliptic flow should be estimated somewhere in the range between $v_2 = 0.8$ and $v_2 = 1$. The multiplicity of the events is generally around $M = 2 - 300$. However the situation is more comparable to that of fig (10.3e) than to that of figure (10.3f) because the multiplicity in these figures are the multiplicity of the entire event. Whereas the multiplicity of the TPC events is only the multiplicity in the TPC range. Another thing that might cause confusion is the value of v_n because the input value of v_n in the JYG-generator is based on equation (7.1). The estimated flow in figure (4.10) is based on equation (4.4) making the estimated value of v_n in the preceding analysis only half of what is expected if equation (4.4) was used. The binning used for the analysis is the same as throughout the entire analysis 21×42 . Since the map has been reduced in θ and fewer bins are analysed, it is only possible to give an estimation of the flow up to the 4th harmonic. The results obtained in the elliptic flow estimation is seen in figure (11.1).

As it appears from the figure the estimated flow is distributed with a mean at roughly 0.2. The fact that the values of the estimated flow are distributed near around the mean, is promising, since events with same centrality are expected to have the same value of v_2 . When comparing figure (11.1) to figure (10.1c) (shown in the left corner of figure (11.1)) and remembering the factor of two, the estimated flow from TPC may be corrected by

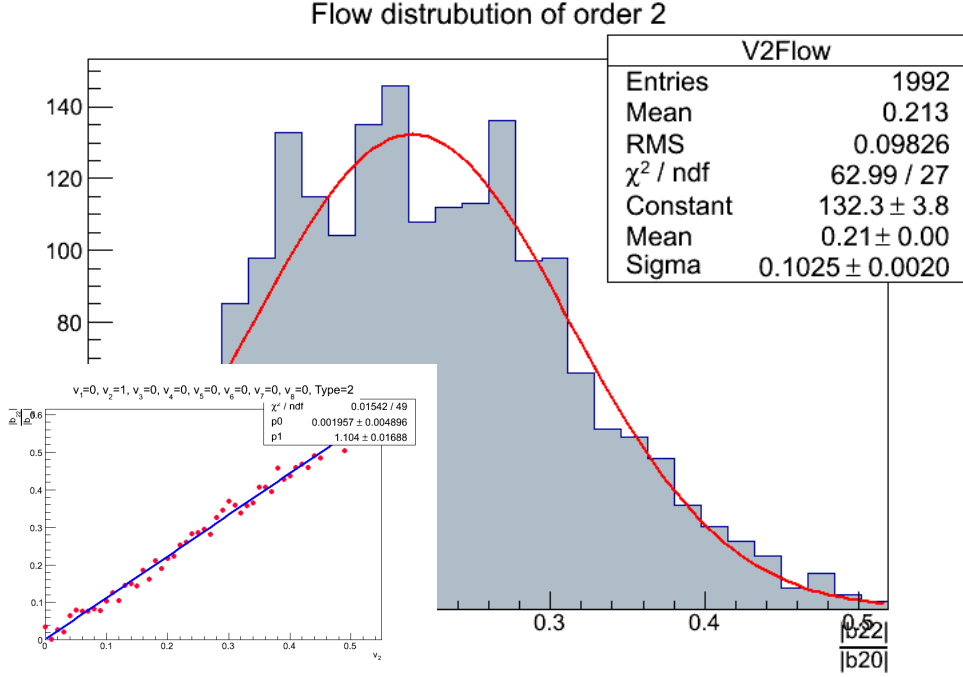


Figure 11.1: Distribution of estimated elliptic flow from 1992 events. The figure in the left corner is the estimated elliptic flow plotted against v_2 from simulated events (same as figure (10.1c)).

the use of the slope to give

$$v_2^{\text{TPC, slope correction}} = \frac{0.2088}{2 \cdot 1.099} = 0.09500 \quad (11.1)$$

This value is a little too high due to the tendency to overestimation at low multiplicities. Taking the results of figure (10.3e) into account a guess for the mean of the elliptic flow in the TPC events would be

$$v_2^{\text{TPC, multiplicity correction}} = \frac{0.09500}{\frac{0.1676}{0.1256}} = 0.07119 \quad (11.2)$$

where 0.1256 is the mean in figure (10.3b). The result is a little lower than that obtained with LYZ. However the correction is made on the basis of a 1000 multiplicity events is an approximation, and maybe it would be more suited to make the correction on the basis of 1500 multiplicity events, which would reduce the correction for overestimation.

The distribution of the symmetry planes shown in figure (11.2) is what was hoped for, namely a more or less even distribution in the entire range.

The distribution of estimated triangular flow from TPC is shown in figure (11.3). These results appears to be in agreement with what might be expected when making a comparison to figure (10.5c). The distribution exhibit the same contours with the long tail. Although it is not visible when looking at figure (10.5c), the tail is longer on the simulated events than on the TPC events.

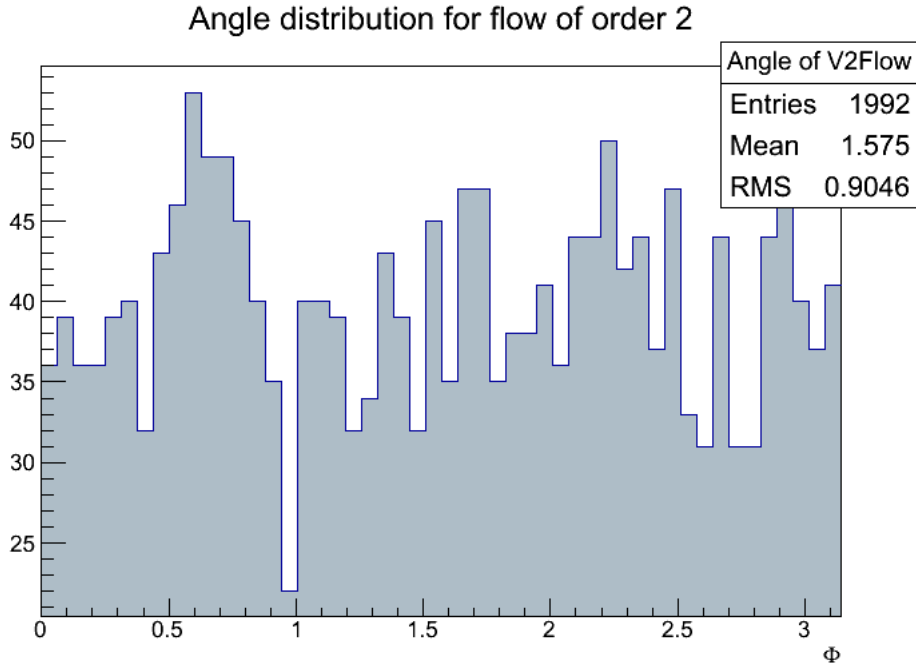


Figure 11.2: Distribution of symmetry planes from the TPC data.

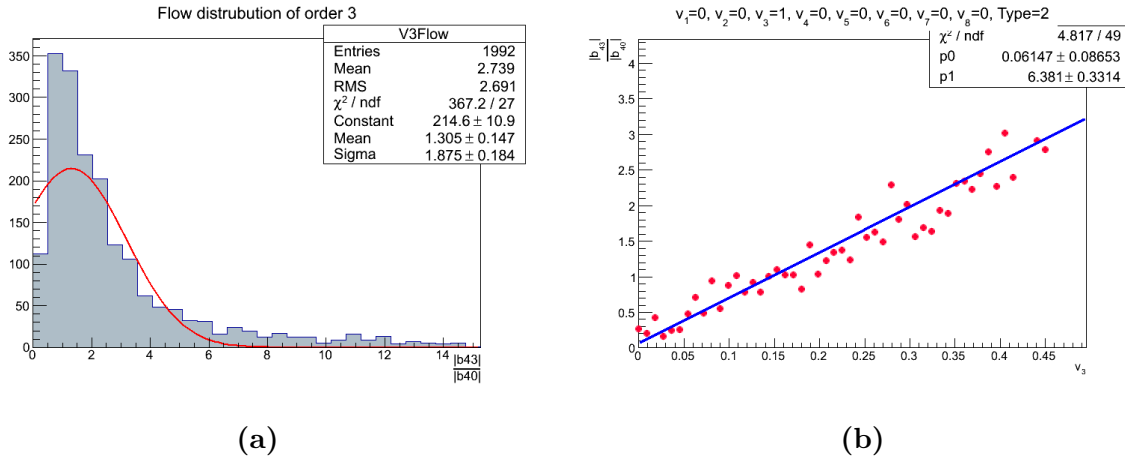


Figure 11.3: Panel 11.3a: Distribution of estimated triangular flow from 1992 events. Panel 11.3b: The estimated triangular flow plotted against v_3 from simulated events with $\cos \theta < \pm 0.72$ and $M = 30000$.

Figure (11.3b), where the estimated triangular flow of events with multiplicity $M = 30000$ and $\cos \theta < \pm 0.72$ is plotted against v_3 , can be used to make the slope correction for the estimated flow distribution in figure (11.3a). Using the slope of the fit in figure (11.3b), the mean of the estimated flow in figure (11.3a) is corrected to be

$$v_3^{\text{TPC, slope correction}} = \frac{1.305}{2 \cdot 7.055} = 0.09248 \quad (11.3)$$

Much uncertainty is connected to the correction for the overestimated value of v_3 with decreased multiplicity. Partly due to the problem mentioned about the elliptic flow, that the $M = 1000$ events may not be those which best resembles the TPC data. And partly because figure (10.5c) do not contain estimations from all events since the tale is very long. In addition figure (10.5c) is poorly approximated by the Guassian fit, and hence instead of using the Gaussian mean for the correction the assumed peak of figure (10.5c) must be used. Despite these considerable distortions a rough estimate of the Gaussian mean of the triangular flow from the 1992 TPC events is given by

$$v_3^{\text{TPC, multiplicity correction}} = \frac{0.09248}{\frac{0.07}{0.5964}} = 0.08 \quad (11.4)$$

This value can almost certainly be regarded as too high since it exceeds the value of the elliptic flow in equation (11.2).

The results for the estimated flow of v_1 and v_4 are shown in figure, after making the corrections the estimated mean of the flow is $v_1^{\text{TPC, multiplicity correction}} = 0.00418$ and $v_4^{\text{TPC, multiplicity correction}} = 0.611$.

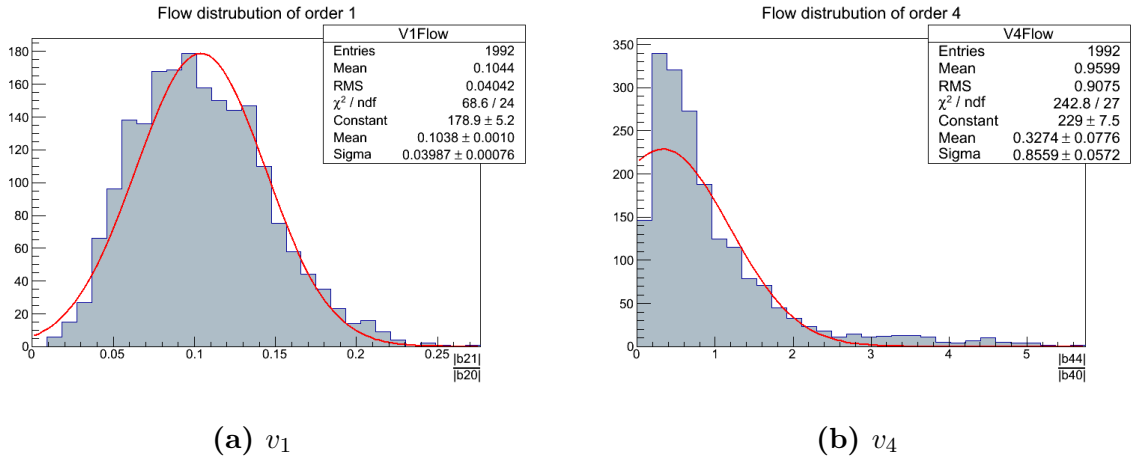


Figure 11.4: The estimated flow distribution for v_1 and v_4 . After making the corrections the estimated mean of the flow is $v_1^{\text{TPC, multiplicity correction}} = 0.00418$ and $v_4^{\text{TPC, multiplicity correction}} = 0.611$.

11.1.1 Analysis of odd ordered symmetry planes

A very interesting and unexplained part of the analysis of the symmetry planes for the odd ordered harmonics is shown in figure (11.5). It can hardly be a coincidence that the symmetry planes are symmetrically distributed around the center of range upon which they are defined. A distribution like that of figure (11.2) was more to be expected. Especially the case of ψ_1 is interesting since figure (10.6a) showed that it is not even possible to determine the symmetry plane in this case. This definitely points in the direction of an error in the calculations, but no bugs have been found so far.

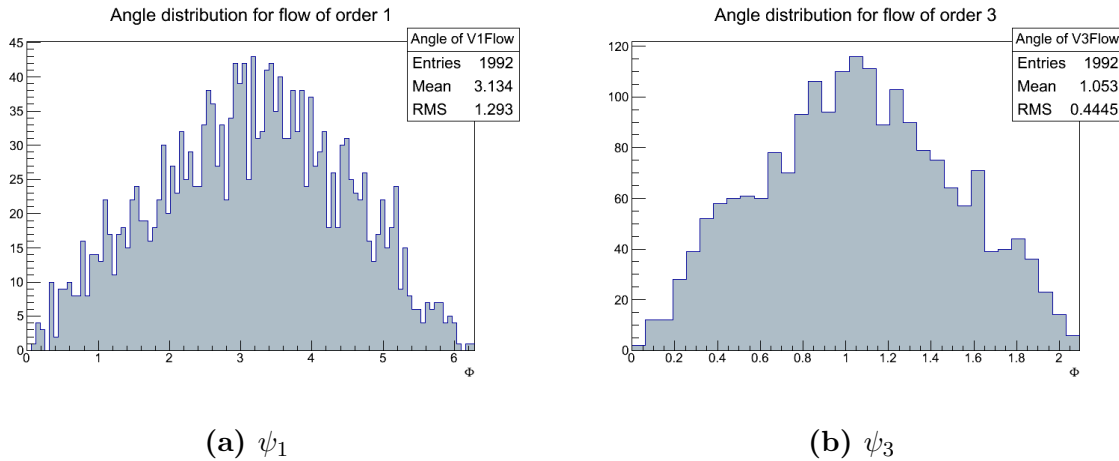


Figure 11.5: The distribution of events planes from the TPC data for ψ_1 and ψ_3 .

11.2 Accumulated TPC events

The last and a promising analysis of the TPC data is performed by adding all events with the degree of rotation of the symmetry planes for elliptic flow in common. Thus all events with $\psi_2 \in [\frac{\pi}{18}; \frac{\pi}{9}]$ are being analysed as one event and so forth for all intervals of $\frac{\pi}{18}$ in the defined range. One of the maps of the particle distribution from such added events are shown in figure (11.6). It is very interesting that the two ridges on the map, is exactly the shape expected in an event with elliptic flow. Hence it appears that the symmetry plane is properly determined. The estimated value of the elliptic flow for the map shown on the figure (11.6) is 0.1191. In this case there has been no correction made for the multiplicity, since the accumulated map contains 20246 particles.

11.3 Remarks on the TPC analysis

In the analysis of TPC data, the method described in this thesis has definitely not been falsified. However it is also hard to conclude that the method is working on the basis of the displayed results. Generally the shape of the distributions for all four flow harmonics seem to be in accordance with those of figure (10.3) and (10.5), but the estimated flow values even after the corrections are uncertain especially those of v_3 and v_4 , since the values were too high when comparing to v_2 . The estimated mean of the elliptic flow was a little lower than expected. However figure (11.6) clearly shows that the determination of the symmetry plane works well for the elliptic flow, and in this case v_2 is a little overestimated. Hence it is very likely that the error lies in the corrections, and that the method is not properly calibrated.

The symmetry plane determination of the odd harmonics gave strange results, which may be caused by an error in the calculations, since ψ_1 cannot be determined in simulated events with low multiplicity. However no bugs have been found so far and it is hard to see where it should be found since the calculations of ψ_n^{odd} utilizes the same routine as the calculations of ψ_n^{even} , and hence their might be an other yet undiscovered explanation.

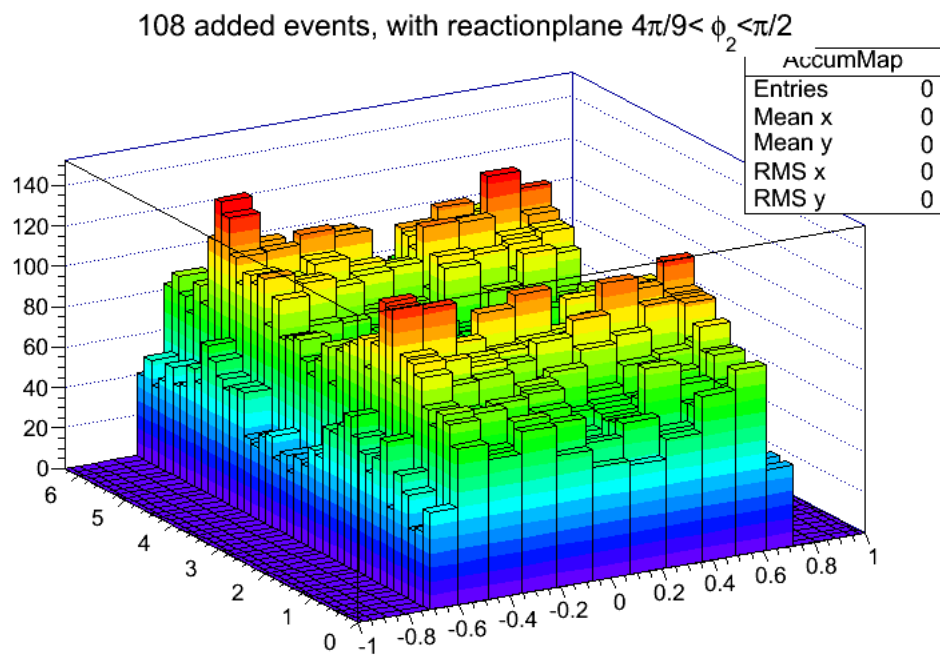


Figure 11.6: All events from TPC with $\psi_2 \in [\frac{\pi}{2}; \frac{4\pi}{9}]$ accumulated into one map.

Chapter 12

Conclusion

The focus in this thesis has been upon the investigation of a new approach to the analysis of anisotropic flow from relativistic heavy ion collisions in ALICE. By applying methods used in the study of CMB the goal has been to obtain a method that will allow for an event-by-event estimation of the flow harmonics and symmetry planes.

A general introduction to the field of relativistic heavy ion collision has been presented in this thesis, followed by a brief description of the ALICE detector, an introduction to the flow phenomenon and the conventional ways of doing flow analysis.

The approach to the new method was based on results presented in [15], where analysis with GLESP demonstrated a relation between the coefficients of spherical harmonics and the elliptic flow. The thesis has been concerned with writing a program that could do the same analysis as GLESP in ROOT, and reproduce the results presented in [15] and to extend the analysis to include higher order flow harmonics.

The ROOT version of GLESP which was designated GiRo was in some sense successfully written and it was demonstrated that $a_{l,m}$ coefficients and the powerspectrum calculated with GiRo has a relative deviation from GLESP of the order of 10^{-9} . However GiRo has two considerable flaws. Firstly the binning of the histogram produced by GiRo, although part of the GLESP package, is not the same as the pixelization used for the results presented in [15]. The consequence is that the normalization factor $g(n)$ does not yield the correct normalization. Secondly GLESP is much faster in the evaluation of the $a_{l,m}$ coefficients. Because it exploits the Gauss-Legendre quadrature in the pixelization. Although the binning in GiRo is also based on the Gauss-Legendre quadrature, it is not exploited in the evaluation of the $a_{l,m}$ coefficients.

The analysis was performed with a very simple event generator, which produced particles defined by their position in θ or η and ϕ . The distribution in η was produced with a random number generator making a Gaussian distribution in order to imitate the forward-backward symmetry in a real collision. The distribution in ϕ was likewise produced with a random number generator, but with particles evenly distributed over the entire range. For the ϕ distribution there was an option of imposing an anisotropic flow for flow harmonics up to the eighth order, where both the magnitude of v_n and the reaction plane ψ_n could be varied. The flow was imposed by omitting a factor of two from the most common way of describing flow. In this way the features of the flow were maintained, but with a different normalization. The motivation for this change was that the estimated flow in the analysis of an entire event with full range in η would not have to be normalized.

The results from [15] could not be reproduced due to the wrong pixelization which lead to a different normalization. However the same relation was found when ignoring normalization problem. The analysis was extended to include other flow harmonics. In the case of events containing only one flow harmonic, it generally appeared that the method was able to give a good estimation of all flow harmonics up to eighth order. But the uncertainty of the estimation was increased with the order of the flow harmonic.

Throughout the analysis, the elliptic flow appeared to be nearly unaffected by other flow harmonics, even when increasing all flow harmonics to large and unrealistic values, but then again the elliptic flow was always the strongest. When increasing all harmonics at the same time, higher order harmonics were severely affected. But when the magnitude of the flow harmonics was kept at a reasonable level, it was possible to give a good estimate of all harmonics.

A little less attention was devoted to the determination of the symmetry plane. But generally the analysis revealed the same features as for the flow analysis with one exception: The symmetry plane was better determined when going to higher orders of the flow harmonics.

Almost all analysis was based on events with 30000 particles distributed on a map with a 21×42 binning covering the full range in η . However the bit of analysis devoted to choice of binning, suggested that as few bins as possible gives most precise estimations. The analysis focused on the dependency on range in η revealed that the flow estimation was affected by the change in two aspects. Firstly the uncertainty on the estimations was changed, but there was no direct pattern between the η -range and the size of the uncertainty. Secondly the normalization was changed, where again no pattern was seen between the η -range and normalization factor. In the case of multiplicity dependence, the analysis revealed a strong dependency on multiplicity where generally results were impaired with decreasing multiplicity. When considering flow harmonics of order higher than two, it is questionable whether the method of analysis is useful at multiplicities lower than 1000.

In the final part of the thesis analysis of events from the TPC in ALICE were considered. The multiplicity from these events were of the order of 2-300 particles distributed in a range $|\eta| < 0.9$. There were several problems in this analysis. Firstly the low multiplicity in the events which was predicted to give results with very high uncertainty for higher order flow harmonics. Secondly the only known flow harmonic was the mean of the elliptic flow and lastly the analysis may not have been correctly calibrated against the simulated events. The results from the higher order harmonics look very suspicious when comparing with the result for the estimated elliptic flow, since the third flow harmonic was estimated a little higher than the elliptic flow and the fourth flow harmonic a little lower.

The elliptic flow of the TPC events was estimated in two ways: The first was to consider the mean of all events, and calibrate that value against simulated events, and the second was to merge all events with the same symmetry plane into one event from which the elliptic flow was estimated. The first method gave a value which was a little lower than the lowest value achieved by cumulants, and the second method gave a value which was a little higher than the highest value achieved by cumulants. However when visualizing the particle distribution from the second method, the distribution took the shape which would be expected from an event containing elliptic flow with two ridges

separated by an amount π . Thus strongly indicating that the symmetry plane is correctly determined.

In conclusion it appears from simplified simulated events that the use of spherical harmonics gives an event-by-event determination of the anisotropic flow and corresponding symmetry planes. However it would be a great advantage to have the correct normalization, which requires a different type of pixelization than the one used in this analysis. The first step has been taken into the analysis of real events, but multiplicity has been too low for the verification of the method.



Bibliography

- [1] P. Higgs, “Broken symmetries and the masses of Gauge bosons”, Physical Review Letters, Volume 13, No. 13, October 1964.
- [2] F. Englert and R. Brout, “Broken symmetries and the mass of Gauge vector bosons”, Physical Review Letters, Volume 13, No. 9, August 1964.
- [3] G. S. Guralnik et al, “Global conservation laws and massless particles”, Physical Review Letters, Volume 13, No. 20, November 1964.
- [4] C. O’Luanaigh, “<http://home.web.cern.ch/about/updates/2013/03/new-results-new-particle-higgs-boson>”, CERN homepage, March 2013.
- [5] K. Winter, “Neutrino Physics, 2nd. edition”, 2000.
- [6] F. Wilczek, “QCD Made Simple”, Physics Today pp. 22-26, August 2000.
- [7] D. Gross and F. Wilczek, “Ultraviolet Behaviour of non-abelian Gauge-theories”, Physical Review Letters, Volume 30, No. 26, June 1973.
- [8] S. Bethke, “Experimental tests of asymptotic freedom”, Max Planck institute für physik, February 2008.
- [9] L. P. Csernai, Introduction to Relativistic heavy ion collisions, November 2008.
- [10] I. Arsene et al, Quark Gluon Plasma and Color Glass Condensate at RHIC? The perspective from the BRAHMS experiment, Brookhaven National Laboratory, April 2005.
- [11] K. H. Ackermann et al, “ Elliptic flow in Au+Au collisions at $\sqrt{s_{NN}} = 130\text{GeV}$ ”, Version 20, February 2008.
- [12] J. Ollitrault, “Nucleus-nucleus collisions at RHIC: A review”, Pramana journal of physics, Vol. 67, No. 5, November 2006.
- [13] M. Atems et. al., “The chromo-Weibel instability in an expanding background”. February 2013.
- [14] B. Alver et al, “The PHOBOS Glauber Monte Carlo”, arxiv:0805.441, May 2008.
- [15] P. Nazelsky et al, “Morphology of High-Multiplicity Events in Heavy Ion Collisions”, arXiv:1204.0387v2, August 2012.

-
- [16] E. L. Wright, “Theoretical Overview of Cosmic Microwave Background Anisotropy”, arXiv:astro-ph/0305591v1, May 2009.
- [17] U. W. Heinz, “Early collective expansion: Relativistic hydrodynamics and transport properties of QCD matter”, arXiv:0901.4355v1, January 2009.
- [18] N. Herrmann et al, “Collective flow in Heavy-Ion Collisions”, Annual Review Nuclear Particle Science 1999, 1999.
- [19] P. F. Kolb et al, “Transverse flow in the quark hadron transition”, Physical Review C, Volume 62, October 2000.
- [20] R. Snellings, “Elliptic Flow: a brief review”, New Journal of Physics 13, May 2011.
- [21] E. Iancu, “QCD in heavy ion physics”, arXiv:1205.0579v1, May 2012.
- [22] S. Voloshin and Y. Zhang, “Flow study in relativistic ion collisions by Fourier expansion of azimuthal particle distributions”, Z. Phys. Vol 67. pp. 665-672, 1996.
- [23] K. Riley, M Hobson, S. Bence, “Mathematical methods for physics and engineering”, 3rd edition reprinted with corrections, Cambridge university press, 2007.
- [24] P. Duhamel, “Fast Fourier Transforms: A tutorial review and a state of the art”, October 1989.
- [25] B. Gough, “FFT Algorithms”, May 1997.
- [26] CMS Collaboration, “Missing transverse energy performance of the CMS detector”, Journal of instrumentation, June 2011.
- [27] ALICE Collaboration, “The ALICE experiment at the CERN LHC”, Institute of physics publishing and SISSA, August 2008.
- [28] R. S. Bhalerao, “Collective flow in relativistic heavy ion collisions”, Pranam journal of physics, Volume 61, Number 5, November 2003.
- [29] S. Mohapatra, “Measurement of elliptic and higher order flow harmonics in 2.76 Pb-Pb collisions with the ATLAS detector”, The 28th winter workshop on nuclear dynamics, August 2012.
- [30] A. Chaudhuri, “A short course on relativistic heavy ion collisions”, July 2012.
- [31] N. Borghini and J. Ollitrault, “Thermalization and elliptic flow at RHIC”, arXiv:0111402v1, Nov 2001.
- [32] L. Cifarelli, “The quark gluon plasma, a nearly perfect fluid”, Europhysics News, Volume 43, Number 2, 2012.
- [33] K. Aamodt et al, “Higher harmonic anisotropic flow measurements of charged particles in Pb-Pb collisions at $\sqrt{s_{NN}} = 2.76$ TeV.”, Volume 107, issue 3, July 2011.
- [34] S. Voloshin and A. Poskanzer, “The physics of the centrality dependence of elliptic flow”, Physics Letters B, Volume 474, Issue 1-2, February 2000.

BIBLIOGRAPHY

- [35] U. Heinz and R. Snellings, “Collective flow and viscosity in relativistic heavy-ion collisions”, Annual Reviews, Volume 63, 2013.
- [36] Z. Qiu and U. Heinz, “Hydrodynamic event-plane correlations in Pb+Pb collisions at $\sqrt{s} = 2.76$ A TeV”, Physics Letters B, Volume 717, Issue 1-3, October 2012.
- [37] A. Poskanzer and S. Voloshin, “Methods for analysing anisotropic flow in relativistic nuclear collisions”, Physical Review C, Volume 58, Issue 3, September 1998.
- [38] A. Bilandzic et al, “Event-plane flow analysis without non-flow effects”, Physical Review C, Volume 83, Issue 1, January 2011.
- [39] H. Masui and A. Schmah, “Event plane resolution correction for azimuthal anisotropy in wide centrality bins”, arXiv 1212.3650v1, December 2012.
- [40] A. Bilandzic et al, “Flow analysis with cumulants: direct calculations”, Physical Review C, Volume 83, Issue 4, April 2011.
- [41] N. Borghini et al, “Flow analysis from multiparticle azimuthal correlations”, Physical Review C, Volume 64, Issue 5, September 2001.
- [42] S. Adler et al, “Elliptic flow of identified hadrons in Au-Au collisions at $\sqrt{s_{NN}} = 200$ GeV” Physical Review Letters, Volume 91, Issue 18, October 2003.
- [43] T. Lee And C. Yang, “Statistical equation of state and phase transistion. II. Lattice gas and ising models” Physical Review, Volume 87, Number 3, August 1952.
- [44] R. Bhalerao et al, “Analysis of anisotropic flow with Lee-Yang zeroes” Nuclear Physics A, Volume 727, Issue 3-4, November 2003.
- [45] A. Bilandzic et al, “Event plane flow analysis without non-flow effects”, Physical Review C, Volume 83, Issue 1, January 2011.
- [46] C. L. Bennet et al, “Seven year Wilkinson microwave probe (WMAP) observations: Are there cosmic microwave background anomalies?”, The Astrophysical journal supplement series, Volume 192, Number 2, February 2011.
- [47] A. Doroshkevich et al, “Gauss-Legendre Sky Pixelization (GLESP) for CMB” International Journal of Modern Physics D, Volume 14, Issue 2, February 2005.
- [48] W. Press et al, “Numerical recipes in C”, Cambridge University Press, Second edition, 1992.
- [49] CERN press Office, “LHC physics data taking gets underway at new record collision of 8 TeV”, 05 April 2005.
- [50] A. Hansen, “Pseudorapidity dependence of elliptic flow in Pb+Pb collisions at $\sqrt{s_{NN}} = 2.76$ TeV with ALICE”, Master thesis, August 2011.
- [51] The ATLAS and CMS collaboration, “Birth of a Higgs boson”, CERN Courier, 26 April 2013.

Appendix A

Cumulants with non-uniform detector acceptance

If the detector has a non-uniform acceptance the fourth order cumulant is written as

$$\begin{aligned}
c_n\{4\} = & \langle\langle 4 \rangle\rangle - 2\langle\langle 2 \rangle\rangle^2 \\
& - 4\langle\langle \cos(n\phi_1) \rangle\rangle \langle\langle \cos[n(\phi_1 - \phi_2 - \phi_3)] \rangle\rangle \\
& + 4\langle\langle \sin(n\phi_1) \rangle\rangle \langle\langle \sin[n(\phi_1 - \phi_2 - \phi_3)] \rangle\rangle \\
& - \langle\langle \cos(n\phi_1 + \phi_2) \rangle\rangle^2 - \langle\langle \sin(n\phi_1 + \phi_2) \rangle\rangle^2 \\
& + 4\langle\langle \cos(n\phi_1 + \phi_2) \rangle\rangle (\langle\langle \cos(n\phi_1) \rangle\rangle^2 - \langle\langle \sin(n\phi_1) \rangle\rangle^2) \\
& + 8\langle\langle \sin[n(\phi_1 + \phi_2)] \rangle\rangle \langle\langle \sin(n\phi_1) \rangle\rangle \langle\langle \cos(n\phi_1) \rangle\rangle \\
& + 8\langle\langle \cos[n(\phi_1 - \phi_2)] \rangle\rangle (\langle\langle \cos(n\phi_1) \rangle\rangle^2 + \langle\langle \sin(n\phi_1) \rangle\rangle^2) \\
& - 6 (\langle\langle \cos(n\phi_1) \rangle\rangle^2 + \langle\langle \sin(n\phi_1) \rangle\rangle^2)^2
\end{aligned} \tag{A.1}$$

The Generalized fourth order differential cumulant is written as

$$\begin{aligned}
d_n\{4\} = & \langle\langle 4' \rangle\rangle - 2\langle\langle 2' \rangle\rangle \langle\langle 2 \rangle\rangle \\
& - \langle\langle \cos(n\Phi_1) \rangle\rangle \langle\langle \cos[n(\phi_1 - \phi_2 - \phi_3)] \rangle\rangle + \langle\langle \sin(n\Phi_1) \rangle\rangle \langle\langle \sin[n(\phi_1 - \phi_2 - \phi_3)] \rangle\rangle \\
& - \langle\langle \cos(n\phi_1) \rangle\rangle \langle\langle \cos[n(\Phi_1 - \phi_2 - \phi_3)] \rangle\rangle + \langle\langle \sin(n\phi_1) \rangle\rangle \langle\langle \sin[n(\Phi_1 - \phi_2 - \phi_3)] \rangle\rangle \\
& - 2\langle\langle \cos(n\phi_1) \rangle\rangle \langle\langle \cos[n(\Phi_1 + \phi_2 - \phi_3)] \rangle\rangle - 2\langle\langle \sin(n\phi_1) \rangle\rangle \langle\langle \sin[n(\Phi_1 + \phi_2 - \phi_3)] \rangle\rangle \\
& - \langle\langle \cos[n(\Phi_1 + \phi_2)] \rangle\rangle \langle\langle \cos[n(\phi_1 + \phi_2)] \rangle\rangle + \langle\langle \sin[n(\Phi_1 + \phi_2)] \rangle\rangle \langle\langle \sin[n(\phi_1 + \phi_2)] \rangle\rangle \\
& + 2\langle\langle \cos[n(\phi_1 + \phi_2)] \rangle\rangle \cdot (\langle\langle \cos(n\Phi_1) \rangle\rangle \langle\langle \cos(n\phi_1) \rangle\rangle - \langle\langle \sin(n\Phi_1) \rangle\rangle \langle\langle \sin(n\phi_1) \rangle\rangle) \\
& + 2\langle\langle \sin[n(\phi_1 + \phi_2)] \rangle\rangle \cdot (\langle\langle \cos(n\Phi_1) \rangle\rangle \langle\langle \sin(n\phi_1) \rangle\rangle + \langle\langle \cos(n\Phi_1) \rangle\rangle \langle\langle \sin(n\phi_1) \rangle\rangle) \\
& + 4\langle\langle \cos[n(\phi_1 - \phi_2)] \rangle\rangle \cdot (\langle\langle \cos(n\Phi_1) \rangle\rangle \langle\langle \cos(n\phi_1) \rangle\rangle + \langle\langle \sin(n\Phi_1) \rangle\rangle \langle\langle \sin(n\phi_1) \rangle\rangle) \\
& + 2\langle\langle \cos[n(\Phi_1 + \phi_2)] \rangle\rangle \cdot (\langle\langle \cos(n\phi_1) \rangle\rangle^2 - \langle\langle \sin(n\phi_1) \rangle\rangle^2) \\
& + 4\langle\langle \sin[n(\Phi_1 + \phi_2)] \rangle\rangle \langle\langle \cos(n\phi_1) \rangle\rangle \langle\langle \sin(n\phi_1) \rangle\rangle \\
& + 4\langle\langle \cos[n(\Phi_1 - \phi_2)] \rangle\rangle (\langle\langle \cos(n\phi_1) \rangle\rangle^2 + \langle\langle \sin(n\phi_1) \rangle\rangle^2) \\
& - 6 (\langle\langle \cos(n\phi_1) \rangle\rangle^2 - \langle\langle \sin(n\phi_1) \rangle\rangle^2) \\
& \times (\langle\langle \cos(n\Phi_1) \rangle\rangle \langle\langle \cos(n\phi_1) \rangle\rangle - \langle\langle \sin(n\Phi_1) \rangle\rangle \langle\langle \sin(n\phi_1) \rangle\rangle) \\
& - 12\langle\langle \cos(n\phi_1) \rangle\rangle \langle\langle \sin(n\phi_1) \rangle\rangle (\langle\langle \sin(n\Phi_1) \rangle\rangle \langle\langle \cos(n\phi_1) \rangle\rangle + \langle\langle \cos(n\Phi_1) \rangle\rangle \langle\langle \sin(n\phi_1) \rangle\rangle)
\end{aligned} \tag{A.2}$$

The second order cumulant from equation (4.21) in chapter 4 may be expressed by use of the Q -vector as:

$$\langle\langle \cos(n\phi_1) \rangle\rangle = \frac{\sum_{i=1}^N (\operatorname{Re}[Q_n])_i}{\sum_{i=1}^N M_i} \quad (\text{A.3})$$

$$\langle\langle \sin(n\phi_i) \rangle\rangle = \frac{\sum_{i=1}^N (\operatorname{Im}[Q_n])_i}{\sum_{i=1}^N M_i} \quad (\text{A.4})$$

The terms in equation (A.1) may as well be expressed by use of the Q -vector as:

$$\langle\langle \cos[n(\phi_1 + \phi_2)] \rangle\rangle = \frac{\sum_{i=1}^N (\operatorname{Re}[Q_n Q_n - Q_{2n}]_i)}{\sum_{i=1}^N M_i (M_i - 1)} \quad (\text{A.5})$$

$$\langle\langle \sin[n(\phi_1 + \phi_2)] \rangle\rangle = \frac{\sum_{i=1}^N (\operatorname{Im}[Q_n Q_n - Q_{2n}]_i)}{\sum_{i=1}^N M_i (M_i - 1)} \quad (\text{A.6})$$

$$\langle\langle \cos[n(\phi_1 - \phi_2 - \phi_3)] \rangle\rangle = \frac{\sum_{i=1}^N (\operatorname{Re}[Q_n Q_n^* Q_n^* - Q_n Q_{2n}^*] - 2(M-1)\operatorname{Re}[Q_n^*])_i}{\sum_{i=1}^N M_i (M_i - 1)(M_i - 2)} \quad (\text{A.7})$$

$$\langle\langle \sin[n(\phi_1 - \phi_2 - \phi_3)] \rangle\rangle = \frac{\sum_{i=1}^N (\operatorname{Im}[Q_n Q_n^* Q_n^* - Q_n Q_{2n}^*] - 2(M-1)\operatorname{Im}[Q_n^*])_i}{\sum_{i=1}^N M_i (M_i - 1)(M_i - 2)} \quad (\text{A.8})$$

The terms of the generalized second order differential cumulant in equation (4.42) which not already been expressed in terms of the Q -vector are:

$$\langle\langle \cos(n\Phi_1) \rangle\rangle = \frac{\sum_{i=1}^N (\operatorname{Re}[p_n])_i}{\sum_{i=1}^N (m_p)_i} \quad (\text{A.9})$$

$$\langle\langle \sin(n\Phi_1) \rangle\rangle = \frac{\sum_{i=1}^N (\operatorname{Im}[p_n])_i}{\sum_{i=1}^N (m_p)_i} \quad (\text{A.10})$$

The terms of equation (A.2) which remains to be expressed in terms of the Q -vector are:

$$\langle\langle \cos[n(\Phi_1 + \phi_2)] \rangle\rangle = \frac{\sum_{i=1}^N (\operatorname{Re}[p_n Q_n - q_{2n}]_i)}{\sum_{i=1}^N (m_p M - m_q)_i} \quad (\text{A.11})$$

$$\langle\langle \sin[n(\Phi_1 + \phi_2)] \rangle\rangle = \frac{\sum_{i=1}^N (\operatorname{Im}[p_n Q_n - q_{2n}]_i)}{\sum_{i=1}^N (m_p M - m_q)_i} \quad (\text{A.12})$$

$$\langle\langle \cos[n(\Phi_1 + \phi_2 - \phi_3)] \rangle\rangle = \frac{\sum_{i=1}^N (\operatorname{Re}[p_n (|Q_n|^2 - M)] - \operatorname{Re}[q_{2n} Q_n^* + m_q Q_n - 2q_n])_i}{\sum_{i=1}^N [(m_p M - 2m_q)(M - 1)]_i} \quad (\text{A.13})$$

$$\langle\langle \sin[n(\Phi_1 + \phi_2 - \phi_3)] \rangle\rangle = \frac{\sum_{i=1}^N (\operatorname{Im}[p_n (|Q_n|^2 - M)] - \operatorname{Im}[q_{2n} Q_n^* + m_q Q_n - 2q_n])_i}{\sum_{i=1}^N [(m_p M - 2m_q)(M - 1)]_i} \quad (\text{A.14})$$

$$\langle\langle \cos[n(\Phi_1 - \phi_2 - \phi_3)] \rangle\rangle = \frac{\sum_{i=1}^N (\operatorname{Re}[p_n (Q_n^* Q_n^* - p_n Q_{2n}^*)] - \operatorname{Re}[2m_q Q_n^* - 2q_n^*])_i}{\sum_{i=1}^N [(m_p M - 2m_q)(M - 1)]_i} \quad (\text{A.15})$$

$$\langle\langle \sin[n(\Phi_1 - \phi_2 - \phi_3)] \rangle\rangle = \frac{\sum_{i=1}^N (\operatorname{Im}[p_n (Q_n^* Q_n^* - p_n Q_{2n}^*)] - \operatorname{Im}[2m_q Q_n^* - 2q_n^*])_i}{\sum_{i=1}^N [(m_p M - 2m_q)(M - 1)]_i} \quad (\text{A.16})$$

Appendix B

GiRo coding

This appendix contains some of the routines implemented in GiRo

B.1 Gauss-Legendre quadrature

For the calculations of the Gauss-Legendre quadrature integral approximation, the w_i and x_i in equation (6.1) can be evaluated by following the algorithm:

```
static void GauLeg(Int_t x1,
  Int_t x2,
  UShort_t n,
  Double_t *x,
  Double_t *weights,
  Double_t eps = 1e-15)
{
  Int_t m = (n+1)/2;
  Double_t xm, x1, z, z1;
  Double_t p1, p2, p3, pp;

  xm = 0.5 * (x2 + x1);
  x1 = 0.5 * (x2 - x1);

  for (UShort_t i = 0; i < m; i++) {
    z = TMath::Cos(TMath::Pi() * ((i + 1) - .25) / (n + .5));
    do {
p1 = 1.0;
p2 = 0.0;
for(UShort_t j = 0; j < n; j++) {
  p3 = p2;
  p2 = p1;
  p1 = ((2*j+1)*z*p2-j*p3)/(j+1);
}
pp = n*(z*p1-p2)/(z*z-1.0);
z1 = z;
```

```

z = z1-p1/pp;
  } while (TMath::Abs(z-z1) > eps);
  x[i] = xm - x1 * z;
  x[n-1-i] = xm + x1 * z;
  weights[i] = 2.0*x1 / ((1. - z*z) * pp*pp);
}
}

```

where $x1$ and $x2$ are upper and lower bound of the integral, and n is the desired number of pixels.

B.2 Drawing of the histogram

The coding and drawing for a 2-d histogram with the binning presented B.1 in in the θ -direction are

```

TH2D* fMap = new TH2D("map", "#phi vs cos(#theta)",
  nbins,xbins.fArray,phiBins,0,2*TMath::Pi());
fMap->Draw("lego2");

```

where $xbins.fArray$ is the array containing each value of x_i

B.3 Evaluation of $a_{l,m}$ coefficients

The Fourier transform was performed by the routine

```

for (Int_t i = min; i < max; i++) {
  TArrayD input(np);
  //Retrieving the bincontent for each phi
  for(Int_t j = 0; j < np; j++){
input[j] = fMap->GetWeightedMap()->GetBinContent(i + 1,j + 1);
  }

  //making the FFT for the slice containg each phi of the i'th x.
  TVirtualFFT *fftwr2hc = TVirtualFFT::FFT(1 ,&np,"R2HC ES");

  fftwr2hc->SetPoints(input.fArray);
  fftwr2hc->Transform();
}

```

where np is the number of bins in ϕ and $fMap$ is the histogram from B.2. From the Fourier coefficients the $a_{l,m}$ coefficients were calculated by the routine

```

for(Int_t l = 0; l <= lmax; l++){
  for(Int_t m = 0; m <= l; m++){
//Loop to take the integral over the contents of each bin.
for(Int_t i = min; i <= max; i++){

```

```
Double_t Sph = ROOT::Math::sph_legendre(l,m,
    TMath::ACos(fMap->GetBins()->GetBinContent(i)));
}
    }
}
```

Where fRe and fIm are histograms containing the real and imaginary parts of the Fourier coefficients. min and max are the bins at the position of the lower and upper bounds of the outer integral in equation (3.14).